UNIVERSITÀ DEGLI STUDI DI MILANO

Scuola di Dottorato in Fisica, Astrofisica e Fisica Applicata

Dipartimento di Fisica

Ciclo XXIX

Spectroscopic Characterizations and DFT Simulations of Ceramic Materials: Nanostructured Zirconium Oxide and ABO_3 Perovskites

Settore Scientifico Disciplinare FIS/03

Tutore: Dott. Marco Potenza

Co-tutore: Prof. Cristina Lenardi

Correlatore: Dott. Alberto Debernardi

Coordinatore: Prof. Francesco RAGUSA

Tesi di Dottorato di:

Patrizia Rosa

Anno Accademico 2015-2016

Commission of the final examination:

External Referee:
Michele Perego, CNR, IMM Institute for Microelectronics and Microsystems, Italy

External Referee:
Guido Roma, Atomic Energy Commission (CEA), France

External Member:
Maddalena Collini, Dipartimento di Fisica; Università degli studi di Milano Bicocca, Italy

External Member:
Luca Nobili, Dipartimento di Chimica, Materiali ed Ingegneria Chimica "G. Natta". Politecnico di Milano, Italy

Internal Member:
Giovanni Onida, Dipartimento di Fisica, Università degli Studi di Milano, Italy

Final examination:

Date 30th June 2017

Università degli Studi di Milano, Dipartimento di Fisica, Milano, Italy

To my Parents

MIUR subjects:

FIS/03 -

PACS:

61.05.cp
61.46.Hk
61.50.Ah
61.50.Nw
61.72jd

Contents

Chapter 1

Introduction

This fellowship was supplied by Ministero dell'Istruzione, dell'Università e della Ricerca (MIUR) in the area of interest of advanced material for structural applications. Specifically, the structural applications are considered regarding the topic of pollution reduction.
The pollution due to the human activities and the consequences on global climate change has been emphasized by so many scientific studies that, in 1997, some nations decided to make a treaty to face this problem. This international treaty is known as the Kyoto protocol that is committed to the reduction of greenhouse gas emissions. Moreover, in the last two decades, we have been witnessing an increase in the public awareness on the consequences of pollution not only on climate change but also on human health, promoting lifestyles with a lower pollution impact, but we are far away from solving the problem.
The main method emerging over these years for pollution reduction is to convert the greenhouse gas into other harmless chemical substances with a conversion rate adequate to the rate of greenhouse production. For example, the catalytic converters combine oxygen with carbon monoxide (CO), unburned hydrocarbons (HC) and nitrogen oxides (NO_x) to produce carbon dioxide (CO_2), water (H_2O) and nitrogen (N_2).Moreover, the catalytic devices usually work at a high temperature. For example, a catalytic converter works between 180 °C and 380 °C.This implies that the material must be stable in this temperature range. The catalysis can also be used also in industrial facilities both for the production of specific chemicals or pollutant reduction. In catalysis, the surface of the material is the active part that enables the catalytic processes. Nanomaterials have a higher surface area than bulk material so that there is increased catalytic

activity because more catalytic reactions can occur at the same time [1]. In particular in recent years nanostructured Pt, Pd, Au and Fe and metal oxide thin films such as CeO_2, TiO_2, ZnO and ZrO_2 were the more studied materials for catalysis [2, 3]. In particular for zirconia, the catalyst activity is the maximum when the material has a tetragonal or cubic crystal phase; while, in the monoclinic phase, the activity is lower [3].
Another application of zirconia is as support for catalysis. With a view to reducing pollution, Drying (CO_2) Reforming of Methane (DRM) has attracted extensive attention because this process simultaneously consumes two greenhouse gases (CH4 and CO2) and converts them into synthesis gas (H_2 and CO), which can be further transformed into various chemicals and fuels [4]. The use of nickel (Ni) as a catalyst seems to be a good alternative to the noble metal that, with their high cost and limited availability, restricts its extensive use in industrial applications. However, Ni is sensitive to deactivation due to carbon deposition after long-term catalytic processes. Therefore, for a good supported Ni catalyst, a bifunctional mechanism is required: CH_4 is activated on the Ni particles, while CO_2 dissociates on the support. Tetragonal and cubic zirconia appear to be a very good candidate to have these behaviors. Moreover, the nanostructure, morphology, and oxygen vacancies can also contribute to the high performance of zirconia [5–7].

Zirconia can also be used as electrolyte in a Solid Oxide Fuel Cell (SOFC)[8, 9]that is an electrochemical conversion device that produces electricity directly from oxidizing a fuel. The advantages of this class of fuel cells include high efficiency, long-term stability, fuel flexibility, low emissions, and relatively low cost. The largest disadvantage is the high operating temperature (greater than 700 °C) that results in longer start-up times and mechanical and chemical compatibility issues [10]. Using as electrolyte, the working temperature can be reduced to 400 °C for a thin film of zirconia [11]. Also in this application, the crystal phase stability of cubic or tetragonal zirconia at a temperature higher than room temperature is important for the performance of the final device. Both catalytic activity and electrolyte propriety seem to also depend on the oxygen vacancies [12, 13]. These three examples of the use of zirconia have the following in common: best performance in using nanostructured thin film in a cubic and tetragonal crystal phase and a working temperature higher than room temperature so it is necessary that there is stability of the material at working temperatures. In particular as support for DRM, the morphology also influences the nanostructured zirconia performance [6]. At Molecular Beam Laboratory of the Università degli Studi di Milano by Supersonic Cluster Beam Deposition

(SCBD), we can make nanostructured thin film of zirconia with a controlled morphology as described in Chapter 2 . Chapter 3 is dedicated to a brief general overview of zirconia, both in bulk and nanostructured form with particular interest in the crystal phase and in the role of oxygen vacancies in phase stability. In the characterization, a possible catalytic application is focused on. I studied the stoichiometry and chemical surface stability after thermal treatments of this material by X-ray Photoelectron Spectroscopy (XPS) along with the crystal phase and nanocrystal size by X-ray Powder Diffraction (XRPD). The physical phenomena and apparatus of these two techniques are described in Chapter 4. The experimental results are exposed in Chapter 7, Chapter 8 for XPS and XRPD respectively, after the description of thermal treatment made in Chapter 6. In the experimental part, the presence of oxygen vacancies has been found and in order to understand the role of these vacancies I performed some simulations on bulk zirconia with oxygen vacancies using the Density Functional Theory (DFT) as covered in the last section of Chapter 4. In Chapter 9, the results of these simulations for bulk are described. Moreover, a simple confinement model has been applied in order to see the differences between bulk and nanocrystal zirconia. This is also a preliminary study before a possible further development in which the confinement effect with a more refined model and surface interaction can be introduced. In Chapter 12, there is an overview of the results about nanostructured zirconia underlining the differences and similitude of the different techniques, with an outlook on the further development.

On the topic of air pollution, Kyoto protocol also commits to the reduction of CO2 emissions in the atmosphere. In this case, another two ceramic materials, belonging to perovskite, $La_{0.6}$,$Sr_{0.4}Co_{0.2}Fe_{0.8}O_{3-\delta}$ and $Ba_{0.5}$,$Sr_{0.5}Co_{0.8}Fe_{0.2}O_{3-\delta}$, can be used. In this case the approach is not to transform the CO_2 in other chemical substances, but rather the CO_2 carbon capture and storage (CCS) to relieve global warming by capturing CO_2 and storing it instead of releasing it into the atmosphere [14–17]. Different fossil fuel power plant concepts for CCS are currently being developed, such as oxy-fuel power plants. In this process, the fossil fuel is combusted using pure oxygen and the result is a gas stream with almost pure CO_2 (90-95%) in the dried flue gas. The CO_2 can then be captured more easily than when air is used in the combustion process and stored in a safe geological site [18]. Actually the two fundamental approaches to air separation are the cryogenic and non-cryogenic distillation. The first one works at ultra-low temperature, while the latter one at ambient temperature using pressure swing adsorption (PSA). Recently, a third category of air separation has emerged, which is based on a specialized ceramic membrane that carries out the

separation of oxygen from air at elevated temperatures, typically 800 °C to 900 °C, in order to activate the oxygen diffusion process through the membrane [19]. Moreover, this dense ceramic membrane can be integrated in catalytic membrane reactors for carrying out different petrochemistry processes. In this field, some kinds of perovskitic membranes can be used for the pure oxygen production. In particular, $La_{0.6}$,$Sr_{0.4}Co_{0.2}Fe_{0.8}O_{3-\delta}$ and $Ba_{0.5}$,$Sr_{0.5}Co_{0.8}Fe_{0.2}O_{3-\delta}$ seem to be more promising[20–29]. Chapter 11 is devoted to the study of two kinds of perovskite. In collaboration with RSE SpA - Ricerca sul Sistema Energetico, these two materials were characterized using different techniques before and after work conditions. In Chapter 12, there is a global conclusion of this work.

Part I
Background

Chapter 2

Cluster Assembled Materials

I am interested in the future application of a thin film of nanostructured zirconia as catalytic support for the drying reforming of methane (DRM) and as an electrolyte in a Solid Oxide Fuel Cell (SOFC). In the first application, the zirconia support allows for the use of nickel (Ni) as a catalyst for DRM instead of the noble metal overcoming the problem of the cost and of the availability of noble metal making this technology suitable for industrial application. The importance of the support in the use of Ni as a catalyst is to prevent the carbon deposition on the Ni and consequence deactivation of the catalyst. Moreover, the morphology of the support influences the DRM as demonstrated in [6]. In particular, the roughness of the support determines the number of sites available for CO2 dissociation. With Super-sonic Cluster Beam Deposition (SCBD), we can make a thin film of nanostructured zirconia with controlled roughness [30].

In the latter application, the use of a thin film of nanostructured yttra-stabilized zirconia can reduce the working temperature from 800 °C to 400 °C [11]. The role of yttria is to stabilize the cubic and tetragonal phase at the working temperature. With Super-sonic Cluster Beam Deposition (SCBD) we can make thin films of nanostructured zirconia in a cubic crystal phase stable at room temperature without adding yttria.

2.1 Supersonic Cluster Beam Deposition

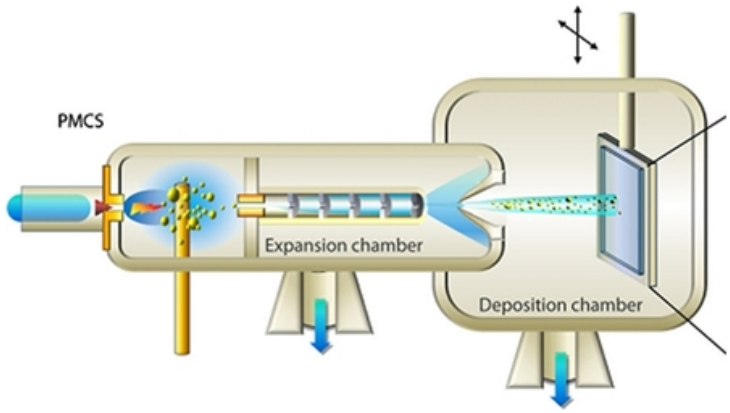

Figure 2.1: SCBD apparatus at LGM: schematic view [31]

During the last three decades, the Molecular Beam Laboratory of the Università degli Studi di Milano has developed the Pulsed Microplasma Cluster Source (PMCS) for Super-sonic Cluster Beam Deposition (SCBD). It combines the advantages of the gas-phase synthesis of nanoparticles with the benefits arising from supersonic molecular beams and aerodynamic focusing method that are crucial for the control of the particle beam shape and velocity. The applications of this technique for obtaining nanostructured materials are described in detail in several papers, see Ref. [32–38]. Therefore, in this section, the basic operating principles of the cluster source, PMCS, and the deposition method, SCBD, are reported.

The SCBD apparatus, shown in Fig. 2.1, is composed of a PMCS source, an expansion chamber, and a deposition chamber. The PMCS (Fig. 2.2) is a pulsed vaporization source with a typical repetition frequency of 1-10 Hz based on the ablation of a target by a pulsed confined plasma ignited by an electrical discharge. An inert gas (e.g. argon or helium) at high pressure (30-50 bar) is injected into the source cavity by a pulsed solenoid valve (valve opening time

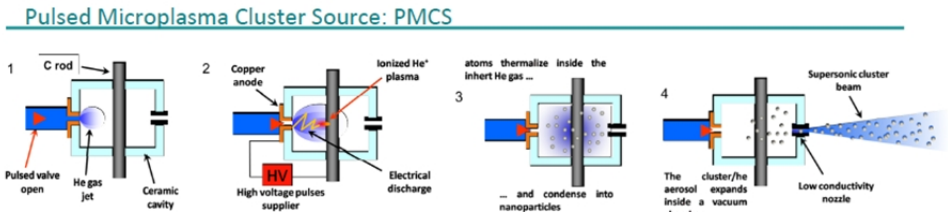

Figure 2.2: PMCS: schematic view [32]

is 150-250 μs). The strong density gradient, generated by the gas jet which impacts on the side of the cathode rod, together with a high potential difference (500-1,000 V), applied after the valve closed (delay time ca. 600 μs) between the cathode and anode, causes the firing of the discharge (duration ca. 80 μs) and the formation of a strong-localized plasma (micro-plasma). The rod, which can be of any conductive solid material, is thus locally vaporized by the plasma, and the vapor is quenched by inert gas forming small aggregates. In the cavity there are cluster-cluster interactions, aggregations, and rearrangements leading to a cluster size and structure which evolve with increasing residence time in the source [31].In the PMCS source, there is the formation of gas-clusters mixture that goes into a vacuum chamber, i.e. expansion chamber, passing through a focusing system, see Fig.2.3, and producing a collimated supersonic cluster beam.

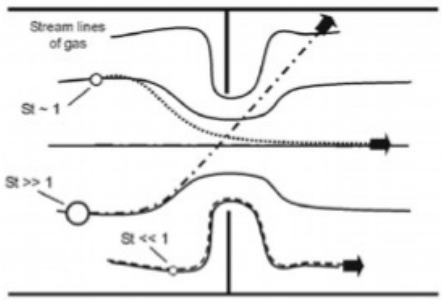

Figure 2.3: Schematic illustration of the basic principles of an inertial focusing lens [32]

Supersonic expansion produces a high outward radial velocity that varies with the radial position in the jet dragging the nanoparticles. The cluster response to this radial drag is the function of their position in the beam and of their size. As shown in Fig. 2.3, after passing an aerodynamic lens, only particles with a critical size (Stokes number, St $\approx$ 1) move closer to the centerline, while bigger clusters (St$\gg$1) and smaller clusters (St$\ll$1) do not merge the lens axis. This effect gives a selection of size and reduces the angular distribution of the clusters produced by the PMCS [32, 38].Nanoparticles with kinetic energy lower than 0.5 eV/atom, which is well below the cluster binding energy, reach the substrate in the deposition chamber. Due to the low kinetic energy the cluster lands on the substrate without fragmentation as schematically reported in Fig 2.4. By depositing preformed clusters on a substrate, one can build cluster assembled materials in which cluster physico-chemical properties, as long as inter-clusters aggregation is suppressed, are preserved. In this way, the size dependent characteristics as well as the large surface to volume ratio of the preformed clusters are in principle transferred to the thin film and it is possible to obtain a memory effect [30].

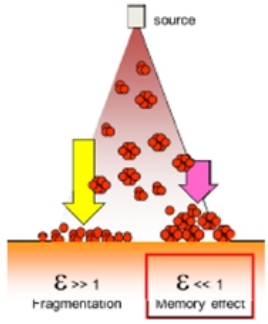

Figure 2.4: Schematic illustration of high kinetic regime, $\epsilon >> 1$, with clusters fragmentation, and low kinetic regime, $\epsilon << 1$, with memory effect.

Chapter 3

Zirconia

Zirconia, or zirconium dioxide ZrO_2, is a widely studied material for its strength and fracture toughness [39], low thermal conductivity, ionic conductivity [40], chemical resistance, and biocompatibility [41]. From these characteristics, a broad range of applications derive thermal-barrier coatings [42], wear resistance coatings[43], protective coatings for optical mirrors and filters [44], high temperature fuel cells [45], oxygen detectors to catalyst supports [45, 46], biomedical and tissue engineering applications [47–49].
This work is dedicated to the characterization of nanostructured zirconia thin film in view of two fundamental applications: as catalytic support for DRM and as an electrolyte Solid Oxide Fuel Cell (SOFC) as discussed in the Chapter [1] and in the first part of Chapter 1 and in the first part of Chapter 2. In this application, the tetragonal and cubic phase gives the best performance results. However, in the range of the working temperature for these two applications, 400 °C and 800 °C, the stable crystal phase is the monoclinic one.

In fact at normal atmospheric pressure, zirconia shows three different crystal phases: monoclinic phase, which is stable from room temperature to 1175 °C, as shown in Fig. 3.1a, tetragonal phase in Fig. 3.1b stable from 1175 °C to 2370 °C and the cubic phase, stable from 2370 °C to 2750 °C [50, 51] whose structure is similar to the tetragonal one. The previews properties of zirconia are typically of the cubic and tetragonal phase that are stable at high temperature. However, for technological applications, and not only in DMR end SOFC, tetragonal and cubic phases present better properties (hardness, high-dielectric constant, etc.) than the monoclinic one. As mentioned in Chapter 2 it is possible to stabilize the tetragonal/cubic phase at room temperature partially substituting

some zirconium atom with yttrium. This substitution induces oxygen vacancies to maintain charge neutrality. From Ref. [52] seems that for an yttrium density below a critical concentration the oxygen vacancies are located near the zirconium atom. For higher concentration the vacancies start to be located near the yttrium atom and this degrades permeation performance. This means that the permeation performance is due to oxygen vacancies rather than to the yttrium presence. From this result, it seems that vacancies bound to yttrium are less mobile and not available for oxygen transport.
The main role of oxygen vacancies to stabilize the cubic or tetragonal phase at room temperature is also confirmed by simulation data [53, 54]. Another way to have the cubic or tetragonal phase of zirconia at room temperature is the use of nanostructured zirconia [55]. It is not yet completely clear what the mechanism of stabilization is in the nanostructure, and different explanations are proposed [56]. However, what emerges for experimental data is that there is a nanocrystal critical size and for values below this critical size, the stable phase at room temperature is the cubic/tetragonal phase.

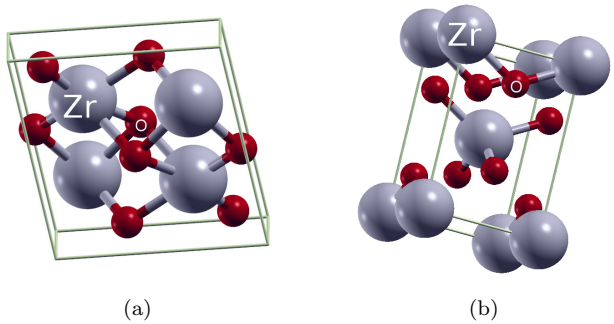

(a) (b)

Figure 3.1: (a) monoclinic and (b) tetragonal zirconia.

3.1 Nanostructured ZrO_2

Nanostructured material has a bigger surface-area volume ratio than the bulk material and this can be an advantage, for example in catalytic application, in biosensing [57–59], and cell culturing [48] or for proteins and enzyme adsorption [60], in which parameters such as the active surface area, surface roughness, and substrate topography are also critical.

The nanostuctured zirconia (ns-ZrO_2) is a good candidate for such applications [30]. It has a different phase stability with respect to the bulk. In particular, the cubic and tetragonal phase in ns-ZrO_2 can be stable at room temperature [61, 62]. Different methods have been reported for the synthesis of ns-ZrO_2 films: sol-gel, spray pyrolysis, micro-wave plasma processes, sputtering, non hydrolytic thermal decomposition, and ion beam assisted deposition technique (IBAD)[47, 63–65]. The characteristics, as a behavior on thermal treatment, are not uniquely determined by the nanostructure, but rather depend on the production condition. For example, in Djurado et al. [65], the authors report a different crystallite size for different spray-pyrolysis conditions in the ns-ZrO_2 preparation. The stabilization mechanism at room temperature depends on the nanocrystalline critical size. In the literature for ns-ZrO_2 we find different values for this critical size, r_c as reported in Table 3.1 where the experimental and theoretical values are indicated.

r_c (nm)	kind.	Ref.
6	Theor.	[66]
6	Theor.	[67]
6.9	Exp.	[65]
10	Exp.	[66]
13.2	Exp.	[65]
25	Theor.	[56]
30	Exp.	[68]
33	Theor	[56]
33	Exp.	[69]

Table 3.1: some critical sizes for ZrO_2 from different works

These different values depend on different factors that can influence the surface energy: aggregation of nanocrystals, change in surrounding atmosphere, hydrostatic pressure, internal hydrostatic pressure, presence of anions, oxygen vacancies[56].
Some of the cited applications involve higher temperature than the room temperature, i.e. catalytic process and high temperature fuel cells, so it is important to study the evolution of these materials under thermal treatment. The two main effects of temperature are the oxidation and the growing of nanocrystals. According to these two effects and to the critical size of the nanostructure we can have a phase change [30, 65] that can affect the performance of the material in the application.

3.1.0.1 Oxygen vacancies

In some of these applications, for example in high temperature fuel cells and catalysis, the performance of the material depends not only on the surface or the different phase but also on oxygen vacancies [3]. In a very recent work of Borghi et al. [30] the role of the presence of an oxidative environment on the nanocrystal growth and on the crystal phase transition as reported in Fig. 3.2 and 3.3 was emphasized..

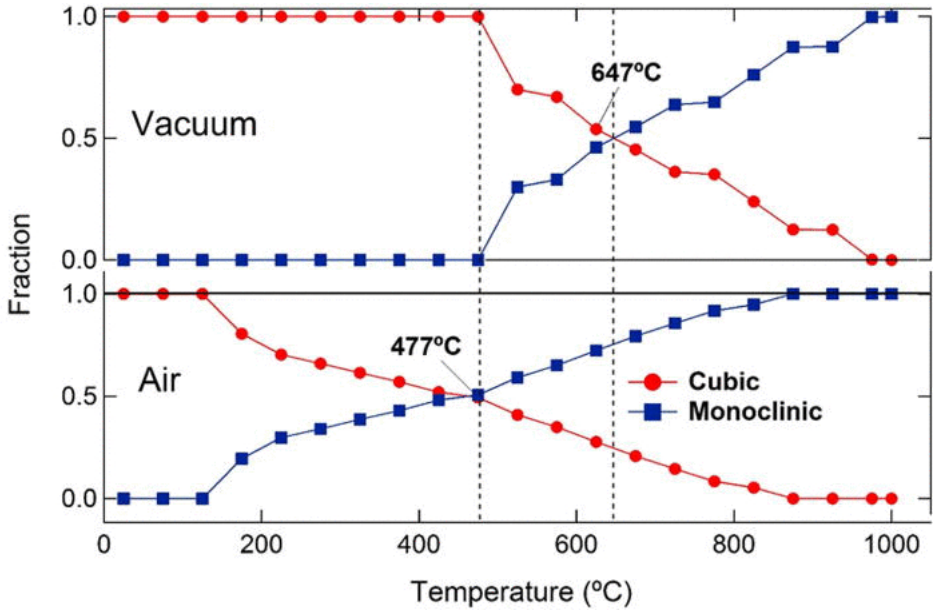

Figure 3.2: cubic and monoclinic fraction in air and vacuum at different temperature for nanostructured zirconia [30]

Their work emphasizes a different phase behavior and crystal growth in vacuum and in atmosphere under a specific thermal treatment. The samples were thermally annealed in air using an oven brought at the final temperature of 250-400-600-800 °C, respectively, applying a temperature ramp of 50 °C in 5 min, and maintaining the target temperatures constant for 2 h. The main effect of these two different environments is the presence of oxygen that can affect the stoichiometry of the material.

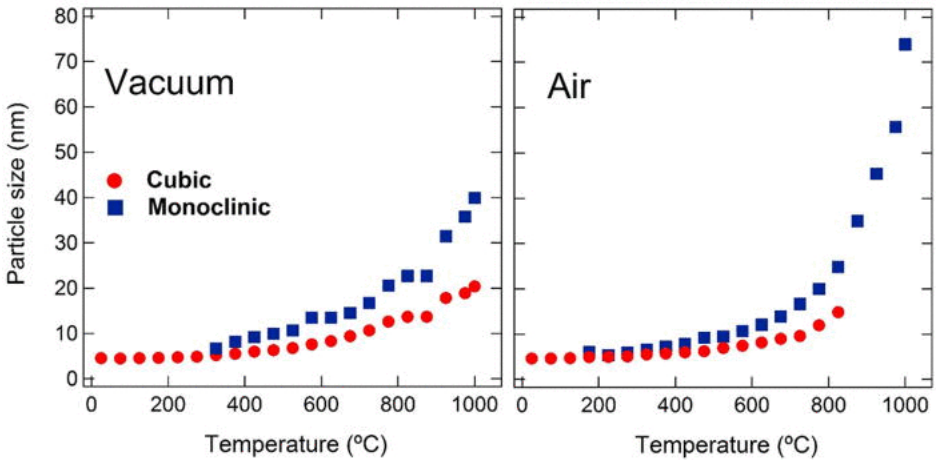

Figure 3.3: nanocrystal size in air and vacuum at different temperatures for nanostructured zirconia [30].

In this landscape, I have characterized nanostructured materials obtained by SCBD as described in Chapter 2 after thermal treatments. In particular, I have chosen two main temperatures, 110 °C and 400 °C , and kept these temperatures for different intervals of time in order to monitor the evolution. I have used Photoemission Electron Spectroscopy (PES) in order to have information about the oxidation state, X-ray Powder Diffraction (XRPD) for the phase, and nanocrystal size. In the experimental part, the presence of oxygen vacancies has been found and in order to understand the role of these vacancies I have performed some simulations about bulk zirconia with oxygen vacancies. In this way, I have studied what is the role of oxygen vacancies in the stabilization of tetragonal/cubic bulk phases with respect to monoclinic one and evaluated how much the vacancies can affect the bulk structure. The difference between nanostructure data and bulk simulation give us some information about the confinement effect on zirconia. Moreover, a simple confinement model has been applied to provide a rough estimation (about the order of magnitude) of the critical size of the nanocrystals. This is a preliminary study before a possible further development in which the confinement effect with a more refined model and surface interaction can be introduced.

Chapter 4

Characterization and Simulation Techniques

4.1 X-ray Photoelectron Spectroscopy

X-ray photoelectron spectroscopy (XPS) is a surface sensitive quantitative spectroscopic technique. It is used to determine the elemental composition, empirical formula, chemical states, and electronic state of elements present in a material. XPS is based on the photoelectric effect in which electrons, from the outer and inner core shells of the molecule, are emitted by electromagnetic radiation. This technique is a surface sensitive and non-destructive method to probe the first atom layers. The information depth of XPS is roughly on the order of up to 10 nm (depending on the material), but is the most sensitive in the first 4 nm. In the following sections, there is a brief description of the physical phenomena, spectra features in XPS measurements, fitting method, and schematic description of the used apparatus in this work.

4.1.1 Photoelectron Emission and Related Phenomena

In XPS, the photoelectric effect is used to investigate the binding energy E_B of the electrons in the sample. The molecules of a sample are exposed to X-rays with a defined energy, $h\nu$.If the energy is high enough, electrons can be emitted from the sample as shown in Fig. 4.1. Through a hemispherical spectrometer, the electrons emitted with a specific kinetic energy are counted. The binding

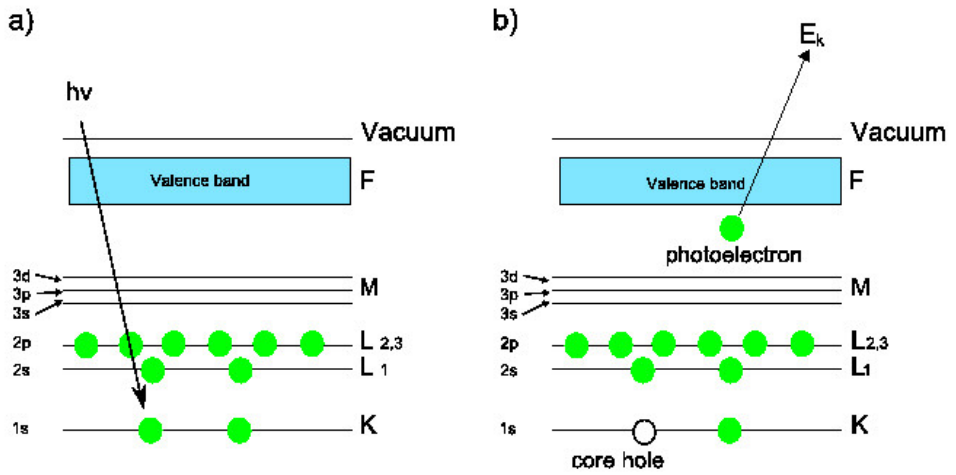

Figure 4.1: Photonemission

energy can be calculated as the difference between the energy of the X-ray and the kinetic energy:

$$E_B = h\nu - E_{kin} - \phi \tag{4.1}$$

where ϕ is the work function, i.e. a potential including surface potential of the sample and a correction factor to the actual referencing point for E_B. The general shape of the spectrum, considering only the main peak, is shown in Fig. 4.2. The step formed after peaks is due to inelastic collisions of photoelectrons. The binding energy of the peaks is specific for each orbital and element. Therefore, through XPS, it is possible to identify the elements present in a material. This energy can be shifted from the position of the pure element. This is due to a chemical shift. The nonequivalence of atoms can arise in several ways: difference in oxidation state, in molecular environment, lattice site, and so on. A simple model of this effect is the charge potential model. Considering a specific core level on atom with binding energy E_i, with valence charge density and mean radius of valence electron q_v and r_v, the binding energy is

$$E_i = E_i^O + \frac{q_v e^2}{r_v} + \sum_{i \neq j} \frac{q_i}{r_{ij}}. \tag{4.2}$$

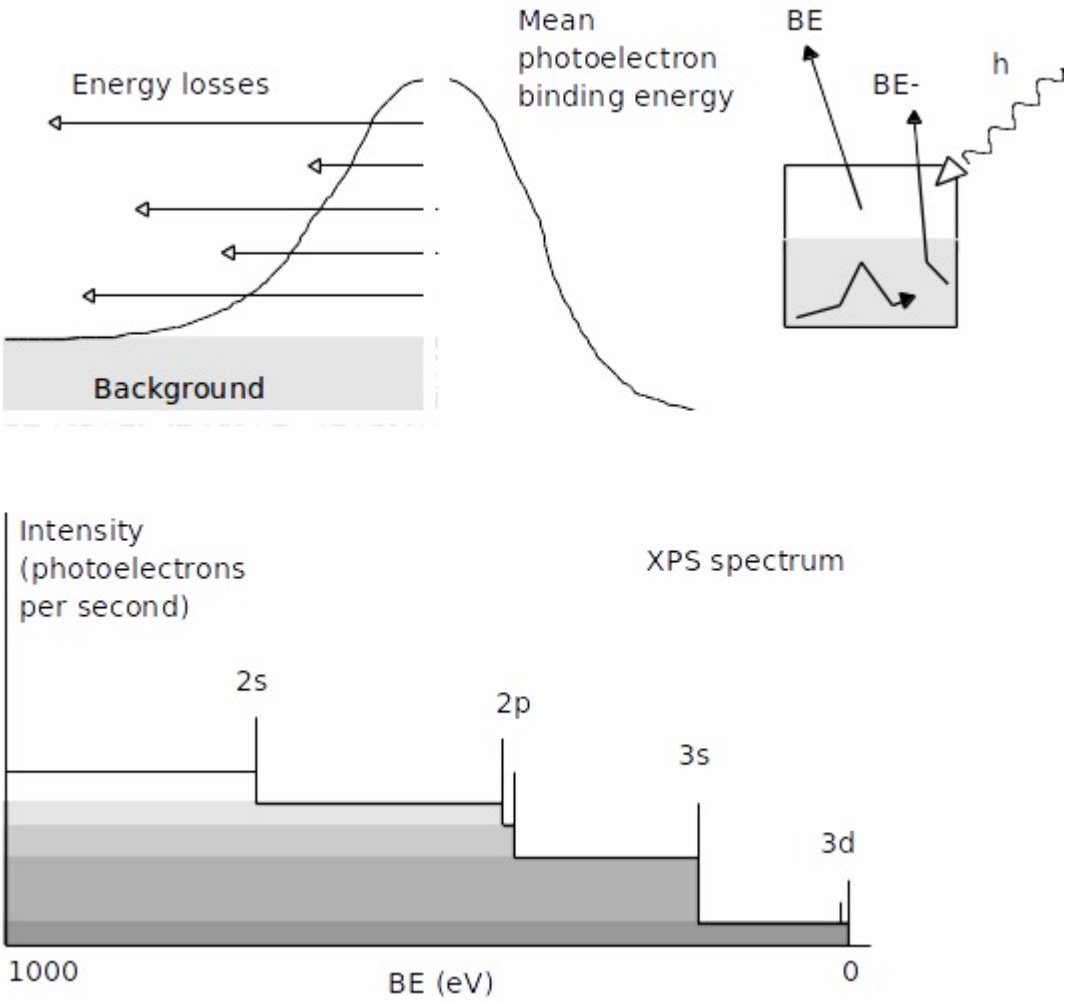

Figure 4.2: Schematic structure of XPS spectra

where E_i^O is a reference energy. A change in electron charge density Δq_v change the energy of all inner level

$$\Delta E_i = \frac{\Delta q_v e^2}{r_v} + \Delta \left(\sum_{i \neq j} \frac{q_i}{r_{ij}} \right). \tag{4.3}$$

This model involves a number of simplifications, for example the relaxation effects are neglected. Nevertheless, a simple interpretation of BE shifts based on the initial state concepts is extremely useful, especially for molecular solid. Recently, the shift of the XPS peaks has been better understood through the use of simulations. In particular in Ref. [70]the effect of the Madelung constant is emphasized, while a very recent work of Taucher et al. [71][52] has emphasized the role of variations in the electrostatic energy caused by collective electrostatic effects.

Auger lines are also recorded during XPS measurements. Auger electrons are emitted by a three electron process. First, a core hole is created and this hole is filled by a second electron from an outer shell. During this relaxation process, there is an energy release. This energy can be used to emit an electron with a binding energy E_B lower than the second electron as shown in Fig. 4.3. 4.3. Moreover, among these two main kinds of peaks there are other, different structures. X-ray satellites refer here to peaks due to non-monochromatic radiation of an ideally pure X-ray anode. Another phenomenon is the spin-orbital splitting that is based on an initial state effect due to the coupling of the electron spin momentum with its orbital angular momentum; this results in a splitting of the electron energy levels. Multiplet or exchange splitting requires unpaired electrons in the initial state of the atom. After photoemission, an unpaired electron remains in the core shell. This unpaired core electron can couple with the outer shells (spin-spin-coupling) and causes a multiplet splitting.
Any electron of sufficient energy passing through a solid can excite one or more modes of the collective oscillation of the sea of conduction electrons. The collective oscillation frequency is characteristic of the solid material and, therefore, needs characteristic energies for excitation. An electron that has given up an amount of energy equal to one of these characteristic energies is said to have suffered a plasmon loss because the harmonics of fundamentals can also be excited, but with progressively lower efficiency plasmon peaks repeat in constant energy distances with decreasing intensity.
Another structure that can appear in XPS spectra is a shake-up satellite. The loss of a photoemitted core level electron increases the nuclear charge filled by valences electrons that reorganize themselves. This reorganization, i.e. relaxation, can involve an excitation of one valence electron to a higher unoccupied level using part of the kinetic energy of the photoemitted electrons. In the relaxation of the valence electrons it can also happen that instead of filling a higher electron, the valence electron has enough energy to be ejected from the material. In this case, we call the spectral structure shake-off satellites. A third possibility of relaxation is that the valence electrons occupy a lower energy level

that is pulled down below another filled level in the presence of a core hole. The lower binding energy of the shake-down satellites compared to the main line is due to the improved screening of the core hole as a result of the shake-down process.

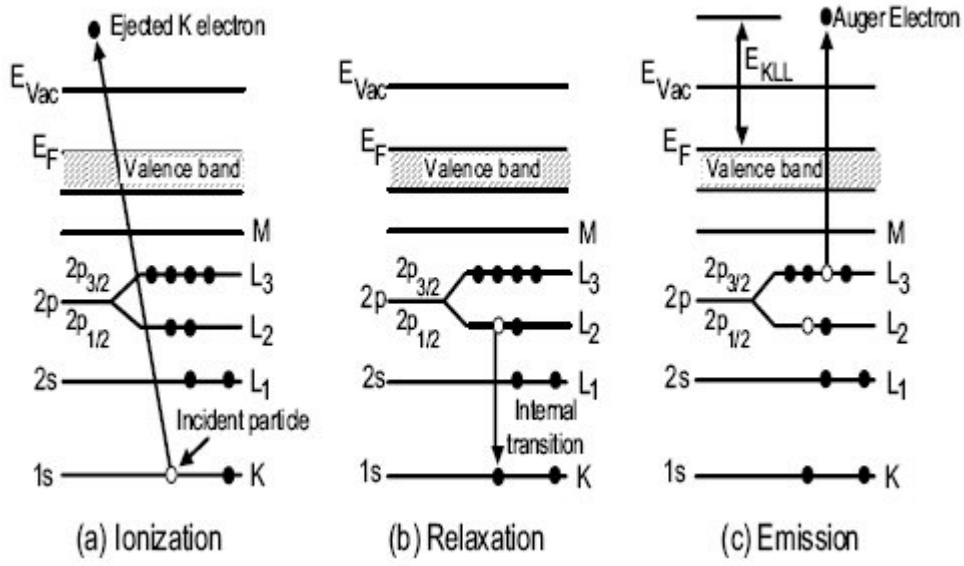

Figure 4.3: Auger emission

It is also possible to use the XPS measurement for quantitative analysis. The intensity of the peak is given by

$$I = nf\sigma\phi yAT\lambda \tag{4.4}$$

where f is the X-ray flux, σ is the photoelectric cross-section, ϕ is an angular correction factor, y is a photoelectron ground state efficiency factor, A is the area from which photoelectrons are detected, T is the efficiency of detection of emitted photoelectrons of that energy by the analyzer, λ is the electron attenuation length and n is the concentration of a given element. So

$$n = \frac{I}{f\sigma\phi yAT\lambda}. \tag{4.5}$$

We can introduce the sensitive factor from the first principle

$$S = f\sigma\phi yAT\lambda \tag{4.6}$$

but usually S is determined by an experimental approach and tabulated for each XPS apparatus. In this way,

$$n = \frac{I}{S}, \tag{4.7}$$

and from the area of the peak and the sensitive factor it is possible to calculate the number of atoms that contributed to the spectra and the relative quantity as the stoichiometry and relative concentration. However, before doing that, it is important to underline that the area of the peak considered in this quantitative analysis must be without the background contribution.

4.1.2 Fitting

In order to have more information from data, as for example different chemical binding involving an element, it is necessary to deconvolve the signals from the element regarding different binding. Before doing that it is necessary to determine the background contribution due to inelastic collisions of electrons.

4.1.2.1 Shirley background

From figure 4.1 we can see that the schematic structure of XPS spectra has a background due to energy losses. In order to evaluate the area of the peaks it is important to subtract the background. There are different models that we can use to fit the background as reported in Fig. 4.4. The last one is the Shirley background that was used in this work. The construction of this background involves the iterative process:

$$\begin{aligned} B_1(E) &= k_1 \int_E^{E_{right}} dE' \left[I(E') - I_{right}\right] \\ B_2(E) &= k_2 \int_E^{E_{right}} dE' \left[I(E') - I_{right} - B_1(E')\right] \\ B_n(E) &= k_n \int_E^{E_{right}} dE' \left[I(E') - I_{right} - B_{n-1}(E')\right] \end{aligned} \tag{4.8}$$

with $E_{left} \leq E < E_{right}$ where $B_n(E)$ is the n-th iteration of the Shirley background, E is the kinetic energy, k_n is the iterative value of the scattering

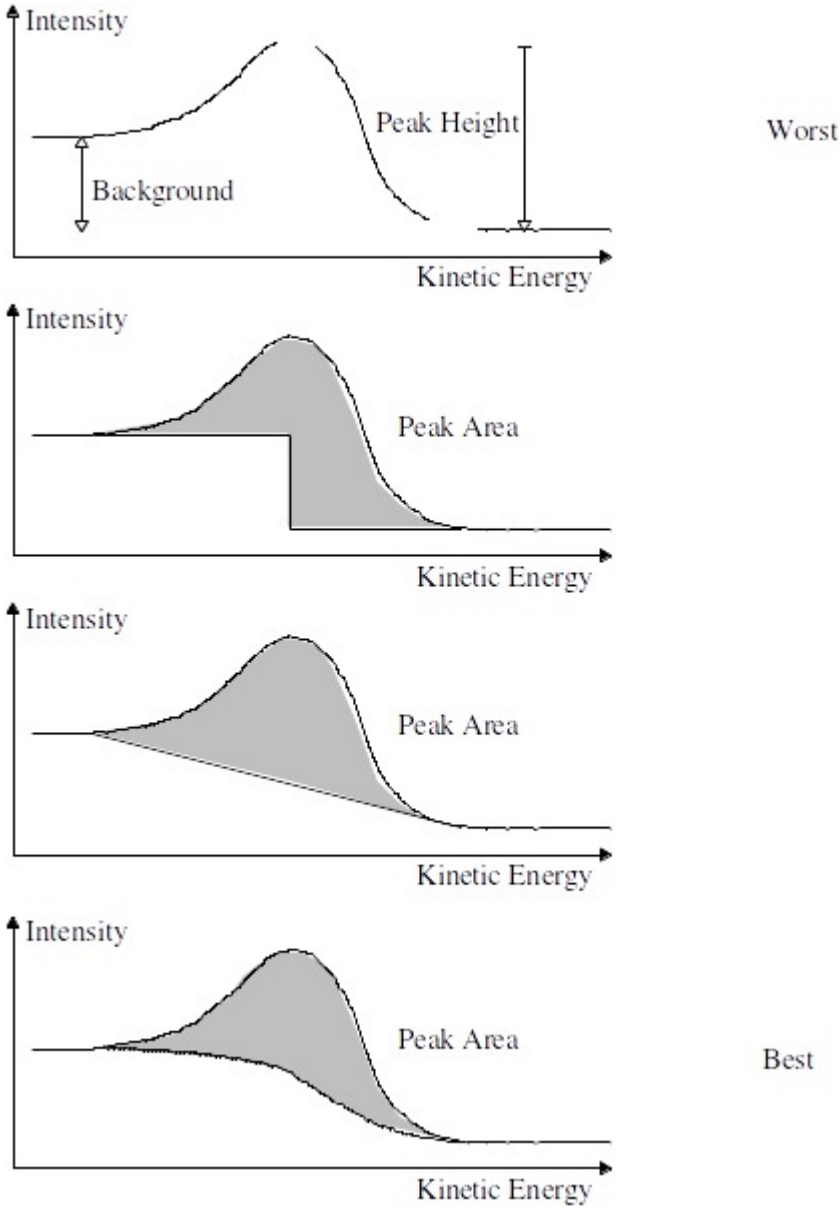

Figure 4.4: Different backgrounds

factor, and $I(E)$ is the photoelectric signal. At each iteration, the value of the scattering factor is chosen in such way that the total background goes through the elected point on the left (E_{left}, I_{left})

$$k_n = \frac{I_{left} - I_{right}}{\int_{E_{left}}^{E_{right}} dE' \left[I(E') - I_{right} - B_{n-1}(E') \right]}. \tag{4.9}$$

The total background is the sum of a constant term, equal to E_{right}, and the Shirley background. Outside the range indicated in the equation above, the Shirley background is equal to 0 for $E_{right} \leq E$, and to $I_{left} - I_{right}$ for $E \leq E_{left}$. This construction guaranties that the total background also passes through (E_{right}, I_{right}) since $B_n(E_{right}) = 0$ for every n.

4.1.2.2 Voigt profile

For fitting data we have use Voigt profile $V(x; \sigma, \gamma)$ that is a convolution between a Gaussian curve and a Lorentzian one.

$$V(x; \sigma, \gamma) = \int_{-\infty}^{\infty} G(y; \sigma) L(x - y; \gamma) dy \tag{4.10}$$

$$G(x; \sigma) = \frac{e^{-x^2/(2\sigma)}}{\sigma\sqrt{2\pi}} \tag{4.11}$$

$$L(x; \gamma) = \frac{\gamma}{\pi(x^2 + y^2)} \tag{4.12}$$

the FWHM of Gaussian, f_G, and Lorentzian profile, f_L are

$$f_G = 2\sigma\sqrt{2\ln(2)} \tag{4.13}$$

$$f_L = 2\gamma \tag{4.14}$$

The FWHM of the Voigt profile can be estimated

$$f_V \approx 0.5346 f_L + \sqrt{0.2166 f_L^2 + f_G^2} \tag{4.15}$$

that is exactly for a pure Gaussian profile and for a pure Lorentzian profile the error is of 0.000305%.

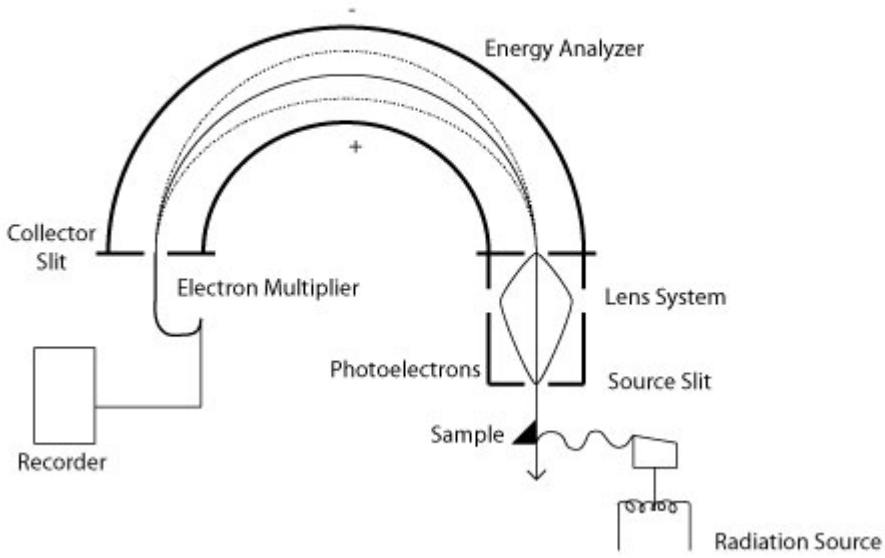

Figure 4.5: Schematic representation of an XPS device

4.1.3 Apparatus description

In Fig. 4.5, there is a schematic representation of the XPS apparatus. The main parts are: a vacuum chamber, an X-ray source, manipulator with sample holder, and an electron energy analyzer. XPS measurements require the detection of electrons ejected from the sample. These electrons need to encounter as few gas molecules as possible; otherwise, they will be scattered and lost for the analysis. Moreover, XPS is a surface technique that is very sensitive to contamination due to the gas environment. For these two reasons, it is necessary to work in an ultra-high vacuum (UHV) regime. In our device, the base pressure in the main chamber is 10^{-9} mbar.

The X-ray source used in our characterizations is Mg K_α (1253.6 eV) with a line width of 0.7 eV and relative intensity of 1. Other lines from the Mg source are Mg $K_\alpha 1$ 1261.8 eV with relativity intensity 0.086, Mg $K_\alpha 2$ 1263.2 with relativity intensity 0.062 and Mg K_β 1302.2 the intensity 0.01. These secondary energies in the X-ray can produce secondary peaks called satellites.
Our apparatus has a hemispherical electrostatic energy analyzer (HSA) represented in Fig.4.5. The emitted electron entering the HSA through the entrance slit, called source slit in Fig. 4.5, are deflected to elliptical trajectories by the radial electrical field between the inner hemisphere $R_{in} = 145$ mm and the outer hemisphere $R_{out} = 110$ mm. The entrance and exit slits are centered on the mean radius $R_0 = 127.5$ mm. Because the lens axis is tilted from the ground plate, the radial position R_0 is not equal to the nominal value of 127.5 mm but to the value of 126 mm. The potentials $-V_1$ and $-V_2$ are applied to the inner and outer hemisphere respectively, with V_2 greater than V_1. The potential $-V_0$ along the median surface is

$$V_0 = \frac{V_1 R_1 + V_2 R_2}{2R_0}. \tag{4.16}$$

If the electrons of energy $E = eV_0$ are injected tangentially to the medium surface at radius R_0 they will describe a circular orbit of radius R_0 according to the expression

$$V_i = V_0 \left[3 - 2\frac{R_0}{R_i} \right] \tag{4.17}$$

with $i = 1, 2$, we obtain

$$e\Delta V = E \left(\frac{R_2}{R_1} - \frac{R_1}{R_2} \right) \tag{4.18}$$

with $\Delta V = V_2 - V_1$. If the electron energy is put in the form $E = Ke\Delta V$ where K is spectrometer constant

$$K = \frac{R_{in}R_{out}}{2R_0(R_{out} - R_{in})} = 1.787. \tag{4.19}$$

The energy $E = Ke\Delta V$ is called pass energy and, from now on, it will be indicated as E_{pass}. In fact, only the electrons with energy E_{pass} impinging normal to the entrance slit of the analyzer describe a trajectory of radius $R_0 = (R_1 + R_2)/2$ and reach the exit slit, where they are revealed by the detector. If the electron are injected at $\delta\alpha$ to the tangential direction and with an energy ΔE different from the energy E_{pass}, the shift ΔR along the radius R_0 from the correct focal position is given by:

$$\Delta R = 2R_0 \left[\frac{\Delta E}{E_{pass}} - (\delta\alpha)^2 \right] \tag{4.20}$$

and the resolution is

$$\Delta E = E_{pass} \left(\frac{W_1 + W_2}{2R_0} + (\delta\alpha)^2 \right) \tag{4.21}$$

where W_1 and W_2 are the widths of the entrance and exit slit respectively. Though the resolution improves with increasing R_0, technical problems related to the size of the analyzer put a limit on the actual value R_0. Although a low pass energy E_{pass} improves the resolution, the electron transmission probability is reduced at low pass energy, and the signal-to-noise ratio deteriorates, accordingly.

4.2 X-ray Powder Diffraction

In the characterization of our materials, the X-ray diffraction technique is used. Diffraction occurs when light is scattered by a periodic array with a long-range order, producing constructive interference at specific angles. The atoms in a crystal are periodically arranged and, therefore, diffract light. The wavelength of the X-ray is similar to the distance between atoms. The Powder X-ray Powder Diffraction (XRPD) technique uses this principle to elucidate the crystalline nature of materials. The scattering of X-rays from atoms produces a diffraction pattern that contains information about the atomic arrangement in crystal. Amorphous materials like glass do not have a periodic array with long-range

order so they do not produce any significant peak in the diffraction pattern [72]. As shown in Fig. 4.6 the incident beam can be considered to be a planar wave. Beam 1 is reflected at atomic surface plane A, whereas the beam 2 is reflected at the very next one below atomic plane B. In both cases the incident beam is a planar way, and beams 1 and 2 are in phase before they reach the sample. After the reflection, beam 2 has to travel an extra distance, as represented by the sum of $\overline{MO_2} + \overline{M'O_2}$. From the illustration, clearly this distance is $\overline{MO_2} + \overline{M'O_2} = 2d \sin\theta$. To maintain the in-phase relationship between beams 1 and 2, and thereby achieve the constructive diffraction, the extra distance beam 2 travels has to be an integer number times the wavelength or $n\lambda$. This is called Bragg's law:

$$2d \sin\theta = n\lambda \tag{4.22}$$

where d is the periodicity of structure or in this case, the interatomic spacing; λ is the wavelength of the incident beam; θ is the incident angle and n is an integer. It is apparent that in order to achieve constructive diffraction, the periodic structure d will have to be on the same order of wavelength λ.
Given an incident X-ray beam with a certain wavelength λ, we can back-calculate the interatomic layer spacing d, which will help to reveal the chemical and phase information of the material. This method, derived from Bragg's law, has been widely used in materials characterization, especially for X-ray diffractometry. In this diffraction technique, a known wavelength of monochromatic X-ray radiation is used to determine the unknown spacing of materials. The specimen can be single crystals, polycrystals, or even powder. The intensity of the diffracted beam is recorded at different angles of θ to calculate the spacing and, therefore, identify the chemical and phase information of the material being studied.

If the phase difference $\overline{MO_2} + \overline{M'O_2} = 2d \sin\theta$ is half of the wavelength different or 180° out of phase, the two diffracted beams will completely cancel each other out, thereby leading to destructive interference. If the delta is a quarter of the wavelength different these two diffracted beams will not cancel each other. Beam 3, which is reflected by the atomic plane C that is directly below A and B , will be 180 degrees out of phase with beam 1 so that these two beams will cancel each other completely, while beam 2 will be canceled by beam 4, which is reflected by atomic layer D. Therefore, all of the beams will still cancel each other and we will observe a complete destructive interference at that angle of θ . From the preceding discussion, we can draw the following conclusion: for

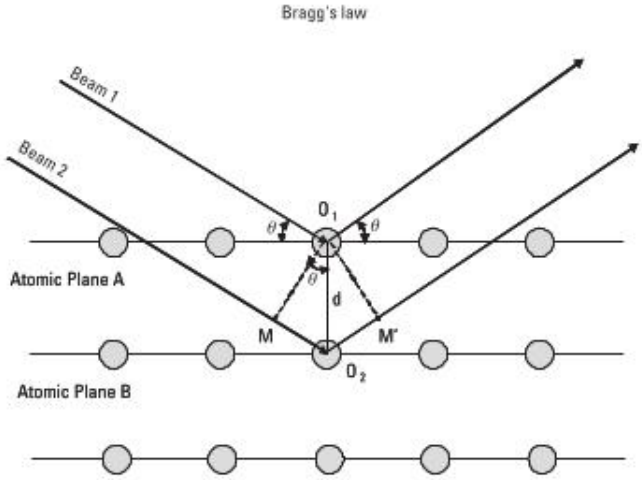

Figure 4.6: Illustration of Bragg's law [73].

a given set of crystallographic planes, any diffracted pattern will be observed at and only at an angle of θ according to Bragg's law. As soon as the angle deviates from θ, $\theta + \Delta\theta$, one can always find a layer that is $\frac{180}{\Delta\theta}$ layers below so that the reflected beams can cancel each other. Thus, in an ideal case, Bragg's law predicts that mathematically the X-ray powder diffraction pattern is a standard delta function as shown in Fig. 4.7(a). Diffraction can only be observed at the angle of θ for a given set of crystal planes. The preceding discussion is based on two assumptions. First, this is only true for ideal crystals that have infinite crystal planes and are defect free. As described earlier, when $\Delta\theta$ is small, one will need a large number of atomic layers below the surface to find the right one in order to completely form destructive infringement. Secondly, it also assumes that all reflected beams have the same amplitude regardless of how deep the atomic layers are below the surface. This is only true at the region near the surface, because the incident beam will be scattered inelastically and the amplitude will be dramatically decreased. Thus, in a real case of X-ray diffraction, when $\Delta\theta$ is small, the reflected beam from depth below will have a much smaller amplitude than the one on the surface and, therefor, the beams cannot completely cancel each other out. As a result, instead of a linear pattern like the delta function, we will observe a wave pack-like diffraction pattern with

a peak at the angle of θ but spreading to $\theta \pm \Delta\theta$ as shown in Fig. 4.7 (b). The total peak width is $2\Delta\theta$.

4.2.1 X-Ray Diffraction in Nanomaterials

Things get more interesting when the specimen is a nanocrystal or nanoparticle. First of all most of a nanocrystal's atoms are considered to be surface atoms. Secondly, nanoparticles or crystals have small particle or grain sizes and, therefor, a limited number of atomic planes. For example, if the interatomic layer distance d is 2.5 Å, nanocrystals with 5 nm only contain approximately 20 atomic layers. This is far less than what is needed to form complete destructive interference at the angle near θ. As a consequence, the peak at the angle of θ is greatly broadened and diffused and so the peak width $2\Delta\theta$ is much larger, Fig. 4.7(c). In fact, one can estimate the nanoparticle's or nanocrystal's grain size from the peak width[74]. From the first principle estimation, one can imagine that a 5-nm nanocrystal with 20 atomic layers will have a half-peak width $\Delta\theta$ of at least 9° ($180°/20 = 9°$). Therefore, the X-ray peak spreads across 18° around the angle of θ. This spreading will increase significantly when the particle size is even smaller. Normally, the full width at half-maximum (FWHM) measurement is used to characterize the diffraction peak and thereby estimate the grain or particle size. The extreme case of nanocrystals is glass, which has short-range order and long-range disorder. In this case, the peak is so broadened that all the peaks are connected and they can hardly be called peaks anymore this has been frequently observed in the amorphous X-ray diffraction pattern. Therefore, peak broadening is one of the key characteristics of X-ray diffraction on nanocrystals. From the width of a peak or more specifically the FWHM, one can obtain information about nanocrystal grain size or nanoparticle size. This method has been widely used in nanomaterial characterization. Note, however, that grain size is not the only cause for peak widening. Other factors, such as micro strains, will also cause peak widening.

From the XRPD analysis we can establish the crystal phases and their relative percentage. Moreover the size of the grains can be estimated through the Scherrer formula

$$d = \frac{K\lambda}{\beta \cos\theta} \tag{4.23}$$

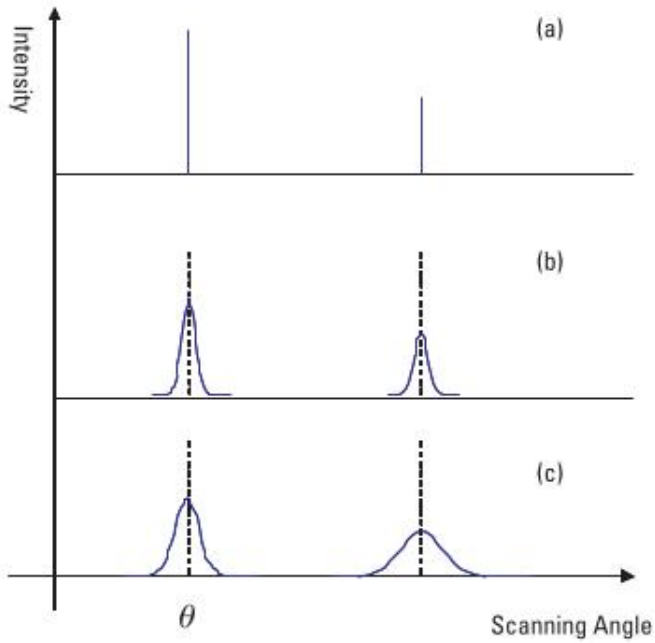

Figure 4.7: X-ray diffraction patterns: (a) linear pattern like the delta function in ideal crystals, (b) wave pack pattern in real crystals, and (c) diffused peak in nanocrystals.[73].

where d is the mean shape, k is a shape factor, λ is the X-ray wavelength, β is the line broadening at the half the maximum intensity (FWHM) after subtracting the instrumental line broadening and θ is the Bragg angle. The FWHM can be expressed in terms of X parameters using a fitting procedure where $\beta = \frac{X}{cos\theta}$ Actually the formula that was used here was:

$$d = \frac{18000\lambda}{\pi X} \tag{4.24}$$

where $\frac{18000}{\pi}$ is the conversion from centi-deg to radians.

4.2.2 Apparatus description

In Fig. 4.8, a schematic representation of the apparatus that is used for the XRPD measurements is reported. The main part is the X-ray source, that in our case, was the Mo X-ray source ($\lambda = 0.710$ Å), sample holder, and X-ray detector. The samples were contained in glass capillaries and the diffractions were collected in transmission geometry with sample to detector distances of 80 mm. The X-ray detector was a Charge Coupled Device (CCD).

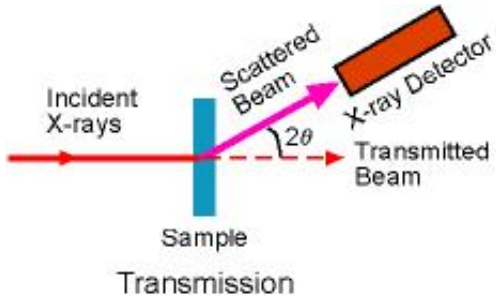

Figure 4.8: Schematic illustration of X-ray diffraction apparatus

4.3 Density Functional Theory

In order to determine the ground state of a material from $ab-initio$ simulation we need to know the eigenfunction of a many-body Hamiltonian. In case of materials in crystal form we can divide the contribution to Hamiltonian by ions and electrons [75]

$$\left(\hat{T}_e + \hat{T}_{io} + \hat{V}_{e-e} + \hat{V}_{e-io} + \hat{V}_{io-io}\right)\psi = i\hbar\partial_t\psi \tag{4.25}$$

with the eigenfunction $\psi = \psi\left(\boldsymbol{R}_1, \boldsymbol{R}_2 ..., \boldsymbol{R}_N; \boldsymbol{r}_1, \boldsymbol{r}_2 ..., \boldsymbol{r}_n; t\right)$ depend on the ions, $\boldsymbol{R}_i$, and electrons, $\boldsymbol{r}_i$, positions. $\hat{T}_e$ and $\hat{T}_{io}$ are the kinetic energy of n electrons

and N ions respectively.

$$\begin{aligned} \hat{T}_e &= -\sum_{i=1}^{n} \frac{\hbar^2 \nabla_i^2}{2m} \\ \hat{T}_{io} &= -\sum_{i=1}^{N} \frac{\hbar^2 \nabla_i^2}{2M} \end{aligned} \tag{4.26}$$

while the Columbian potentials are

$$\begin{aligned} \hat{V}_{e-e} &= \frac{1}{2} \sum_{i \neq j} \frac{e^2}{|\boldsymbol{r}_i - \boldsymbol{r}_j|} \\ \hat{V}_{io-io} &= \frac{1}{2} \sum_{i \neq j} \frac{e^2}{|\boldsymbol{R}_i - \boldsymbol{R}_j|} \\ \hat{V}_{e-io} &= -\sum_{i=1}^{n} \sum_{j=1}^{N} \frac{e^2}{|\boldsymbol{R}_j - \boldsymbol{r}_j|} \end{aligned} \tag{4.27}$$

that describe the electron-electron, ion-ion and electron-ion interaction respectively.
Due to the huge number of variables that cannot be separated the system described in 4.25 is not resolvable even with the actual computing power. We can use some approximations. First of all we can uncouple the ions and electrons dynamic using the adiabatic or Born-Oppenheimer approximation. In this approximation we can consider the ionic lattice at rest and so the ionic variables became parameters. In this way the electronic part can be described by the Hamiltonian

$$\left(\hat{T}_e + \hat{V}_{e-e} + \hat{V}_{e-io}\right) \psi = i\hbar \partial_t \psi. \tag{4.28}$$

and $\hat{V}_{e-io}$ can be treated as an external potential. This approximation is not enough to resolve the system for the great number of variable.
We can use the Density Functional Theory(DFT) in order to face this problem. The starting point of this theory is the Hohenberg-Kohn theorem: for any system constituted by interacting particles, for a fixed the interaction, with non-degenerate ground-state there exists a bijective relation among the external potential (up to an arbitrary additive constant), the ground-state many-body wave-function and the ground-state density of the system,

$$\hat{V}_{est} \iff |\psi_0\rangle \iff n_0(\boldsymbol{r}). \tag{4.29}$$

So we can describe a system in the ground state using the density in this way the number of variables is reduced. From the non-degeneracy of the ground state follows that to an external potential correspond only one ground-state eigenfunction $|\psi_0\rangle$. Now, we prove that $|\psi_0\rangle$ cannot be the eigenfunction of two different Hamiltonian in which the external potentials are different to within an additive constant. Suppose that there are two different external potentials that have the same ground state wavefunction:

$$\begin{aligned} \hat{H} + \hat{V}_{est} |\psi_0\rangle &= E_0 |\psi_0\rangle \\ \hat{H} + \hat{V}'_{est} |\psi'_0\rangle &= E'_0 |\psi'_0\rangle . \end{aligned} \tag{4.30}$$

If we subtract the two previous equations, assuming that the wavefunction is different from zero only in a subspace of null measure, we obtain

$$\hat{V}_{est} - \hat{V}'_{est} |\psi_0\rangle = E_0 - E'_0 |\psi_0\rangle \tag{4.31}$$

This means that the two potentials can differ only up to a constant that anyway is irrelevant as the total energy of a system is always determinate up to an additive constant. Now, we show that given a ground state density there exists a unique wavefunction that determines such a density. Suppose that there exist two different ground states $|\psi_0\rangle$ and $|\psi'_0\rangle$. This implied two different external potentials

$$\begin{aligned} \hat{H}_{tot} &= \hat{H} + \hat{V}_{est} \\ \hat{H}'_{tot} &= \hat{H} + \hat{V}'_{est}. \end{aligned} \tag{4.32}$$

Considering the density expectation value in the ground state

$$n_0 (\boldsymbol{r}) = \langle \psi_0 | \sum_i \delta (\boldsymbol{r} - \boldsymbol{r}_i) |\psi_0\rangle \tag{4.33}$$

The external potential for a multi-body system can be expressed as the sum of the potentials that act on a single particle

$$\hat{V}_{est} = \sum_i \hat{v}_{est} (\boldsymbol{r}_i) . \tag{4.34}$$

Than, the external potential expectation value in the ground state using the equation (4.33) becomes

$$\langle \psi_0 | \hat{V}_{est} |\psi_0\rangle = \int d\boldsymbol{r} v_{est} (\boldsymbol{r}) n_0 (\boldsymbol{r}) . \tag{4.35}$$

Is a well-known fact that the non-degenerate expectation value of Hamiltonian using the ground-state eigenfunction is strictly minor of the expectation value using any other eigenfunction

$$\begin{aligned} \langle\psi_0|\,\hat{H}_{tot}\,|\psi_0\rangle &< \langle\psi_0'|\,\hat{H}_{tot}\,|\psi_0'\rangle \\ \langle\psi_0'|\,\hat{H}_{tot}'\,|\psi_0'\rangle &< \langle\psi_0|\,\hat{H}_{tot}'\,|\psi_0\rangle \end{aligned} \tag{4.36}$$

if the densities are the same, we will have an absurd. Suppose that E_0 and E_0' are the energy of the fundamental state for the first and second Hamiltonian of (4.32) respectively, than

$$\langle\psi_0'|\,\hat{H}_{tot}\,|\psi_0'\rangle = \langle\psi_0'|\,\hat{H} + \hat{V}_{est}' + \hat{V}_{est} - \hat{V}_{est}'\,|\psi_0'\rangle = E_0' + \langle\psi_0'|\,\hat{V}_{est} - \hat{V}_{est}'\,|\psi_0'\rangle\,. \tag{4.37}$$

using (4.35) in (4.37)

$$\left\langle\bar{\psi}_0\right|H_e\left|\bar{\psi}_0\right\rangle = E_0' + \int d\boldsymbol{r}\,(v_{est}\,(\boldsymbol{r}) - v_{est}'\,(\boldsymbol{r}))\,n_0'\,(\boldsymbol{r}) \tag{4.38}$$

with

$$n_0'\,(\boldsymbol{r}) = \langle\psi_0'|\sum_i \delta\,(\boldsymbol{r} - \boldsymbol{r}_i)\,|\psi_0'\rangle\,. \tag{4.39}$$

In the same way we obtain

$$\langle\psi_0|\,\hat{H}_{tot}'\,|\psi_0\rangle = E_0 - \int d\boldsymbol{r}\,(v_{est}\,(\boldsymbol{r}) - v_{est}'\,(\boldsymbol{r}))\,n_0\,(\boldsymbol{r})\,. \tag{4.40}$$

Using this result in (4.36)

$$\begin{aligned} E_0 &< E_0' + \int d\boldsymbol{r}\,(v_{est}\,(\boldsymbol{r}) - v_{est}'\,(\boldsymbol{r}))\,n'\,(\boldsymbol{r}) \\ E_0' &< E_0 - \int d\boldsymbol{r}\,(v_{est}\,(\boldsymbol{r}) - v_{est}'\,(\boldsymbol{r}))\,n\,(\boldsymbol{r}) \end{aligned} \tag{4.41}$$

and adding the two previous expressions, in the hypothesis $n'\,(\boldsymbol{r}) = n\,(\boldsymbol{r})$,

$$E_0 + E_0' < E_0' + E_0 \tag{4.42}$$

that is absurd. So if the external potential is different then the density on the ground-state is also different. Using the Hohenberg-Kohn theorem we can

express the expectation value of any observables as a function of the density. In our case for the energy of a system of interaction electrons

$$\begin{aligned} E[n(\boldsymbol{r})] &:= \langle \psi_0[n(\boldsymbol{r})] | \hat{T}_e + \hat{V}_{e-e} + \hat{V}_{est} | \psi_0[n(\boldsymbol{r})] \rangle \\ &= T_e[n(\boldsymbol{r})] + V_{e-e}[n(\boldsymbol{r})] + \int d\boldsymbol{r} v_{est}(\boldsymbol{r}) n(\boldsymbol{r}) \end{aligned} \tag{4.43}$$

and minimizing this functional we can obtain the energy of the fundamental state. So, for the fundamental state, we can use the density of state instead of the eigenfunction.

4.3.1 Kohn and Sham equation

With the Hohenberg-Kohn theorem, if we know the energy functional we can know the ground-state of the Hamiltonian using the density. This theorem was used by Kohn and Sham. They considered an auxiliary system of non-interactive particles with an effective potential such that the density is the same of the interacting system. In this way, the auxiliary Hamiltonian gives the Schrödinger equations of a single particle. Using the second quantization formalization, we can write the density in terms of the field operator:

$$\hat{n}(\boldsymbol{r}) = \hat{\psi}^\dagger(\boldsymbol{r})\hat{\psi}(\boldsymbol{r}) \tag{4.44}$$

the interaction potential is

$$\hat{V}_{e-e} = \frac{1}{2} \int d\boldsymbol{r} d\boldsymbol{r'} \frac{e^2}{|\boldsymbol{r} - \boldsymbol{r'}|} \hat{\psi}^\dagger(\boldsymbol{r'})\hat{\psi}^\dagger(\boldsymbol{r})\hat{\psi}(\boldsymbol{r})\hat{\psi}(\boldsymbol{r'}). \tag{4.45}$$

Using the anticommutator of fermionic field

$$\begin{aligned} \left\{ \hat{\psi}(\boldsymbol{x}), \hat{\psi}(\boldsymbol{y}) \right\} = \left\{ \hat{\psi}^\dagger(\boldsymbol{x}), \hat{\psi}^\dagger(\boldsymbol{y}) \right\} = 0 \\ \left\{ \hat{\psi}(\boldsymbol{x}), \hat{\psi}^\dagger(\boldsymbol{y}) \right\} = \delta(\boldsymbol{x} - \boldsymbol{y}) \end{aligned} \tag{4.46}$$

from which

$$\begin{aligned} \hat{\psi}^\dagger(\boldsymbol{r'})\hat{\psi}^\dagger(\boldsymbol{r})\hat{\psi}(\boldsymbol{r})\hat{\psi}(\boldsymbol{r'}) = -\hat{\psi}^\dagger(\boldsymbol{r'})\hat{\psi}^\dagger(\boldsymbol{r})\hat{\psi}(\boldsymbol{r'})\hat{\psi}(\boldsymbol{r}) = \\ -\delta(\boldsymbol{r} - \boldsymbol{r'})\hat{\psi}^\dagger(\boldsymbol{r'})\hat{\psi}(\boldsymbol{r}) + \hat{\psi}^\dagger(\boldsymbol{r'})\hat{\psi}(\boldsymbol{r'})\hat{\psi}^\dagger(\boldsymbol{r})\hat{\psi}(\boldsymbol{r}) \end{aligned} \tag{4.47}$$

using this last relation in (4.45) and considering the expectation value [76]

$$V_{e-e}[n] = \frac{1}{2} \int d\boldsymbol{r} d\boldsymbol{r'} \frac{e^2}{|\boldsymbol{r} - \boldsymbol{r'}|} n(\boldsymbol{r'})n(\boldsymbol{r}) - \frac{1}{2} \int d\boldsymbol{r} d\boldsymbol{r'} \frac{e^2 \delta(\boldsymbol{r} - \boldsymbol{r'})}{|\boldsymbol{r} - \boldsymbol{r'}| n(\boldsymbol{r'})} n(\boldsymbol{r})n(\boldsymbol{r'}). \tag{4.48}$$

In equation (4.48) the first addendum is the Hartree term that is the energy of the mean field due to the electrons. Therefore, in Kohn and Sham effective potential we can isolate this term. The energy functional of the auxiliary system is

$$E'[n] = T'[n] + E_{e-io}[n] + E_H[n] + E_{xc}[n] \tag{4.49}$$

where T' è is the non-interactive system kinetic energy, E_{e-io} is the energy of the external potential that is the same of the interactive system, E_H è is Hartree energy, E_{xc} is the difference between the energy functional of the auxiliary and interactive system. For the interactive system the energy functional is

$$E\left[n\right] = T[n] + E_{e-io}[n] + E_{e-e}[n] \tag{4.50}$$

from the difference between this functional and the one in (4.49)

$$E_{xc}[n] = T[n] - T'[n] + E_{e-e}[n] - E_H[n], \tag{4.51}$$

so the exchange-correlation term E_{xc} has inside the interaction. In order to have a non-interactive system this term can be approximate in different way. The more widespread approximation, and the one used in this work, is the local density approximation (LDA)[77] in which the exchange-correlation functional is approximated with the local relation

$$E_{xc} \approx \int d\boldsymbol{r} n\left(\boldsymbol{r}\right) \epsilon_{xc}^{omo}\left[n\left(\boldsymbol{r}\right)\right], \tag{4.52}$$

where $\epsilon_{xc}^{omo}\left[n\right]$ is the exchange-correlation energy for an electron in a homogeneous electron with density n. Now we can use the variational principle to determine the fundamental-state energy. The decoupling of the electron in an auxiliary system implies that the eigenfunction is the product of the one-particle eigenfunctions. Considering the orthonormal constraint between the single particle eigenfunctions

$$\langle\phi_i|\phi_j\rangle = \delta_{ij} = \int d\boldsymbol{r}\phi_i(\boldsymbol{r})\phi_j(\boldsymbol{r}), \tag{4.53}$$

using the Lagrange multiplier and the partial derivative respect the eigenfunction instead of the density

$$\frac{\delta}{\delta\phi_i^*\left(\boldsymbol{r}\right)} = \frac{\delta n\left(\boldsymbol{r}\right)}{\delta\phi_i^*\left(\boldsymbol{r}\right)}\frac{\delta}{\delta n\left(\boldsymbol{r}\right)} = \phi_i\left(\boldsymbol{r}\right)\frac{\delta}{\delta n\left(\boldsymbol{r}\right)} \tag{4.54}$$

we have

$$\frac{\delta E'[n]}{\delta \phi_i^*(\boldsymbol{r})} = \left(\frac{\delta T'[n]}{\delta n(\boldsymbol{r})} + \frac{\delta E_{e-io}[n]}{\delta n(\boldsymbol{r})} + \frac{\delta E_H[n]}{\delta n(\boldsymbol{r})} + \frac{\delta E_{xc}[n]}{\delta n(\boldsymbol{r})} \right) \phi_i = \epsilon_i \phi_i. \tag{4.55}$$

For the auxiliary system, we have

$$\left(\frac{-\nabla^2}{2m} + \hat{V}_{eff} \right) \phi_i(\boldsymbol{r}) = \epsilon_i \phi_i(\boldsymbol{r}), \tag{4.56}$$

and in the function of the density the effective potential is

$$\hat{V}_{eff} = \hat{v}_{e-io} + \hat{v}_H + \hat{v}_{xc} \tag{4.57}$$

with

$$\hat{v}_H = \int d\boldsymbol{r}' \frac{e^2 n(\boldsymbol{r}')}{|\boldsymbol{r} - \boldsymbol{r}'|} \tag{4.58}$$

supposing

$$E_{xc} = \int d\boldsymbol{r} \epsilon_{xc}(n(\boldsymbol{r})) n(\boldsymbol{r}) \tag{4.59}$$

the contribution of exchange-correlation term to the effective potential is

$$\hat{v}_{xc} = \hat{\epsilon}_{xc} + \int d\boldsymbol{r}' \frac{\partial \hat{\epsilon}_{xc}(\boldsymbol{r}')}{\partial \hat{n}(\boldsymbol{r})} \hat{n}(\boldsymbol{r}'). \tag{4.60}$$

In this way we have obtained a resolvable single particle Schrödinger equation. The more used electron simulation programs use this method using a self-consistent calculation. The Kohn and Sham effective potential (4.57) is calculated from a test density and solving the relative Schrödinger equation (4.56) we obtain a new density that is used again as test density for the calculation of a new Kohn and Sham effective potential. Through the iteration of these passages we can achieve a self-consistency and the true density of the system.

4.3.2 Relaxation

Using the DFT we can also perform calculation about the optimum geometry. In order to do that we can calculate the force acting between the atoms inside the cell and minimize it. In this case we have to act on the ions position and restore the dependency of the eigenstate from the ions coordinate $\boldsymbol{R}_i$. Using

the Hellman Feynman theorem we can calculate the forcing acting on a I ions through the formula

$$\boldsymbol{F}_I = -\frac{d}{d\boldsymbol{R}_I} \langle\psi| H |\psi\rangle \tag{4.61}$$

and using the eigenstate of the Hamiltonian $H|\psi\rangle = E|\psi\rangle$

$$\boldsymbol{F}_I = -\langle\psi| \frac{\partial H}{\partial \boldsymbol{R}_I} |\psi\rangle - E\frac{\partial \langle\psi|\psi\rangle}{\partial \boldsymbol{R}_I} = -\langle\psi| \frac{\partial H}{\partial \boldsymbol{R}_I} |\psi\rangle . \tag{4.62}$$

So starting for specific cell parameters and atom positions, after a self-consistent calculation of the electronic part of the Hamiltonian, we can calculate the forces acting between atoms and change the cell parameters and atoms position if the forces are far from zero value. Trough iteration of this calculation we can achieve the optimization of the structure.

4.3.3 Plane waves

We have seen that with Kohn and Sham equation 4.56 we can reduce a many-body Hamiltonian to a single particle Schrödinger equation with eigenfunction $\phi_i(\boldsymbol{r})$. This eigenfunction can be expanded on a basis set $f_a(\boldsymbol{r})$

$$\phi_i(\boldsymbol{r}) = \sum_{a=1}^{N_b} c_{ia} f_a(\boldsymbol{r}). \tag{4.63}$$

On this basis the Schrödinger equation became

$$\sum_b H_{ab} c_{ib} = \epsilon_i c_{ia} \tag{4.64}$$

and to solve the equation we have to diagonalize the matrix H_{ab} of size $N_b \times N_b$. A good choose of the basis, i.e. fast for a computational point of view, accurate and easy is the plane waves $e^{i\boldsymbol{k}\cdot\boldsymbol{r}}$. Moreover for a periodic system we can use the Bloch's Theorem that allows you to rewrite the wave as a product of a plane wave and a periodic function $u_{i,\boldsymbol{k}}(\boldsymbol{r}) = u_{i,\boldsymbol{k}}(\boldsymbol{r}+\boldsymbol{R})$, where $\boldsymbol{R}$ is the lattice vector

$$\phi_{i,\boldsymbol{k}}(\boldsymbol{r}) = e^{i\boldsymbol{k}\cdot\boldsymbol{r}} u_{i,\boldsymbol{k}}(\boldsymbol{r}). \tag{4.65}$$

We can expand $u_{\boldsymbol{k}}(\boldsymbol{r})$ on a plane wave bases set

$$u_{i,\boldsymbol{k}}(\boldsymbol{r}) = \frac{1}{\Omega} \sum_{\boldsymbol{G}} c_{i,\boldsymbol{k}+\boldsymbol{G}} e^{i\boldsymbol{G}\cdot\boldsymbol{r}} \tag{4.66}$$

with $\boldsymbol{G}$ reciprocal lattice vector. In this way

$$\phi_{i,\boldsymbol{k}}(\boldsymbol{r}) = \frac{1}{\Omega}\sum_{\boldsymbol{G}} c_{i,\boldsymbol{k}+\boldsymbol{G}} e^{i(\boldsymbol{k}+\boldsymbol{G})\cdot\boldsymbol{r}} \tag{4.67}$$

where $c_{i,\boldsymbol{k}+\boldsymbol{G}}$ are a complex numbers. Therefor, in the momentum space, the Kohn-Sham equations are equivalent to solve

$$\sum_{\boldsymbol{G'}} H_{\boldsymbol{k}+\boldsymbol{G},\boldsymbol{k}+\boldsymbol{G'}} c_{i,\boldsymbol{k}+\boldsymbol{G'}} = \epsilon_{i,\boldsymbol{k}} c_{i\boldsymbol{k}+\boldsymbol{G}} \tag{4.68}$$

diagonalizing the matrix

$$H_{\boldsymbol{k}+\boldsymbol{G},\boldsymbol{k}+\boldsymbol{G'}} = -\frac{\hbar^2}{2m}|\boldsymbol{k}+\boldsymbol{G}|^2\delta_{\boldsymbol{G},\boldsymbol{G'}} + V_{eff}(\boldsymbol{G},\boldsymbol{G'}). \tag{4.69}$$

In principle the dimension of the plane-wave basis set should be infinite. Numerically we truncate the expansion including only the reciprocal lattice vectors that fulfill the condition:

$$\frac{\hbar^2|\boldsymbol{k}+\boldsymbol{G}|^2}{2m} \leq E_{cut}. \tag{4.70}$$

It corresponds to assuming that the contribution to V_{eff} is negligible compared to that of lower frequency plane-waves. The main disadvantage of plane-waves is that for tightly bound electrons need a huge number of plane waves to achieve an adequate expansion. This problem can be overcome by using the pseudopotential approximation.

4.3.4 Pseudopotential Approximation

Near ions the strong ionic Coulomb potential causes rapid oscillations of the eigenfunction. This implies a very high energy cut off in the plain wave expansion. In the approximation in which the chemical bounding does not affect the core region of the atoms (frozen core approximation), it is possible replace the strong ionic potential with a weaker pseudopotential that gives identical valence electron wavefunctions outside the core region, $r > r_c$.

Moreover norm-conserving pseudopotentials are constructed to enforce the condition that, including inside the cut-off radius, the total norm of the pseudowavefunction is identical to the corresponding true wavefunction

$$\int_{r<r_c} drr^2|\psi(r)|^2 = \int_{r<r_c} drr^2|\psi_{ps}(r)|^2. \tag{4.71}$$

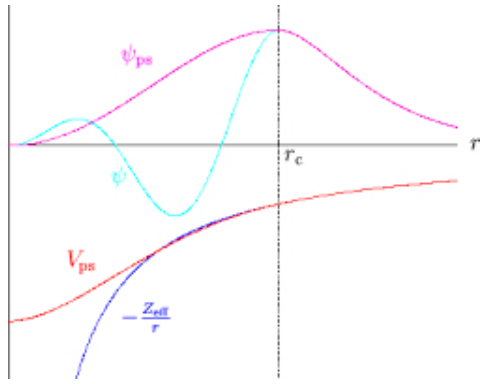

Figure 4.9: Schematic illustration of pseudopotential. Real ionic potential is the blue line and the real wavefunction is shown light blue, the red and magenta lines are the pseudopotential and the pseudo wavefunction respectively

Target of this technique is to produce $transferrable$ pseudopotential, i.e. pseudopotential that can be used in different chemical environment, which can be used with computationally reasonable number of plane waves.

Part II
Results and discussion

Chapter 5

Characterization and Simulation of Zirconia in the Literature

In the last two decades nanosctrutered zirconia, without dopant, has attracted attention for its stability in cubic or tetragonal form at room temperature. As mentioned in Chapter 3, the different production modes give different characteristics for zirconia. The grain size, which is a parameter on which the crystal phase depends, is very sensitive to the preparation condition. This also affects the behavior in thermal treatment as shown in Ref. [65]. For zirconia prepared by SCBD, there is a recent publication with some characterization after thermal treatments by Borghi et al. [30]. Borghi et al. annealed the sample in air and vacuum at the final temperatures of 250-400-600-800 °C, respectively, applying a temperature ramp of 50 °C in 5 min, and maintaining the target temperatures constant for 2 h. The resulting percentage of cubic and monoclinic phase and nanocrystal size changes with the environment. Whether changing the time in reaching and keeping a target temperature leads to materials with different stoichiometry, crystal phase, and nanocrystal size was studied.
Point defects in the stabilized zirconia system have been extremely topical in theoretical studies, which focus on ion mobility, thermal properties,and the interaction between dopant cations and oxygen vacancies [78]. In Ref.[79] there is an extensive study through simulation about the nature of the oxygen defect, both interstitial oxygen and oxygen vacancies (V_O) in monoclinic pure zirconia

considering different charge states of the defects. According to the literature we denote with V_O^0, V_O^+,V_O^{+2}, the neutral, single, charged, and double charged oxygen vacancy, respectively. In particular the neutral vacancy has a doubly occupied one-electron energy level deep in the forbidden gap and is strongly localized [79]. In Ref.[80] on the basis of ab initio simulations of monoclinic Zirconia, the authors computed the formation energy of oxygen vacancies as a function of the Fermi energy within the Zirconia band-gap. They found that, for Fermi energy in the gap within a range up to approx 1.5 eV lower than the conduction band minimum, the neutral oxygen vacancy is energetically favored with respect to charged oxygen vacancies, while the opposite is true for lower value of the Fermi energy. Qualitatively similar results were obtained by Zheng et al. [81] computing the formation energy of oxygen vacancies as a function of the Fermi level at different chemical potential. They found a range in which the V_O^0 is favored with respect to the charged defect the is significantly larger the one of Ref. [80]. Remarkably, in their work Zheng et al. [81] find that when the Fermi level is constrained remain within the band gab of silicon, the neutral oxygen vacancies are energetically favored with respect to the charged ones. In Ref. [78] the lattice and energy level modifications by neutral oxygen vacancies in tetragonal zirconia are studied.
In this work we want to see how the density of vacancies affect the crystal phase. This is a preliminary study, and in first approximation we neglected charge vacancies with the associated difficulty to treat the Coulomb interaction between charge vacancies and their image charges. In the following, to shorten the notation, we will denote the neutral oxygen vacancy by V_O.

Chapter 6

Zirconia Sample Description

In the landscape presented in Chapter 3, ns-ZrO_2 samples were prepared by SCBD as described in Chapter 2 on crystalline silicon substrate. The samples have a thickness of 180 nm and a roughness r.m.s. of 25±4 nm. In order to evaluate the possible evolution of this material under thermal treatment, I have characterized different samples as reported in Fig.6.1.

Starting from the characterization of the deposited material, hereinafter referred to as received material, , some samples were heated until 110 °C in 30 min. at atmosphere pressure.I have kept samples at this temperature for different times and next I have made a slowly cooled down the room temperature, as shown in green line in Fig. 6.1. The same procedure has been made for 400 °C, which was reached in 30 minutes, shown as a magenta line in Fig. 6.1. I have also varied the timing in which the temperature of 400 °C was reached and after I slowly cooled the room temperature, as shown in Fig. 6.1. Moreover, I treated a sample until 800 °C in 4 hours and sustained this temperature for 6 hours before the cooling process. All of these treatments have been made with samples exposed to air. In order to confirm the role of oxygen in the thermal evolution, I used a treatment of ns-ZrO_2 powder closed in a capillary for XRPD measurement, reaching a temperature of 400 °Cbefore cooling. In this way, the interaction with oxygen was limited. All of these treatments are shown in Table 6.1.

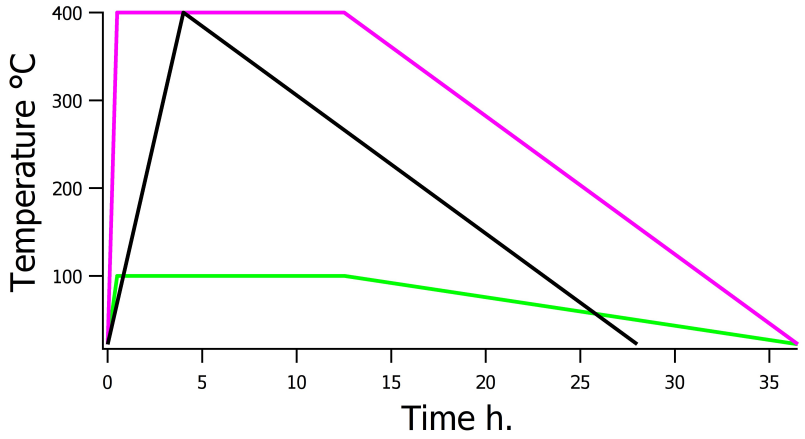

Figure 6.1: three examples of thermal treatments.

From the XPS characterization, some information about the stoichiometry of the surface of the material can be obtained by using the sensitive factor as described in Chapter 4.1 and using the Formula 4.7.
From the XRPD characterization, the crystal phase and relative concentration of each phase can be evaluated. Moreover, the unit cell parameters can be evaluated. The powder for the XRPD analysis has been prepared after thermal treatment on silicon substrate and then put in a quartz capillary. A sample was treated on glass substrates before putting the powder in the capillary. For another sample, I prepared the capillary before the thermal treatment in order to emphasize the oxygen and the substrate influence on phase transformation.
In the next three Chapters, I will illustrate the XPS, XRPD, and simulated results emphasizing the different kinds of information that each technique gives, and try to connect the obtained results in an organic view, when possible, for the behavior under thermal treatment of zirconia nanostructured thin film.

sample name	description	characterization
as received	thickness: 180 nm roughness: 25 nm no thermal treatment	XPS XRPD

sample name	description	characterization
30 min 110 °C	from room temperature to 110 °C in 30 min. cooling in 24 hours on crystalline SiO_2 substrate	XPS XRPD
30 min 110 °C 12 h	from room temperature to 110 °C in 30 min. at 110 °C for 12 hours cooling in 24 hours on crystalline SiO_2 substrate	XPS XRPD
30 min 110 °C24 h	from room temperature to 110 °C in 30 min. at 110 °C for 24 hours cooling in 24 hours on crystalline SiO_2 substrate	XPS XRPD
30 min 110 °C 72 h	from room temperature to 110 °C in 30 min. at 110 °C for 72 hours cooling in 24 hours on crystalline SiO_2 substrate	XPS XRPD
30 min 400 °C 1 h	from room temperature to 400 °C in 30 min. at 400 °C for 1 hour and cooling in 24 hours on crystalline SiO_2 substrate	XPS XRPD
30 min 400 °C 2 h	from room temperature to 400 °C in 30 min. at 400 °C for 2 hours and cooling in 24 hours on crystalline SiO_2 substrate	XPS
30 min 400 °C 4 h	from room temperature to 400 °C in 30 min. at 400 °C for 4 hours and cooling in 24 hours on crystalline SiO_2 substrate	XPS XRPD

sample name	description	characterization
30 min 400 °C 12 h	from room temperature to 400 °C in 30 min. at 400 °C for 12 hours and cooling in 24 hours on crystalline SiO_2 substrate	XPS XRPD
30 min 400 °C 24 h	from room temperature to 400 °C in 30 min. at 400 °C for 24 hours and cooling in 24 hours on crystalline SiO_2 substrate	XPS XRPD
30 min 400 °C 72 h	from room temperature to 400 °C in 30 min. at 400 °C for 72 hours and cooling in 24 hours on crystalline SiO_2 substrate	XPS XRPD
30 min 400 °C 72 h glass	from room temperature to 400 °C in 30 min. at 400 °C for 72 hours and cooling in 24 hours on glass substrate	XRPD
1 h 400 °C	from room temperature to 400 °C in 1 hour and cooling in 24 hours on crystalline SiO_2 substrate	XPS
3 h 400 °C	from room temperature to 400 °C in 3 hours and cooling in 24 hours on crystalline SiO_2 substrate	XPS
4 h 400 °C	from room temperature to 400 °C in 3 hours and cooling in 24 hours on crystalline SiO_2 substrate	XPS
4 h 400 °C capillary	from room temperature to 400 °C in 3 hours and cooling in 24 hours in closed quartz capillary	XRPD

sample name	description	characterization
4 h 800 °C 6 h	from room temperature to 800 °C in 4 hours for 6 hours and cooling in 24 hours in closed quartz capillary	XRPD

Table 6.1: sample name, description, and characterization

Chapter 7

Zirconia X-ray Photoelectron Spectroscopy Results

I have made an XPS analysis of the samples described in the previous chapter. With this kind of analysis, I can have chemical composition information from the surface, with a maximum depth of 10 nm. It is also possible to determine the stoichiometry of the samples through the analysis of peak areas with a sensitive factor. As described in the details in Chapter 4, photoemission spectra were acquired with ultra-high vacuum (UHV) chamber having a conventional X-ray source (Leybold LHS 10/12 Mg K_α = 1253.6 eV). The system is equipped with a hemispherical electron analyzer, (EA11 MCD). The spectra were acquired in constant pass-energy mode E_p = 30eV. The overall resolution was 0.9eV. All the spectra are referenced to the Fermi level and the binding energy scale is calibrated via the Au 4f7/2 core level line (84.0eV) of a clean polycrystalline Au sample. The line shapes are fitted with mixed singlets and obtained by Voigt profiles that are sited on a Shirley background using the KolXPD software [82].The Gaussian contribution on full width half maximum (FWHM) profiles is taken fixed at 1.2eV while the Lorentzian contribution is different for a different orbital. This choice is made considering that the major Gaussian contribution to the shape is due to the apparatus while the Lorentzian contribution is due to a whole lifetime [70]. I have also used the typical constraint of ratio intensity due to spin splitting. For the orbital, there is a ratio of 2 : 3.

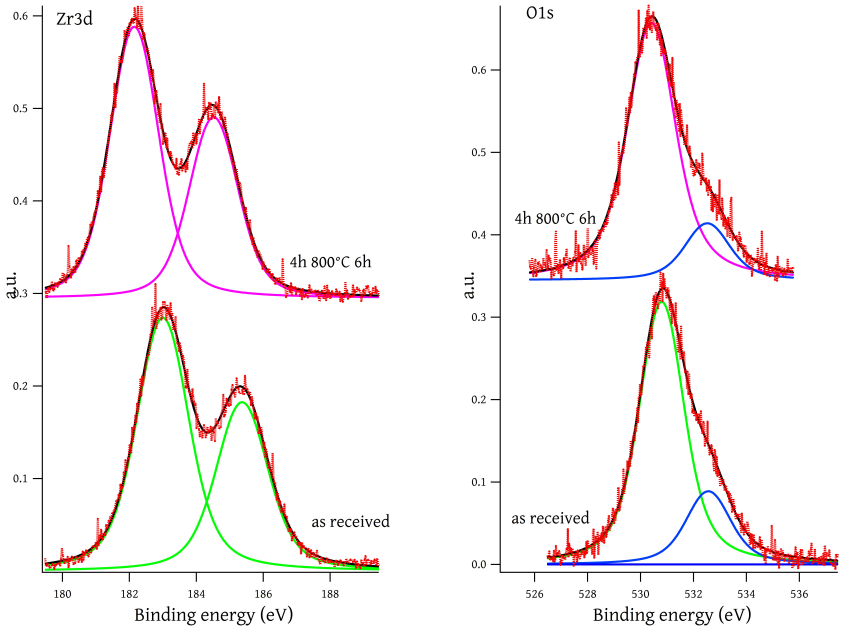

Figure 7.1: XPS spectra of (a) Zr3d and (b) O1s for the as received and thermal treatment to 800 °C samples.

From XPS data the as recevied sample $Zr3d_{5/2}2$ data can be fitted with one doublet at 183eV as shown in Fig 7.1a in green. In the same figure there is reported data of a thermal treated sample brought to 800 °C in 4 hours and kept at 800 °C for 6 hours before the annealing. In this case the data can be fitted with one doublet at 182.51eV (magenta). The Lorentzian contribution to FWHM 0.75eV and 0.58eV for the as received and thermal treated, respectively. From the XPRD data, illustrated in the next chapter, the sample is composed by cubic zirconia while the 800 °C treated sample is composed by monoclinic zirconia, the different position in binding energy, $\Delta E = 0.49eV$, of the $Zr3d_{5/2}$

doublet in this two samples can be due to the different crystal form. The shifting peaks to due crystal phase are also reported in Basahel et al. [83] with $\Delta E = 0.11eV$. The difference in the shift between this data and Basahel et al. data can be explained considering the oxygen spectra reported in Fig.7.1b. The as received and thermal treated sample to 800 °C have two main signals from the O1s spectra; the blue peaks indicate the link to oxygen bound with adventitious carbon and the other ones are linked to zirconium. As reported in Table 7.1, the O1s green peak of the has received sample has a binding energy of 530.8eV, while the magenta O1s peak of the thermally treated sample has a binding energy of 530.45eV. The Lorentzian contribution to FWHM is 1eV and 1.23eV for the as received and thermal treated sample, respectively. Evaluating the stoichiometry, through a sensitive factor that is 0.98 for Zr3d5/3 and 0.61 for the O1s signal, of the as received material this is 1.61, so we have $ZrO_{1.61}$, while the sample treated at 800 °C it is 2, i.e. stoichiometric zirconia, ZrO_2. A suboxide can shift a peak to lower bending energy this can be the reason for the greater difference in binding energy between cubic and monoclinic phase in our work as it respects to the Bashel et al. [83] results. Moreover, they report, for oxygen peaks, that the monoclinic one is a higher binding energy than the cubic one. For oxygen, the substoichiometry shifts the peak to a higher binging energy and this effect can explain the fact that in our spectra the cubic substoichiometry peak has a higher binding energy than the monoclinic one.

sample	**element**	**position**	**phase**	**stoichiometry**	**cubic phase**
as received	Zr $3d_{5/2}$ O1s	183.00 530.8	cubic	1.61	100%
4 h 800 °C 6 h	Zr $3d_{5/2}$ O1s	182.51 530.45	monoclinic	2.00	0%

Table 7.1: as received and 800 °C sample peak position of XRD

I have treated the zirconia samples at 110 °C reached in 30 minutes and kept the material at this temperature for different intervals of time before cooling in 24 hours. In the XPS spectra of Zr3d, as shown in Fig. 7.2a, regarding the fixed shape of the green doublet as in the as received spectra, it is necessary to introduce another peak for the thermal treated sample data. Keeping the same

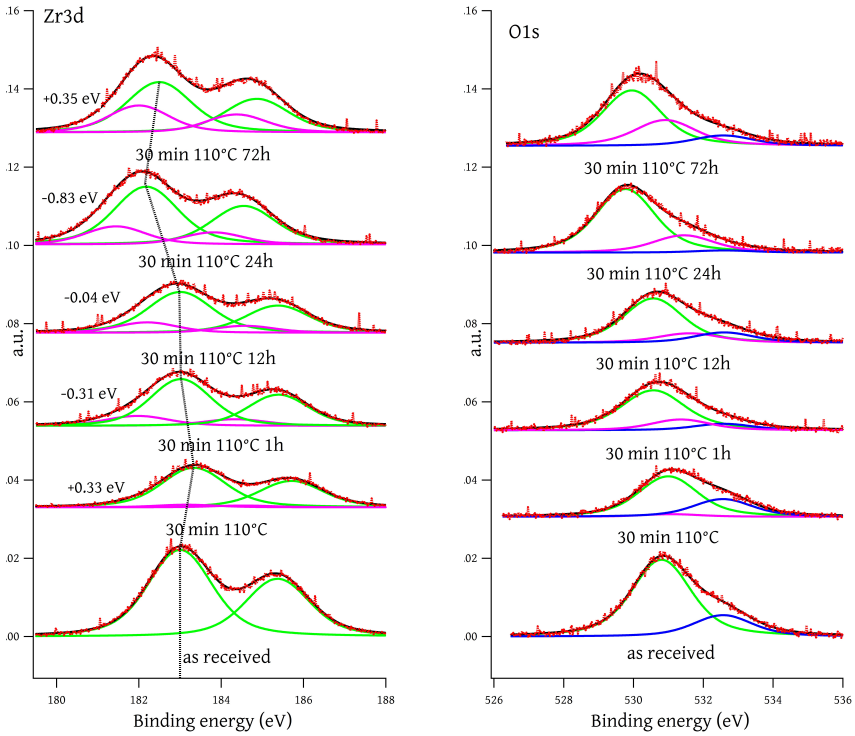

(a) (b)

Figure 7.2: XPS spectra of (a) Zr3d and (b) O1s for sample treated at 110 °C. Numbers near spectrum are the shift in eV for green peak respect the previous spectra from down to upper

Lorentzian width of the as received material for the green peaks of O1s and Zr3d the new peaks, the magenta ones in Fig. 7.2b and 7.2a, in a fitting procedure assume the same Lorentzian width of the monoclinic peak found in the sample treated at 800 °C that are 0.58 eV for Zr3d and 1.23 for O1s. The O1s magenta peak's intensity increases coherently with the intensity of the magenta Zr peaks. This is a strong indication that these two structures are linked. Moreover, in Fig. 7.1a, we can see that the cubic peak has a higher binding energy than the monoclinic one, as for the green and magenta peak in Fig. 7.2a. The shape

and doublet position in the Zr spectra are compatible with an identification of the green peak with cubic phase and magenta peak with monoclinic phase. On the other hand the green and magenta oxygen peaks in Fig. 7.2b switch position compared with the ones in Fig. 7.1b. This can be due to the electronic environment effect of the coexistence of two different phases. Another hint that there are some electronic environment effects that come from the shift of Zr green doublet with thermal treatment. Comparing the as received sample with the thermal treated sample heated at 110 °C and cooled right after, the Zr3d green peak is shifted at higher binding energy, as shown in Fig. 7.2a by a vertical dashed line. This shift is consistent with an increase of the oxygen content which is found when evaluating the stoichiometry as reported in Table 7.2 and in Fig. 7.3a.

sample	**element**	**position**	**phase**	**stoichiometry**	**cubic like**
as deposited	Zr $3d_{5/2}$ O1s	183.00 530.8	cubic	1.61	100%
30 min 110 °C	Zr $3d_{5/2}$ O1s	183.33 530.99	cubic like	1.86	94%
	Zr $3d_{5/2}$ O1s	182.16 531.08	monoclinic like	2.00	
30 min 110 °C 1 h	Zr $3d_{5/2}$ O1s	183.02 530.56	cubic like	1.88	81%
	Zr $3d_{5/2}$ O1s	181.96 531.35	monoclinic like	2.00	
30 min 110 °C 12 h	Zr $3d_{5/2}$ O1s	182.98 530.54	cubic like	1.97	81%
	Zr $3d_{5/2}$ O1s	182.17 531.58	monoclinic like	2.00	
30 min 110 °C 24 h	Zr $3d_{5/2}$ O1s	182.15 530.41	cubic like	2.00	78%
	Zr $3d_{5/2}$ O1s	181.41 530.74	monoclinic like	2.00	
30 min 110 °C 72 h	Zr $3d_{5/2}$ O1s	182.5 529.96	cubic like	2.00	67%
	Zr $3d_{5/2}$ O1s	182.01 530.92	monoclinic like	2.00	

Table 7.2: XPS position of the thermal treated sample at 110 °C

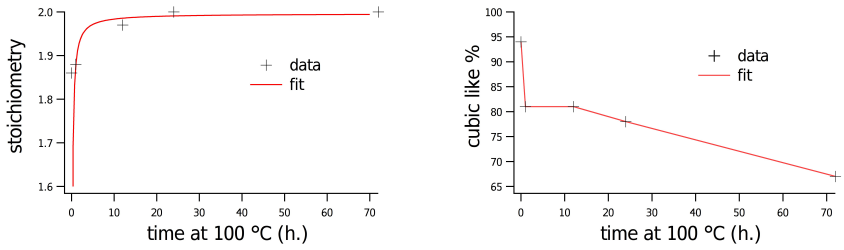

(a) (b)

Figure 7.3: stoichiometry (a) and cubic-like phase (b) in the function of time at 110 °C

Increasing the time in which the sample was kept to 110 °C oxidation and the percentage of the magenta peak increase while the binding energy of the green peak shift to a lower binding energy. This means that the position of the green peak is influenced by the presences of the magenta peak in the opposite direction with respect to the oxidation process. This is confirmed also by the comparison of the sample kept at 110 °C for 24 hours. So the XPS shifts are not only due to chemical change, but also to the electronic environment as proposed in Ref.[71]. Even if we are far away from a secure assignation, the shape and relative position of Zr3d green peak seems to be compatible with cubic phase, while the magenta peak seems to be compatible with the monoclinic phase. So, from now on, the magenta peaks will be called monoclinic-like and the green one cubic-like.

Using the amplitudes of monoclinic-like peaks of Zr and O, Fig. 7.2b and 7.2a, for all the samples, the stoichiometry is of 2. Instead, the cubic-like peaks present an evolution in stoichiometry for different treatment as shown in Fig 7.3a. The oxidation of the cubic-like phase increase until it reaches the value of 2, that is a full oxide zirconium ZrO_2, after 12 hours. From Fig.7.3b we can see that for the sample stored at 100 °C for one hour the relative percentage of the cubic-like phase decreases by 19% compared to the sample as received. The same amount of cubic-like phase has been found in the sample kept for 12 hours at 110 °C. While for a longer time the cubic phase decreases with a linear behavior. Table 7.2 summarizes the peak position, stoichiometry and cubic-like percentage of the samples treated at 110 °C.

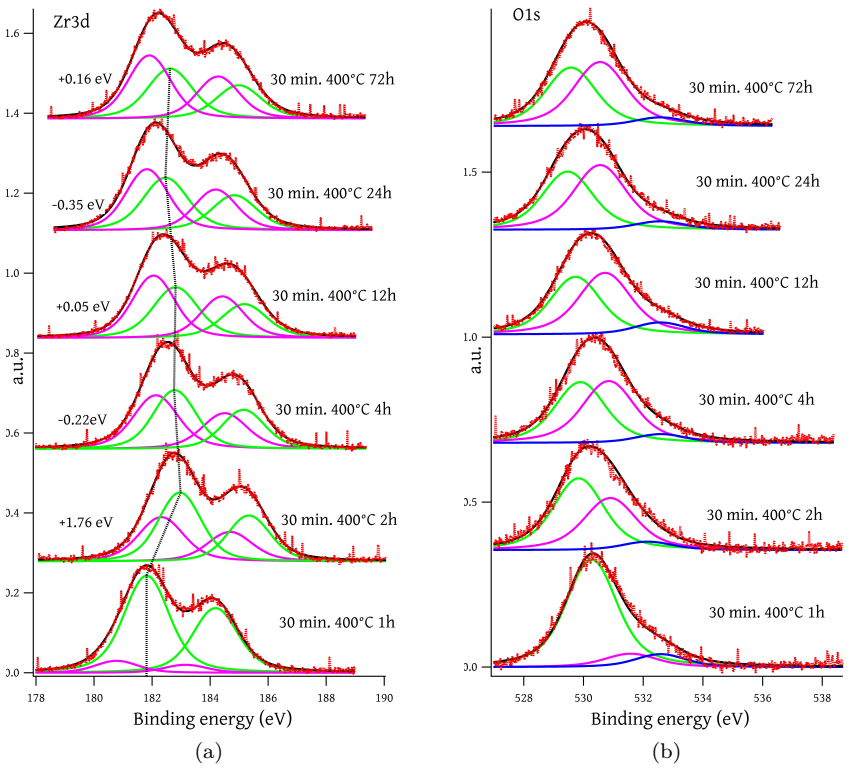

Figure 7.4: XPS spectra of (a) Zr3d and (b) O1s for sample treated at 400 °C in 30 minutes. The numbers near spectrum are the shift in eV for the green peak respect the previous spectra from down to upper

I have also treated some samples at 400 °C, reached in 30 minutes and kept at this temperature for different intervals of times. The XPS spectra are reported in Fig.7.4a and 7.4b for Zr3d and O1s. The dashed vertical line shows the cubic-like shift respect the previous samples which is the one just below. In this case, we also have competitive phenomena: shift toward a higher binding energy by oxidation, and a shift to lower binding energy by changing the electronic environment. In this case, there was a cubic-like phase decrease, thereby

increasing the time in which we kept the material at 400 °C until 12 hours. For longer times, the relative percentage of cubic-like phase does not change anymore and remains fixed at 46% as shown in Fig. 7.5b. The stoichiometry has a similar behavior with a linear increasing until I kept the samples at 400 °C for time less than 12 hours in which the full oxidation is reached as shown in Fig. 7.5a. Therefor, in case we heated at 400 °C for 30 minutes after 12 hours at this temperature the phase and the stoichiometry of the surface are stable. Table 7.3 summarizes the peak position, stoichiometry and cubic-like percentage of the samples treated at 400 °C.

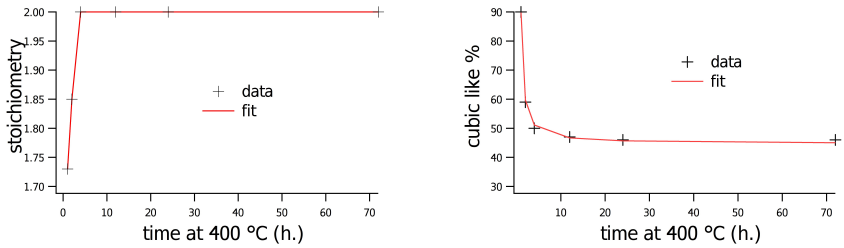

(a) (b)

Figure 7.5: stoichiometry (a) and cubic-like phase percentage (a) in the function of the time at 400 °C

sample	**element**	**position**	**phase**	**stoichiometry**	**cubic like**
30 min 400 °C 1 h	Zr $3d_{5/2}$	181.81	cubic like	1.73	90%
	O1s	530.25			
	Zr $3d_{5/2}$	181.46	monoclinic like	2.00	
	O1s	531.56			
30 min 400 °C 2 h	Zr $3d_{5/2}$	182.98	cubic like	1.85	59%
	O1s	530.25			
	Zr $3d_{5/2}$	182.33	monoclinic like	2.00	
	O1s	531.31			
30 min 400 °C 4 h	Zr $3d_{5/2}$	182.76	cubic like	1.86	50%
	O1s	529.87			

sample	element	position	phase	stoichiometry	cubic like
	Zr $3d_{5/2}$ O1s	182.11 530.82	monoclinic like	2.00	
30 min 400 °C 12 h	Zr $3d_{5/2}$ O1s	182.81 529.74	cubic like	2.00	47%
	Zr $3d_{5/2}$ O1s	182.05 530.72	monoclinic like	2.00	
30 min 400 °C 24 h	Zr $3d_{5/2}$ O1s	182.46 529.47	cubic like	2.00	46%
	Zr $3d_{5/2}$ O1s	181.82 530.56	monoclinic like	2.00	
30 min 400 °C 72 h	Zr $3d_{5/2}$ O1s	182.62 529.58	cubic like	2.00	46%
	Zr $3d_{5/2}$ O1s	181.91 530.56	monoclinic like	2.00	

Table 7.3: XPS position of the thermal treated sample at 400 °C reached in 30 minutes

In Fig. 7.6a and 7.6b, the XPS spectra of Zr3d and O1s are reported for samples brought to 400 °C in different times and then cooling to room temperature in 24 hours. In this case, the sample is stoichiometric if we reach 400 °C at least in 1 hour. While the relative percentage of cubic-like phase decrease with increasing the time in which the target temperature is reached with a linear behavior as shown in Fig.7.7 at least until we reach the target temperature in 4 hours.

Summarizing from the XPS data, we can see that the as received sample is substoichiometric, $ZrO_{1.61}$. Thermal treatments induced an oxidation and zirconia becomes stoichiometric. The time spent to reach the stoichiometric depends on the annealing temperature. The sample heated in 30 minutes to 110 °C becomes stoichiometric in 24 hours, while the sample heated in 30 minutes to 400 °C becomes stoichiometric in 12 hours. The stoichiometric also depends on the time used for reaching the target temperature. In fact bringing the sample to 400 °C in 30 minutes give a substoichiometric sample while if I heat to the

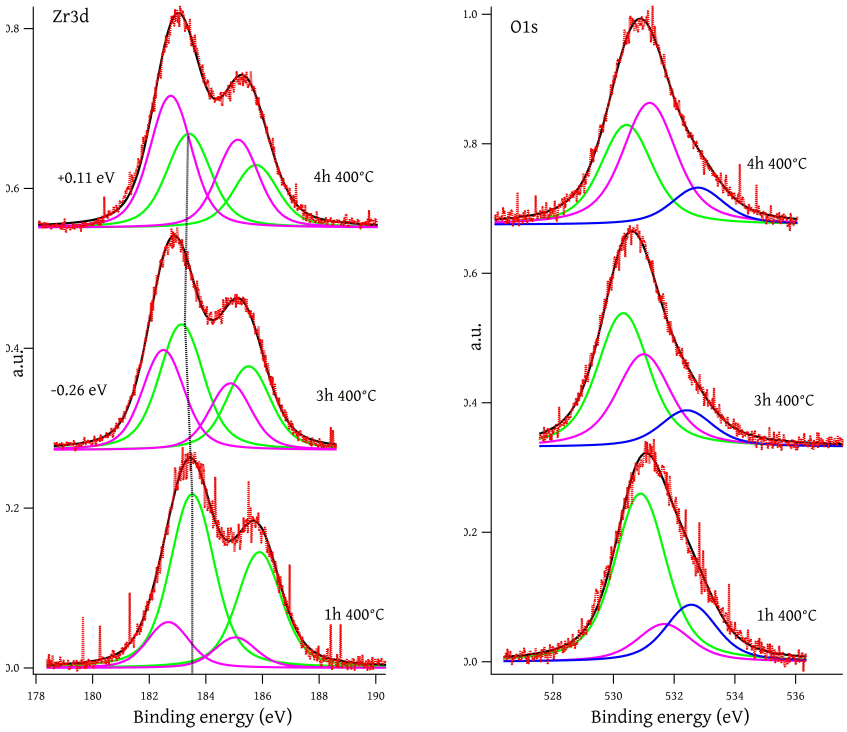

Figure 7.6: XPS spectra of (a) Zr3d and (b) O1s for the sample treated at 400 °C. The numbers near the spectrum are the shift in eV for the green peak respect the previous spectra from down to upper

same temperature in 1 hour the sample is stoichiometric. In the thermal treatment sample, we have two structures called cubic-like and monoclinic-like. The relative percentage of the two phase changes with the temperature and time.

sample	**element**	**position**	**phase**	**stoichiometry**	**cubic** like
1 h. 400 °C	Zr $3d_{5/2}$ O1s	183.52 530.89	cubic like	2.00	80%
	Zr $3d_{5/2}$ O1s	182.67 532.21	monoclinic like	2.00	
3 h. 400 °C	Zr $3d_{5/2}$ O1s	183.26 530.56	cubic like	2.00	58%
	Zr $3d_{5/2}$ O1s	182.62 531.14	monoclinic like	2.00	
4 h. 400 °C	Zr $3d_{5/2}$ O1s	183.37 530.45	cubic like	2.00	46%
	Zr $3d_{5/2}$ O1s	182.73 531.06	monoclinic like	2.00	

Table 7.4: XPS peak position in the function of the time in reaching 400 °C

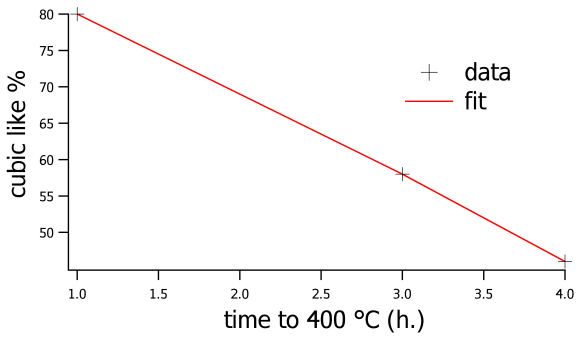

Figure 7.7: XPS relative percentage of the cubic-like phase reaching 400 °C at different times

Chapter 8

Zirconia X-ray Powder Diffraction Results

As previously mentioned, the only work that presents a characterization of nanostructured Zirconia made by SCBD is [30].

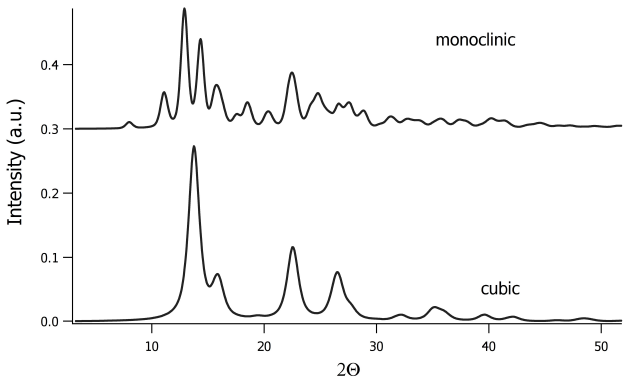

Figure 8.1: Example of XRPD spectra for pure cubic and monoclinic zirconia

In particular, using XRPD they found that the percentage of cubic and monoclinic phase after thermal treatments change if the sampled was annealed in

air or in vacuum. In this case, I want to see if changing the time in thermal treatments results in the percentage of the different phases change changing as explained in detail in Chapter 4.
The spectra of a pure cubic and pure monoclinic zirconia are very different as shown in Fig.8.1. Moreover, with XRPD we can have obtain information about crystal parameters and nanocrystal size.

We conducted two series of experiments. One at the synchrotron X-ray diffraction beam line (ID09A beamline) at ESRF synchrotron radiation facility (Grenoble, France) and the second at the Earth Science department of Universit'a degli Studi di Milano. The first series as performed on the as received materials and laboratory annealed samples. The standard beamline setup for transmission geometry with area detector was used [84], with monochromatic radiation at high energy (E =30keV; λ =0.4139Å) to minimize absorption. Raw data (pixel vs. intensity) extracted with Fit2D software[84] are converted into an angle/intensity histogram by a preliminary calibration performed with the NIST standard Si powder. Rietveld analysis of the converted spectra was performed with GSAS software [85]. The second series has been made using a four circle diffractometer equipped with CCD detector and Mo X-ray source ($\lambda = 0.710\AA$). The samples were contained in glass capillaries and the diffractions were collected in transmission geometry. The sample to detector distances was 80 mm and the integration of raw 2D data was done with the Crysalis RED software.
The as received sample is a pure cubic phase, as shown in Fig. 8.2 composed by nanocrystals with an average size of 4.45 nm, and an average molecular unit volume of 33.98Å^3, as reported in Tab.8.1.

Sample	cubic phase	m.u. volume (Å^3)	nanocrystal size (nm)	average stoichiometry (XPS)
as received	100%	33.98	4.45	1.60
30m 110 °C 1h	100%	34.13	4.62	1.90
30m 110 °C 12h	100%	33.96	4.83	1.98

Sample	cubic phase	m.u. volume (Å^3)	nanocrystal size (nm)	average stoichiometry (XPS)
30m 110 °C 24h	100%	33.94	5.22	2.00
4h 800 °C 6h	0%	(35.30)	(13.12)	2.00

Table 8.1: XRPD molecular units (m.u.) volume and nanocrystal size of cubic phase for as deposited, samples treated at 110 °C and at 800 °C. Numbers in bracket are the correspondent quantity for the monoclinic phase

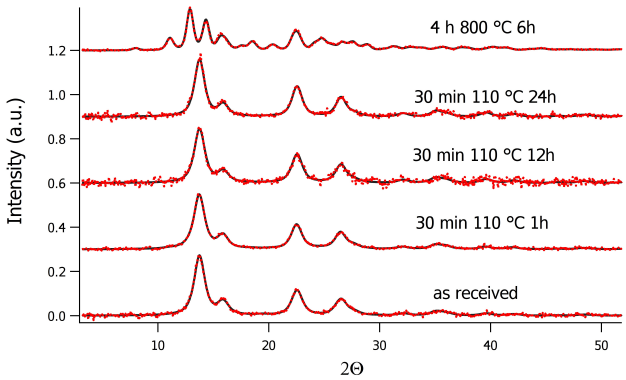

Figure 8.2: XRPD spectra of sample treated at 110 °C and 800 °C

For the samples heated at 110 °C in 30 minutes and kept to this temperature for different intervals of time we see a pure cubic phase as shown in Fig. 8.2. From Table 8.1, we can see that increasing the time in which we kept the material at 110 °C we do not have a phase evolution. So up to the temperature of 110 °C the cubic phase is stable.
Considering the nanocrystal size increasing the time in which I kept the samples at 110 °C there is a little increasing of the size as shown in black square markers

in Fig 8.3a, and for sample kept at 110 °C for 24 hours the size is of 5.22 nm. In these thermal treatments, we can have an oxidative process that causes a lattice expansion as I will show in the next Chapter 9 from simulation and a nanocrystal growth process. Moreover the molecular unit (m.u.) volume decreasing as shown with the same signature in Fig. 8.3b. This effect for which there is a lattice expansion due to size reduction, in metal oxides has been commonly explained in terms of the confinement effect, reduced ionic valencies, electrostatic relaxation and interactions among the surface dipoles [86, 87].
In Fig. 8.2, it is also reported that XRPD of the sample was heated in 4 hours to 800 °C and kept for 6 hours at the target temperature. In this case, the sample has a pure monoclinic phase. For the sample treated at 800 °C, the nanocrystals have an average size of 13.12 nm while the average volume for molecular units is of 35.30 nm.

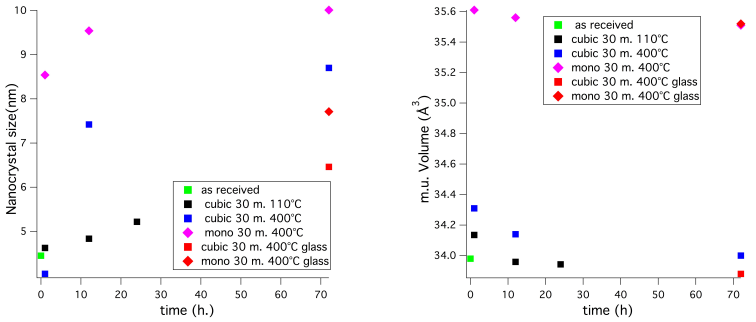

(a) (b)

Figure 8.3: XRPD size of nanograins (a) and molecular units volume (b) as a function of time for the sample treated at 110 °C, in black square markets, 400 °C in cubic phase, blue square markets, and monoclinic phase, magenta diamond markets.

For the samples heated to 400 °C in 30 minutes and kept to the target temperature for different intervals of time, we have a decreasing of the cubic phase and an increasing of the monoclinic phase increasing the time interval at 400 °C as reported in Table 8.2 and in Fig.8.4a with square blue markers. Also in

this case for a longer time at 400 °C the nanocrystal size increased while the molecular units volume decreased for cubic, in square blue markers, and monoclinic phase, in the diamond magenta markets in Fig. 8.3a and Fig.8.3b. In the last line of Table 8.2, there are the data for a sample brought to 400 °C in 30 minutes and kept at this temperature for 72 hours on a glass substrate instead of crystal silicon is shown. From the results, we can see that the phase percentage, nanocrystal size and molecular units volume are different from the same treatment but on different substrate. This confirms the crucial role of the surface energy played in phase transformation underlined emphasized in [56]. In this specific case the nanocrystal are smaller on amorphous silica than on silicon wafer for both phases as shown in Fig 8.3a. The relative percentage of cubic phase is greater on amorphous silica than on silicon wafer. These data can be explained as ba better mobility on silicon wafer that favorite favor the growth of nanograins that and can easily reach the critical size necessary to for the transition phase from cubic to monoclinic.

Sample	cubic phase	m.u. volume (Å^3)	nanocrystal size (nm)	average stoichiometry (XPS)
30m 400 °C 1h	30% (60%)	34.31 (35.61)	4.04 (8.54)	1.75
30m 400 °C 12h	21% (69%)	34.14 (35.56)	7.42 (9.54)	2.00
30m 400 °C 72h	9% (81%)	34 (35.51)	8.7 (10.01)	2.00
30m 400 °C 72h amorphous substrate	36% (64%)	33 (35.52)	6.46 (7.71)	

Table 8.2: XRPD molecular units (m.u.) volume and nanocrystal size of cubic phase for samples treated at 400 °C. The numbers in brackets are the corresponding quantities for the monoclinic phase.

Sample	cubic phase	m.u. volume (Å^3)	nanocrystal size (nm)	average stoichiometry (XPS)
4 h 400 °C capillary	100%	33.75 ()	6.36 ()	
4 h 400 °C silicon	13% (87%)	34.13 (35.34)	6.57 (8.35)	2

Table 8.3: XRPD molecular units (m.u.) volume and nanocrystal size of cubic phase for as deposited and samples treated at 400 °C. The numbers in brackets are the correspondent corresponding quantity quantities for the monoclinic phase.

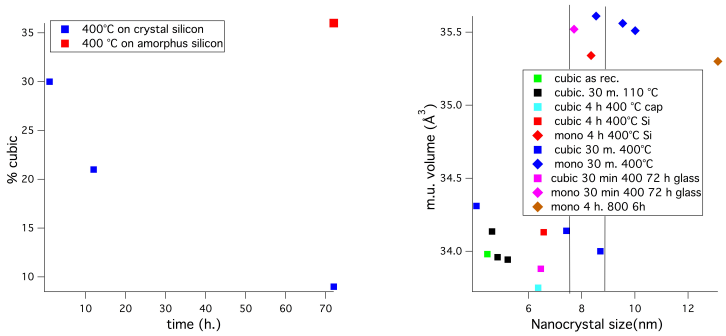

(a) (b)

Figure 8.4: XRPD cubic phase percentage as a function of time for sample treated at 400 °C on crystal silicon, black markets, and on amorphous silicon, green markets(a). XRPD molecular units volume (Å^3) as a function of nanocrystal size (nm). In square are reported the data for the cubic phase in diamond for the monoclinic phase. The two vertical lines delimited the range for the critical size (b).

I have also heated at 400 °C in 4 hours a powder in a closed quartz capillary to a limited oxygen reaction, and I have made the same treatment on a crystal

silicon wafer expose to atmospheric air. From the XRPD results, it can be seen that in capillary the sample remains cubic as shown in Fig. 8.5. This confirms the importance of the role of the oxygen vacancies in phase transition in nanomaterials.
In Fig. 8.4b, the molecular units volume ($Å^3$)in the function of nanocrystal size (nm) is reported. We can see that in the range of [7.71,8.7] nm there are cubic and monoclinic crystals. Therefore, the critical size in which we have the phase transformation is in this range. Moreover, if I considered only the material on the crystal silicon surface, the range for the critical size became [8.84,8.7] nm. Therefore, on amorphous silicon substrate, the critical size is probably lower than on the crystal silicon surface.
Summarizing the data from XRPD analysis, the received material is cubic and remains cubic at least until 100 °C. After treatment at 400 °C in atmosphere, the material is partially cubic and partially monoclinic and the relative percentage of these two phases depends on the time in which the materials were kept at 400 °C. The relative percentage of cubic phase depends on the substrate and on the environment. In a poor oxygen environment at 400 °C the sample remains cubic. At 800 °C in atmosphere the sample is pure monoclinic. Moreover, the substrate influences the phase percentage, size of the nanocrystal and the molecular unit volume.

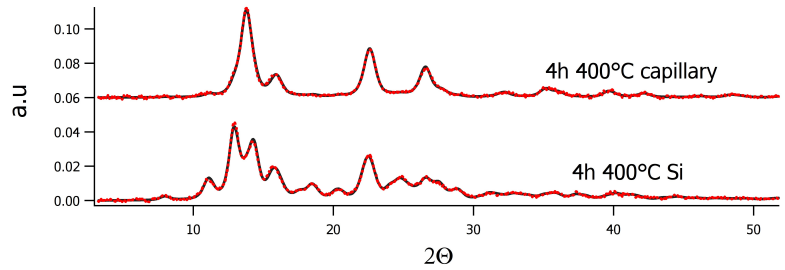

Figure 8.5: XRPD spectra of sample treated to 400 °C on silicon substrate and in a closed capillary

Chapter 9

Zirconia Simulation Results

9.1 Technical Details

I have studied the bulk behavior of zirconia in the presence of vacancies in a monoclinic and tetragonal crystal structure. I perform simulations with ultrasoft pseudopotential in the generalized gradient approximation (GGA) with the Perdew-Burke-Ernzerhof (PBE) functionals[88], for the exchange correlation potential,[88–90] in the plane-wave scheme, as implemented in the Quantum ESPRESSO (QE) package [91].
In Fig. 9.1a and 9.1b the unit cell for bulk zirconia (in gray Zr atoms and in red oxygen atoms) in the monoclinic and tetragonal phase, respectively, which are composed of 4 molecular units of ZrO_2, are reported. In order to introduce some vacancies I had to consider a Supercell (SC). In particular the SCs considered in this work are obtained by repeating two times the bulk cell in each direction giving 32 molecular units, i.e. a total of 96 atoms per SC without oxygen vacancies, reported in Fig.9.2a and 9.2b for the monoclinic and tetragonal phase, respectively. The SC was relaxed in all axes and angle parameters. In stoichiometric SC, i.e. a SC composed by ZrO_2 I have 64 oxygen atoms. For simulating a substoichiometric material, I have removed some oxygen atoms. In particular for a stoichiometry of 1.60, 1.66, 1.78, 1.84 and 1.94 I have considered 51, 53, 57, 59 and 62 oxygen atoms respectively. Starting from the full oxides SC, we can organize the atoms in the shells of symmetry-equivalent sites [92]. Each shell is filled with the same kind of ions. Oxygen vacancies are introduced removing all the oxygen atoms from one or more shells according to the stoichiometry that we want simulate. Also in this case, the relaxation was performed on all SC

parameters, i.e. axes and angles. In Fig. 9.3 a tetragonal SC with stoichiometry of 1.66, before the relaxation, is reported and the black ball represented the oxygen that was removed.

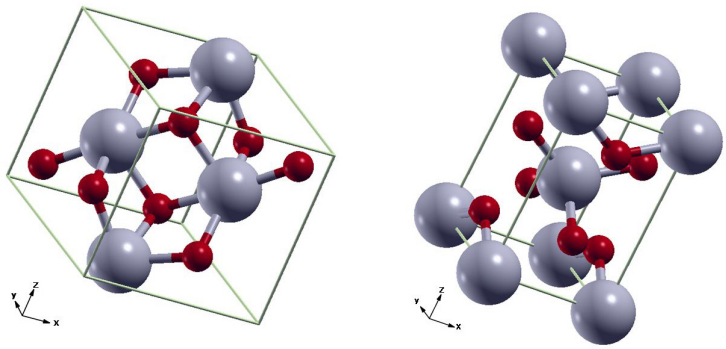

(a) (b)

Figure 9.1: (a) monoclinic and (b) tetragonal zirconia bulk cell, in gray zirconium atoms, in red oxygen atoms.

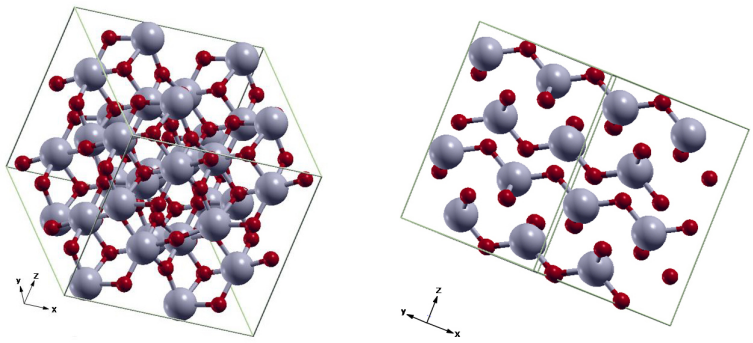

(a) (b)

Figure 9.2: (a) monoclinic and (b) tetragonal zirconia Supercell, in gray zirconium atoms, in red oxygen atoms.

Ground-state calculations are performed with a kinetic energy cutoff of 35 Ry

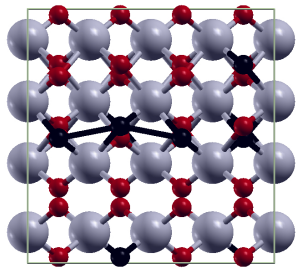

Figure 9.3: tetragonal zirconia Supercell with stoichiometry of 1.66, in gray zirconium atoms, in red oxygen atoms, in black oxygen removed.

(480 eV) for the plane wave functions, and a Monkhorst-Pack [93] grid $4 \times 4 \times 3$ for tetragonal and $4 \times 4 \times 4$ for monoclinic respectively for the Brillouin zone (BZ), thus maintaining an (approximately) uniform mesh in the BZ.

9.2 Results

For the tetragonal zirconia I have considered four different vacancy concentrations corresponding to a stoichiometry of 1.60, 1.66, 1.78, 1.84 and 1.94 each one with three different distributions while for monoclinic zirconia I have considered only one distribution for each different stoichiometry.
From Fig 9.4 I can see that the molecular unit volume of the tetragonal phase is between 33 and 34.5 $Å^3$, while for the monoclinic phase it is between 34.5 and 36 $Å^3$. For both the tetragonal and monoclinic phase the molecular unit volume increased with stoichiometry with a linear behavior, as expected, because in general vacancies have negative formation volumes. For experimental data I have considered a weight average stoichiometry obtained from XPS data and the molecular units volume obtained from the XRPD data. I can see that, as in simulation, the monoclinic phase has a bigger molecular unit volume then the tetragonal/cubic phase. For material with a stoichiometry of 2 the experimental molecular unit volume is lower than the simulated one. This can be due to the fact that nanomaterial suffers of a lattice contraction due to size nanocrystal expansion, while the simulated data are for bulk zirconia. Instead for substoichiometric zirconia the measured molecular unit volume is bigger than the simulated one. This can explained considering the fact that we have two

competitive phenomena in nanocrystal: oxidation that give a lattice expansion and nanocrystal growth that give a lattice contraction.

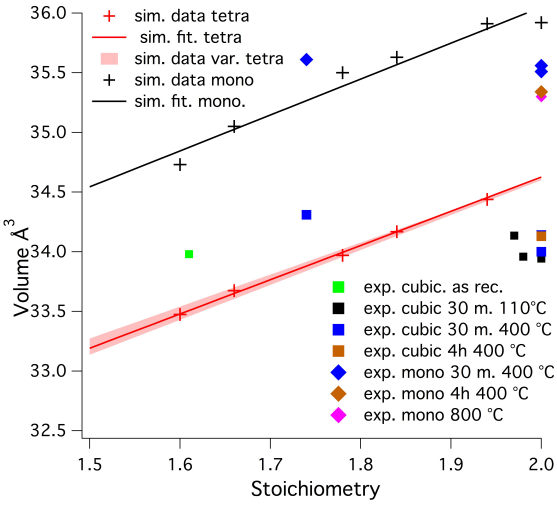

Figure 9.4: tetragonal and monoclinic molecular unit volume as function of the stoichiometry for simulated data (sim.) and experimental data (exp.) with time and temperature of annealing

The formation energy ΔE_f of oxygen vacancies can be estimate according the formula

$$\Delta E_f = E(N_{Zr}, N_O) - N_{Zr}\mu_{Zr}^{ZrO_2} - N_O\mu_O^{ZrO_2} \tag{9.1}$$

where $E(N_{Zr}, N_O)$ is the total energy of a system containing N_{Zr} and N_O zirconium and oxygen atoms in the system with vacancies, while $\mu_{Zr}^{ZrO_2}$ and $\mu_O^{ZrO_2}$ are the chemical potential of zirconium and of oxygen, respectively, in ZrO_2. In order to prevent the formation of pure oxygen I consider the chemical potential for the formation of molecular oxygen O_2 for each atoms $\mu_O^{O_2} = -31.75825871$ Ry and imposing that the chemical potential of oxygen in zirconia $\mu_O^{ZrO_2}$ must be lower

$$\mu_O^{ZrO_2} < \mu_O^{O_2} \tag{9.2}$$

In the same way I exclude the formation of metallic zirconium that has a chemical potential $\mu_{Zr}^{Zr} = -99,15301121$ Ry imposing

$$\mu_{Zr}^{ZrO_2} < \mu_{Zr}^{Zr}. \tag{9.3}$$

From the relation 9.2 I have the superior extrema for $\mu_O^{ZrO_2}$. The inferior extrema can be calculated considering the monoclinic phase formation energy equal to zero with $\mu_{Zr}^{ZrO_2} = \mu_{Zr}^{Zr}$. The range obtained in this way for $\mu_O^{ZrO_2}$ is $[-32.14; -31.76]$ Ry. The lower extrema of this range correspond to O poor (or Zr rich) grow conditions, the higher extrema to O rich (or Zr poor) grow conditions. In our case in the deposition chamber we have a pressure of 10^{-5} mbar that in the deposition process can grow to 10^{-3} mbar due to the presences of Argon. So we do not have oxygen in the grow process and the contribution due to the pressure dependence of O_2 gas is neglected in our simulation. I can rearrange the formula 9.1 and specify it for the considered SC. In this way the formation energy for molecular units is

$$\Delta E_f = E(N_{Zr}, N_O) - E_M + \mu_O^{ZrO_2} \frac{(2N_{cell} - N_O)}{N_{cell}} \tag{9.4}$$

where $E(N_{Zr}, N_O)$ is the molecular units energy of the substoichiometry SC, E_M is the molecular unit energy of the stoichiometry monoclinic cell, N_{cell} is the number of unitary cell in the SC that in our case is 32 and N_O is the number of oxygen in the SC that is different for the different stoichiometry. In Fig.9.5 the formation energy for different value of the oxygen chemical potential $\mu_O^{ZrO_2}$ are plotted. In the legend with t. and m., the monoclinic and tetragonal phase that are plotted in continuous and dashed lines, respectively, with a different color for the different stoichiometry are indicated. Moreover, for the tetragonal phase, for which I have considered a different distribution of the vacancies, I have also plotted the variance indicated with, t. var. in legend. I can see that the monoclinic phase full oxide, i.e. a stoichiometry of 2, draw with black dashed line, has the lowest formation energy and so is the stable phase. Line of the same color, which have the same stoichiometry, are parallel and the dashed line has a lower energy of the continuous one of the same color. This means that, for fixed stoichiometry, the monoclinic phase is preferred to the tetragonal one. The distance between the pair of dashed and continuous lines of the same color decrease with increasing the stoichiometry. This means that for poor oxygen zirconia, i.e. substoichiometric zirconia ZrO_{2-x} the differences in formation energy between the monoclinic and tetragonal phase is lower than a zirconia ZrO_{2-y} with more oxygen, $x < y$. For oxygen chemical potential greater than -31.97 Ry, the substoichiometry formation energy are always greater than the monoclinic and tetragonal full oxide phase, in fact all the colored lines are above the two black lines. For oxygen chemical potential lower than -31.97 Ry the monoclinic phase with a stoichiometry of 1.94 is preferred over the tetragonal full oxide phase. While for $\mu_O^{ZrO_2} < -32.08$ Ry also the 1.94 tetragonal phase is preferred

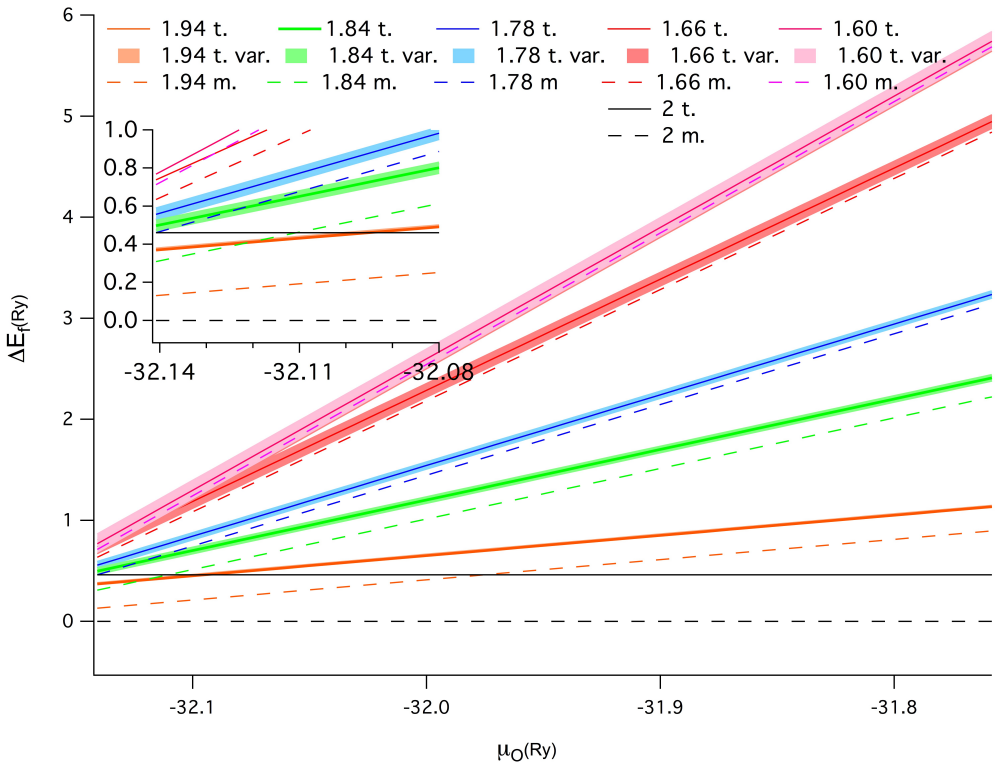

Figure 9.5: Formation energy for the different stoichiometry as function of the oxygen chemical potential. t. stay for tetragonal reported in continuous lines, m. stray for monoclinic phase, reported in dashed lines, var. stay for variance. The same color was used for the same stoichiometry.

over the tetragonal full oxide situation as shown in the inset of Fig.9.5. For $\mu_O^{ZrO_2} < -32.12$ Ry the 1.84 monoclinic phase is preferred over the 1.94 tetragonal and of the full oxide tetragonal. Moreover, for the $\mu_O^{ZrO_2} < -32.13$ Ry monoclinic phase with a stoichiometry of 1.60 is preferred over the tetragonal one with a stoichiometry of 1.66. All of this change for low value of oxygen chemical potential, i.e. zirconia poor in oxygen, indicated that the phase stability can change with the concentration of oxygen vacancies.

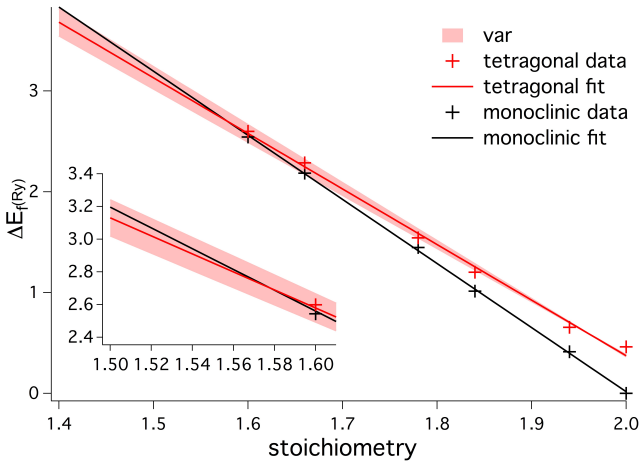

Figure 9.6: Formation energy as function of stoichiometry for $\mu_0^{ZrO_2} = -32$ Ry

In Fig. 9.6 the formation energy as function of the stoichiometry with a fixed value of $\mu_0^{ZrO_2} = -32$ Ry is reported. Black marks denoted the simulated data form monoclinic phase and red marks denoted the data for tetragonal phase. With the black and red lines the fits for monoclinic and tetragonal, respectively, are reported. While the colored area is the variance for the tetragonal simulated data. We can see the linear behavior of the formation energy as function of the stoichiometry for both the monoclinic and tetragonal phase. From the inset in Fig. 9.6 we can notice that for a stoichiometry of 1.58 the tetragonal and monoclinic phases have the same formation energy while for a lower value the tetragonal phase has a lower formation energy than the monoclinic one. This means that, also in bulk material, from this result, the tetragonal phase can be stable for stoichiometry lower than 1.58. From variance, we can estimate

an error for the order 0.1 in the estimation of the critical stoichiometry below which the tetragonal phase is stable.
The simulation results showed until now concern bulk zirconia. I will study the stability of the ZrO_{2-x} films combining these bulk data with *ab-initio* estimation of surface energy according to the receipt presented in Ref.[67]. In particular, Debernardi et al. considered the surface energy of (100) of the monoclinic and of (001) of the tetragonal phase repeating along the growing direction 4 and 5 unit cells of monoclinic and tetragonal structure, respectively. This gives a total of 8 (48) and 10 (30) ZrO_2 monolayers (atoms). The surfaces are O terminated and keep their stoichiometry. The crystal axes parallel to the surface are kept fixed to bulk theoretical value of pure ZrO_2, while along the growth direction the atomic coordinates are relaxed. We can call this structure slab (SL). The surface energy (per molecular unit) is the increasing of the energy due to the formation of a surface with respect to the bulk phase,

$$E^s = E^{tot}_{SL} - NE^{TOT}_{bulk} \tag{9.5}$$

and normalizing by the appropriate number of the molecular units of the surface. In formula 9.5 E^{tot}_{SL} is the total energy of the SC obtained by repeating N times the bulk unit cell along the grow direction and E^{TOT}_{bulk} is the total energy of the bulk unit cell. In this way they have $E^s_{tet} = 15.79$ Ry and $E^s_{mono} = 19.93$ Ry for the molecular unit, where E^s is the energy of two surfaces in the slab geometry. Considering the energy formation difference between the monoclinic and tetragonal phase as a function of stoichiometric $\Delta E(x)$ taken from the fit in Fig.9.6 at $\mu_O^{ZrO_2} = -32$ Ry, the critical length l_{crit} , i.e., the maximum thickness of the film at which the tetragonal phase has lower energy with respect to the monoclinic phase, is estimated, for a mono-crystalline (M) film, as

$$l^M_{crit} = l_{ML}\frac{E^s_{tet} - E^s_{mono}}{\Delta E(x)} \tag{9.6}$$

where l_{ML} is the thickness of one monolayer of ZrO_2, $l_{ML} = 2.63\mathring{A}$ Ref. [67].

In fig.9.7 the critical thickness for a film, red line, is reported. In the area above the fitted line the monoclinic phase is preferred while under the fitted line the tetragonal one is the preferred. Note, that our estimation made in Eq. 9.6 assumes the film to be uniform and with a specific growth orientation. A more accurate evaluation that improves the approximation mentioned above and that includes the vibrational contributions as a function of temperature is needed to account. [67]

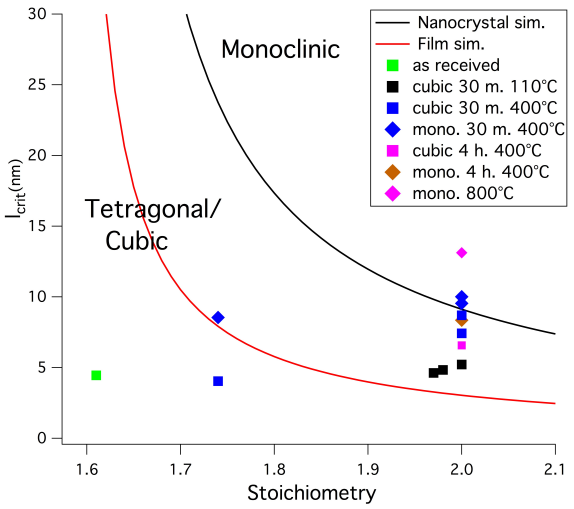

Figure 9.7: Simulated critical size for a film, red line, and for a nanocrystal, black line. For the experimental data I have considered a weight average stoichiometry obtained from the XPS data and the molecular units volume obtained from the XRPD data reported in marks.

We can extend this model to a cubic nanocrystal by multiplying the equation 9.6 for a factor of 3. In this way we can have a rough estimation of the critical size for a nanocrystal with oxygen vacancies. In this model, we have assumed a cubic form of nanocrystal and that the surface energy does not depend on the surface orientation. The critical size for a nanocrystal is reported with the black line in Fig. 9.7. For the experimental data, I have considered a weight average stoichiometry obtained from the XPS data and the molecular units volume obtained from the XRPD data. We can see that the square marks, cubic phase, are all under the black line, in the area in which also from simulation, the stable phase is the tetragonal/cubic. Only one data has a great difference from simulation, the blue diamond at approx. 1.75 of stoichiometric. This discrepancy can be due to the fact that I have considered an average stoichiometric, this excludes the possibility of a coexistence of a different stoichiometric for a different phase. However, if I considered this eventuality according to the XPS results, in which the monoclinic like phase was always stoichiometric, this data will be shifted at a higher stoichiometric while, the cubic data, represented with a square market, will be shifted at lower stoichiometric in the area in which the tetragonal/cubic phase is the stable one. Therefore all the data will become compatible with the simulation. Another possible explanation can be from the observation that all the squares (cubic/tetragonal phase) are below the black line denoting the stabilization of tetragonal phase nanocrystals. All the diamonds (monoclinic phase) are above the red line denoting the stabilization of the tetragonal phase film. The experimental samples have a structure that can be considered intermediate between the uniform film and the nanocrystal, so that the theoretical predictions are in agreement with all the experimental data without needing to correct the experimental data stoichiometry according the consideration made above.
So the main results in this part are:

- molecular unit volume increases linearly with stoichiometry, both from the tetragonal and monoclinic phase
- tetragonal bulk zirconia becomes stable for a stoichiometric value lower than 1.58
- we have predicted a critical film thickness and nanograin size as a function of stoichiometry, and our theoretical results are compatible with our set of experimental data according to the above discussion.

Chapter 10

Zirconia Results Overview

The aim of this part of the study was to determine the stability or evolution of zirconia nanostructured thin film in thermal treatments. Two different kinds of characterization, namely XPS and XRPD, were used. Moreover, we also used DFT simulation. The XPS gives surface information and is sensitive to the local electronic environment [71], while XRPD gives information about the whole material and is sensitive to the long range order. These experimental data were also compared with the simulation data, finding a good agreement in spite of the the approximation used in the theoretical model.
From the XPS and XRPD, the received samples produced by SCBD have a stoichiometry of 1.61 and are in the cubic phase stable at room temperature.
The samples treated at 110 °C reached in 30 minutes and kept at this temperature for different intervals of time remain cubic from XRPD data. Moreover, we have a small amount of nanocrystal growth from 4.22 nm of the received material to 5.22 nm for the sample kept at 110 °C for 24 hours. The XPS results show an oxidative process until the complete oxidation was reached, after 12 hours, with a local electronic evolution from cubic-like to monoclinic-like peak.
The samples heated at 400 °C in 30 minutes and kept at this temperature for different intervals of time, show, from XRPD data, an evolution of relative percentages of cubic and monoclinic phase. Whereas, from XPS data, an evolution is observed until 12 hours at 400 °C, after the surface structure remains stable.
The characteristics of the samples also depend on the time implied to reach the target temperature, as shown by the difference in stoichiometry and local electronic environment among samples heated at 400 °C in 30 minutes, 1 hour, 3 and 4 hours.

The phase transition from cubic to monoclinic is influenced by the presence of oxygen as shown from the XRPD of a powder heated at 400 °C for 72 hours in a closed quartz capillary. The zirconia remains cubic, while with the same thermal treatment made in air it becomes almost monoclinic. Moreover, the material of the substrate influences the thermal evolution of the nanostructured zirconia. From nanocrystal size, molecular unit volume and phase we can estimate a range of the nanocrystal critical radius for phase transition. In the case of crystal on silicon substrate is in the range of [8.84,8.70]nm.
Our simulations of bulk zirconia predict that the molecular unit volume increases linearly with stoichiometry, both from the tetragonal and monoclinic phases. The value of the volume is compatible with the experimental one with an error of 1 nm. The experimental data do not have the same linear behavior due to lattice contraction due to size nanocrystal expansion. Moreover, according to our first principles calculations, the tetragonal bulk zirconia becomes stable for stoichiometric value less than 1.58. With an approximative model, we have predicted a critical nanograin size in the function of stoichiometry with good agreement with XRPD data.
In order to improve our understanding of this material and thereby the engineering of the material for different applications it is possible to use other experimental techniques. Nevertheless, thermal treatments induced different physical phenomena: oxidation, nanocrystal growth, and phase transitions. These phenomena depend on surface energy, which is influenced by different factors: aggregation of nanocrystals, change in the surrounding atmosphere, hydrostatic pressure, internal hydrostatic pressure, presence of anions, and oxygen vacancies [56]. The coexistence of these phenomena complicates the interpretation of the experimental data. According to my experience, there are two main approaches to study this material. The first one, in the case in which we are focusing on specific applications, is make directly a prototype and see if is working. In fact the zirconia evolution under thermal treatments depends on a chemical environment, so in the case of DRM and SOFC, in which we have the contact of zirconia with a different chemical, I cannot predict with certainty how zirconia can react. The second one, if we are interested more in fundamental physics and go deeper in a full understanding of this material is the ability to turn on and off the different physical phenomena to understand how each phenomenon influences the propriety of the nanostructured zirconia. In this way, simulations are a very good tool, as already demonstrated in this thesis. Nevertheless, this study can give some preliminary information about the behavior of these materials that can help to understand if nanostructured zirconia thin film made by SCBD can be suitable in different applications.

Chapter 11

Perovskitic

As mentioned in Chapter1, the Kyoto protocol commits the signers to the reduction of CO_2. Furthermore there are annual international conferences about global warming and a constant key topic is the necessity of reducing CO_2 emissions. There are different sources of CO_2 emissions and electric power generation is the greatest one from a global point of view. Carbon capture and storage (CCS) is an approach to relieving global warming by capturing CO_2 and storing it instead of releasing it into the atmosphere [14–17]. In oxyfuel power plants, the fossil fuel is combusted using pure oxygen and the result is a gas stream with almost pure CO_2 (90-95%) in the dried flue gas. The CO_2 can then be captured more easily than when air is used in the combustion process and stored in a safe geological site [18, 94].
Moreover oxygen is ranked among the top five in the production of commodity chemicals in the world [95]. The separation of oxygen from air is big business, where nearly 100 million tons of oxygen are produced every year[19]. Oxyfuel combustion process and oxygen-blown gasification can be used to convert coal and natural gas into an intermediate synthesis gas that can be further processed to produce electricity, chemicals and transportation fuels [19]. There have been two fundamental approaches to air separation, which are cryogenic and non-cryogenic distillation. The cryogenic distillation is typically reserved for applications that require tonnage quantity of oxygen at ultra-low temperatures. The latter involves the separation of air at ambient temperatures using either molecular sieve adsorbents via pressure swing adsorption (PSA), or membrane separation process using the polymeric membranes[19]. Recently, a third category of air separation has emerged, which is based on specialized ce-

ramic membranes that separate oxygen from air at elevated temperatures, in contrast to the super-cooled temperatures required by conventional cryogenic distillation. This technique is based on dense ceramic membranes, which carries out the separation of oxygen from air at elevated temperatures, typically 800 to 900 °C in order to activate the oxygen diffusion process through the membrane [19]. In producing high purity oxygen, dense ceramic membranes can also be integrated in catalytic membrane reactors for carrying out different petrochemistry processes such as oxidative coupling of methane to ethylene and ethane($2CH_4 + O_2 \rightarrow C_2H_4 + 2H_2O$), partial oxidation of methane to syngas, partial oxidation of heptane to hydrogen, selective oxidation of ethane to ethylene, and selective oxidation of propane to propylene [96–101], during which both separation and catalytic processes are achieved in a single step. The mixed conducting membrane technology is also commercially prospective for an air separation unit integrated with a hot turbine system [102]. Another interesting example of the coupling between oxygen separation and catalysis is the ammonia oxidation into nitric acid manufacturing process [103].
The two main types of oxygen separation systems based on ceramic membranes are: pure oxygen conducting membranes and mixed ionic-electronic conducting membranes. A driving force has to be provided for oxygen to permeate through the membrane. This driving force can be either an electrical potential gradient or a chemical potential gradient (i.e. gas component partial pressure). As oxygen is transported in the ionic form, and to fulfill the electric neutrality criteria, there must be a simultaneous flux of electrons in the opposite direction to charge compensate the oxygen flux [103]. In certain materials that provide only ionic conductivity, electrodes are provided for the electron pathway. A benefit inherent in such a system is the control over the amount of oxygen generated via the application of an electric current. A mixed ionic-electronic membrane (MIEC), in contrast, requires no electrodes to operate, although it needs the oxygen pressure difference on both sides of the membrane.

As shown in Figure 11.1, the electronic conductivity is presented as a small internal circuit involving oxygen partial pressure gradient. The O_2 permeates from the high oxygen partial pressure side to the low oxygen partial pressure side, while the overall charge neutrality is maintained by opposite movement of electron flow. So mixed ionic-electronic conducting (MIEC) membranes are promising alternatives for oxyfuel power plants due to their high selectivity for oxygen separation and their significantly lowest efficiency losses compared with currently existing cryogenic distillation technology for oxygen separation [104]. The MIEC family is rich in structures and the perovskite structure is within them. The perovskite structure, at the presence of oxygen vacancy, exhibits

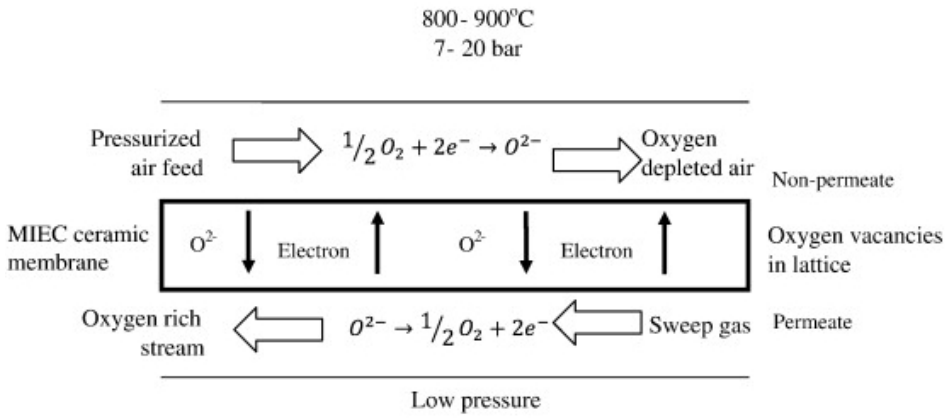

Figure 11.1: Schematic representation of O_2 transport in dense ceramic MIEC membranes [19]

good ionic and electronic conductivity leading to attractive oxygen flux [102]. In the last decade, intensive research has been dedicated to the preparation and characterization of MIEC membranes [14–18, 102, 104–113].

Perovskite oxides are an extremely interesting class of materials. The ideal perovskite has the compositional formula $A^{2+}B^{4+}O_3$ ($A^{1+}B^{5+}O_3$ or $A^{3+}B^{3+}O_3$ are also possible) [102]. Its general crystal structure has medium size cations B which are located at the corner and the larger cations A is located to the center of the cube (Fig. 11.2a) while the oxygen atoms are placed in the center of the cube edges leading the formation of BO_6 octahedral extended three dimensionally (Fig. 11.2b).

The relative sizes of the A and B ions dictate the shape of the crystal structure. The perovskite structure is preserved if the tolerance factor, t, as given in Eq. 11.1, is between 0.8 and 1 as stated by Goldschmidt [114]

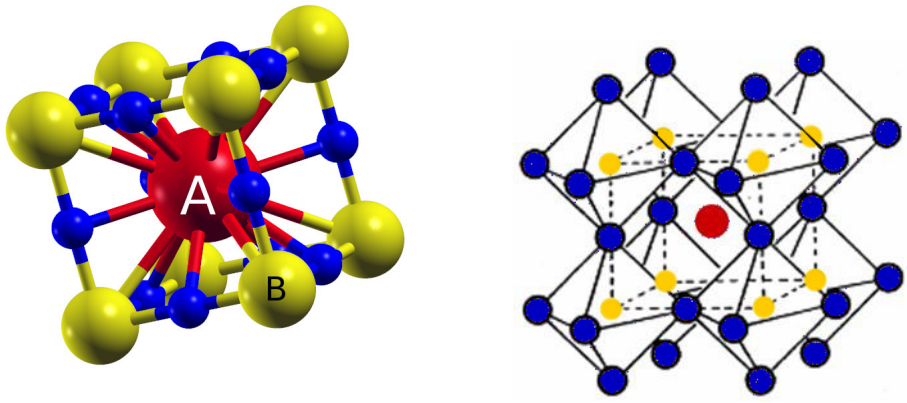

(a) (b)

Figure 11.2: Crystal structure of a general perovskite ABO_3

$$t = \frac{R_A + R_O}{\sqrt{2}(R_B + R_O)}, \tag{11.1}$$

where R_A, R_B and R_O are the radius of A-site, B-site and oxygen ions, respectively. Perovskite has the capability to simultaneously accommodate a number of different cations in its lattice with the constraints that ions of one, two, three, four and five valence will be accommodated in varying combinations if their sizes are in the range of 0.45-0.75 or 1-1.4 a.u. (atomic units). Therefore, the perovskite crystal structure can be realized with a wide variety of different elements at the A and B positions.

This results in a class of materials with similar lattice parameters but a wide range in physical properties [115] including superconductivity [115], colossal magneto-resistance[115], ferroelectricity[115, 116], a high electronic/ionic conductivity and catalytic characteristics [115, 117, 118] promising for applications such as sensors [115] oxygen separation membranes[19], and solid oxide fuel cells (SOFCs)[117, 119], catalytic converters [120, 121].

In crystals, several types of defects can be present including zero dimensional or point defects. Those defects are generally separated into vacancies (atoms missing in the lattice), interstitial atoms (atoms on lattice sites which are not normally occupied) and substitutional atoms (lattice site that are occupied by

foreign atoms)[94]. The diffusion of oxygen ions is provided by vacancy defects present in the perovskite structure, because the ideal structure is unable of conducting those ions [122, 123]. The presence of vacancies is due to the high tolerance of perovskite materials to non-stoichiometric structures, which allows for obtaining a high ionic conduction of oxygen [19]. When the B-site of the perovskite is doped with a metal ion, B', with lower valence state, oxygen vacancies are created as well as a change in valence state of ions A occurs, in order to maintain electronic neutrality. The stability of perovskite structure oxides is also improved by doping A-site with a more stable ion, A', to produce $A_xA'_{1-x}B_yB'_{1-y}O_{3-\delta}$. It is important to note that the term δ is related to the amount of vacancies and, therefore, the higher the number of vacancies is, the higher the oxygen permeation flux will be, since the perovskite structure stability is preserved [124]. A large number of oxygen vacancies can be formed in perovskite crystals by doping ions with different valences. At high temperatures, oxygen is incorporated into perovskite crystal structure resulting in the annihilation of an oxygen vacancy and the formation of two electron holes, as expressed in Equation 11 in Kröger-Vink notation.

$$V_o^{\bullet\bullet} + \tfrac{1}{2}\,O_2 \longleftrightarrow O_o^{\times} + 2\,h^{\bullet}$$

where $V_o^{\bullet\bullet}$ is the oxygen vacancy, $O_o^{\times}$ is the lattice oxygen and $h^{\bullet}$ is the electron hole [123].

At elevated temperatures, the non-stoichiometric oxygen of perovskite-type ceramics changes with temperature and ambient oxygen partial pressure [125]. Therefor oxygen permeation flux is related not only to upstream and downstream oxygen partial pressures, but also to temperature, membrane thickness and other transport properties of the perovskite type ceramic material. With constant oxygen ion diffusivity, the oxygen permeation flux through the membrane is directly related to the oxygen nonstoichiometry of the perovskite type ceramic[126]. Oxygen transport through a MIEC, as shown in Fig. 11.3 involves three progressive steps: (i) the surface-exchange reaction on Interface I; (ii) the simultaneous bulk-diffusion of charged species and electron/electron holes in the bulk phase and (iii) the surface-exchange reaction on Interface II[127, 128]. As the membrane thickness is decreased, as reported in Fig. 11.4, the controlling step will no longer be bulk-diffusion but surface- exchange reaction [127, 129, 130].

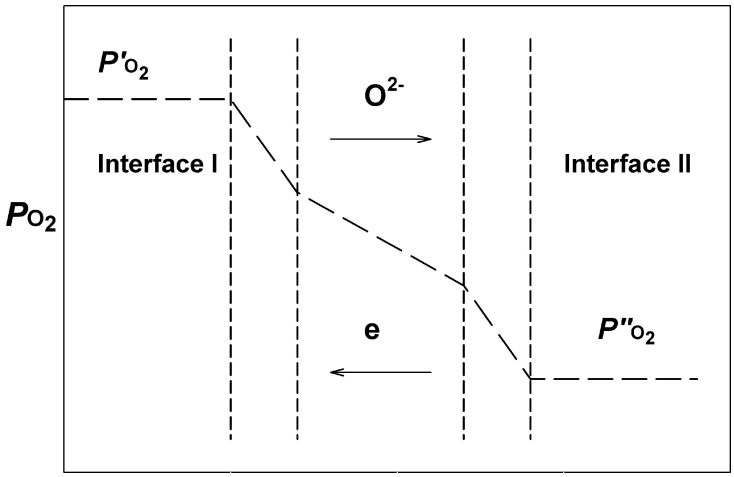

Figure 11.3: Different sections involved in oxygen transport during oxygen permeation [102]

The oxygen permeation flux based on bulk diffusion can be expressed by Wagner equation[102]

$$J_{O_2} = \frac{RT}{16F^2L} \int_{p''_{O_2}}^{p'_{O_2}} \sigma_{amb}(p_{O_2}) d \ln p_{O2} \tag{11.2}$$

where J_{O_2} is the oxygen permeation flux in mol m^{-2} s^{-1}; R is the gas constant, F is the Faraday constant, L is the membrane thickness, σ_{amb} is the ambipolar conductivity, and p'_{O_2} and p''_{O_2} are the oxygen partial pressures at the high pressure side and low pressure side, respectively. Consequently, reducing membrane thickness will lead an increasing of O_2 permeation rate. However, for thinner membranes, the resistance to oxygen ion conduction will be decreased until a certain limit, known as the characteristic thickness of the membrane L_c which also depends on the operating conditions such as temperature and O_2 partial pressure. The L_c of most MIEC membranes typically range from 20 to 3,000 μm. For a thickness under L_c, the region of higher resistance becomes the interfaces I and II that are the surfaces with exchange reactions. The Wagner equation is not applicable when the oxygen flux becomes determined by the surface reaction [94]. The materials studied in this work have a thickness of 1 mm, so they are in the diffusion-controlled range (Fig. 11.4).

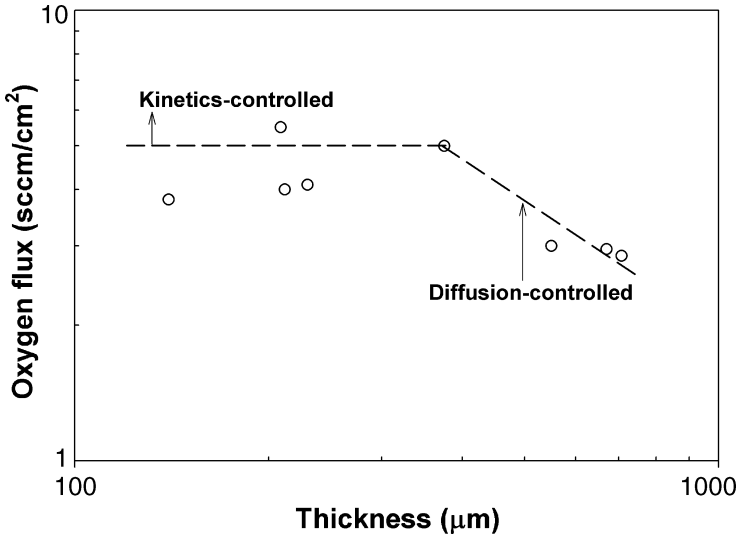

Figure 11.4: Variation of regime from bulk-diffusion to surface-exchange reaction limited with decreasing membrane thickness[131].

11.1 Data and Results

As mentioned before, in order to have oxygen permeation in perovskite the presence of oxygen vacancies is needed to induce a partial substitution of the cations B with lower valence cations, B'. In this way, some oxygen must be depleted to maintain the charge neutrality, but this substitution can give some structural instabilities that can be overcome by a partial substitution of the cations A with another A'. In this work, strontium cobalt-ferrite, Sr(Co, Fe)$O_{3-\delta}$ (SCF) around 1000 °C present oxygen permeation are considered. This material suffer of structural instability due to the formation of brownmillerite in the range temperature 700 °C-800 °C. In order to overcome this issue a partial substitution of Sr(2+) ions with lanthanum La(3+) or Barium Ba(2+) can be used [132]. Results from permeation tests [20–29] show that the best composition among these two materials are $La_{0.6}$,$Sr_{0.4}Co_{0.2}Fe_{0.8}O_{3-\delta}$ (LSCF6428) and $Ba_{0.5}$,$Sr_{0.5}Co_{0.8}Fe_{0.2}O_{3-\delta}$ (BSCF5582). In particular, these materials show an acceptable structural stability during heat/cooling between ambient and operating temperature (700 °C-950 °C).
The samples analyzed have a thickness of 1 mm and a disk diameter of 14.7

mm produced at Forschung-zentrum Jülich (FZJ) by uniaxial pressing and sintering up to 1000 °C and 1200 °C for BSCF and LSCF, respectively, as better explained in [16, 25].
In the work of Brisotto et al. presented in the article "High temperature stability of $Ba_{0.5}Sr0.5Co_{0.8}Fe_{0.2}O_{3-\delta}$ and $La_{0.6}Sr_{0.4}Co_{1-y}Fe_yO_{3-\delta}$ oxygen separation perovskite membranes" [132] we have used a multi-methodological approach to the study these two materials in a wide temperature range.

The surface morphology of the two materials was examined in a scanning electron microscope (SEM FEG MIRA 3-TESCAN) with X-ray Energy Dispersive Spectroscopy (EDS) microanalysis (Bruker Quantax 200 with XFlash detector). The chemical composition was measured by a Jeol-8000 Superprobe with six spectrometers WDS (Wavelength Dispersive Spectroscopy), using mineral standards. Structural and microstructural XRD characterization was performed by an advanced diffractometer (Bruker D8Advance) operating with Cu tube (40 kV and 40 mA). Two-dimensional XRD patterns were acquired using a Rigaku D-Max Rapid Diffractometer (Cu tube-40 kv and 30 mA), equipped with a collimator (300 μm area) and an Image Plate detector. The measurements were carried out in the reflection mode at 20°. Two synchrotron X-ray diffraction experiments were performed: the first at the ID09A beamline at ESRF synchrotron radiation facility (Grenoble, France) on as received materials (BSCF, LSCF) and laboratory annealed samples; the standard beamline setup for transmission geometry with area detector was used [84], with monochromatic radiation at high energy (E = 30 keV; λ = 0.4145Å) to minimize absorption. In the second experiment, performed at the MCX beamline of the ELETTRA synchrotron radiation facility (Trieste, Italy), the thermal expansion coefficient (TEC) and the structural evolution up to 1000 °C of both perovskites were monitored, by using monochromatic radiation (λ = 0.7866Å) and the experimental set up described in [133]. The sample is first powdered and then inserted within a quartz capillary inserted into a closed furnace (for accurate temperature control in the range 25-1000 °C) and sealed to a device able to switch from vacuum to air or inert gas (N_2) atmospheres. Diffraction signals are collected by a translating curved (cylindrical) imaging plate detector to assure a constant sample-detector distance and avoid geometrical corrections for intensity. Raw data (pixel vs. intensity) extracted with Fit2D software[84] are converted into an angle/intensity histogram by a preliminary calibration performed with the NIST standard Si powder. Rietveld analysis of converted spectra was performed with GSAS software [85].

The surface morphology of the LSCF discs is characterized by small grains (diameter 1.2 $\pm$ 0.07 μm) and closed porosity few micrometers in size, as shown

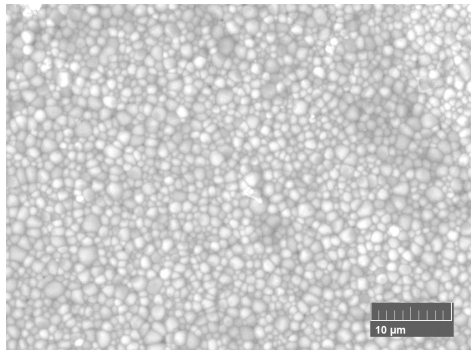

(a)

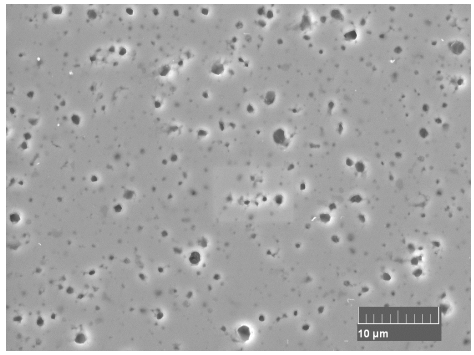

(b)

Figure 11.5: LSCF secondary electron image of (a) surface and (b) section. The grains morphology and the closed porosity can be clearly observed [132].

in Fig.11.5a and Fig.11.5b, respectively. WDS analyses confirm the nominal composition. Synchrotron XRD measurements show that at room temperature LSCF is Rhombohedral, R-3c, (a = 5.4789 Å c = 13.3215 Å) with (La, Sr), (Co, Fe) and O in the (0,0,0.25), (0,0,0) and (0,y,0) position with y = 0.4802, from structural refinement. Increasing the temperature, a modification of the crystal structure was clearly detected. In particular at about 700 °C the LSCF becomes cubic. The surface morphology of the BSCF membranes is shown in Fig.11.6a; grain and porosity size (Fig.11.6b) are about 5 μm and 1 μm, respectively. WDS measurements confirm the nominal composition. The synchrotron XRD results

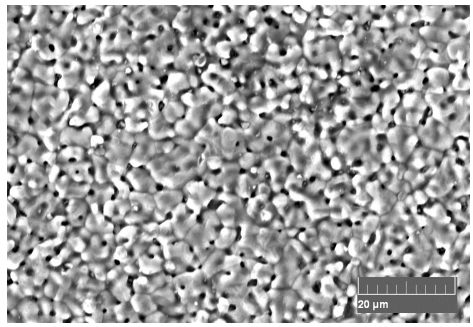

(a)

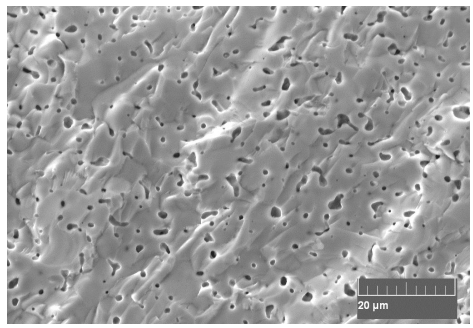

(b)

Figure 11.6: BSCF secondary electron image of (a) surface and (b) fracture surface. The grains morphology and the closed porosity can be clearly observed[132].

show the cubic structure (a = 3.9740 Å), Pm-3 m with (Ba, Sr), (Co, Fe) and O atoms in the (0,0,0), (0.5,0.5,0.5) and (0.5,0.5,0) position, respectively. Surface diffraction measurements also indicate the presence of a small amount of Co oxides. This finding is confirmed by SEM and EDS, which evidences the presence of some Co rich particles mainly at grain boundaries, see Fig.11.7. XRD analyses relieved both CoO and Co_3O_4.

The LSCF sample, heated in air, shows a structural transition from the R-3c to the Pm-3 m structure above 750 °C, detectable by the disappearance of Rhombohedral superstructure diffraction peaks in XRD spectra. The geometric transformation of the unit cell at about 700 °C is confirmed by the Rhombohe-

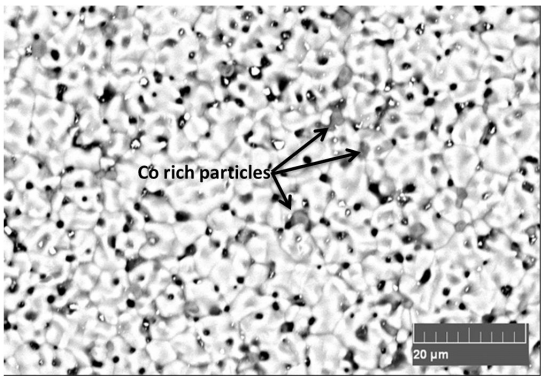

Figure 11.7: BSCF the Co rich particles dispersed on sample surface close to the grain boundaries can be seen as dark gray spots indicated by the arrows[132].

dral angle evolution versus temperature (see Fig. 11.8a and 11.8b), since this angle is 60° in a cubic lattice but deviates from this value as soon as the lattice geometry changes. X-ray diffraction recorded during cooling confirms that the transition is reversible as the quenched sample structure is again rhombohedral. By measuring the unit cell, increase the thermal expansion was estimated as a function of the temperature (Fig.11.9a). Furthermore, a slight thermal expansion increase, possibly related also to the rhombohedral/cubic phase transition can be observed at temperatures higher than 800 °C. Oppositely, the BSCF material does not present any structural transition or decomposition during heating in air to 1000 °C as the results of synchrotron XRD measurements indicate, within the experimental accuracy of this technique. However, above 600 °C a significant increase of both the lattice parameter and the thermal expansion coefficient is measured, as reported in Fig.11.9b.

For characterization after aging temperature the LSCF specimens were exposed at 780 °C until 480 h (20 days) were analyzed with synchrotron radiation; no significant difference compared to the spectra of the as received material is noticed. Similar results were obtained on the specimens exposed at 820 °C for similar duration. These results confirm the stability of the LSCF compound in the examined temperature range, in agreement with the literature [134–137].

The BSCF aging treatments were done at the three temperatures 780, 800 and 820 °C, with durations increasing from few days up to several weeks. After aging in an air furnace, the specimens have differently colored surfaces: the side

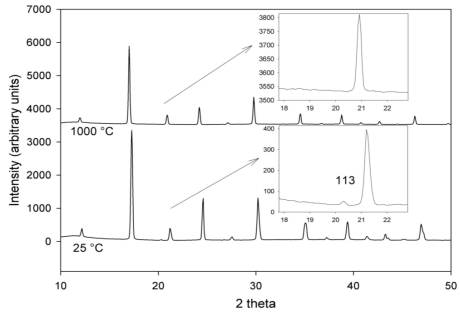

(a)

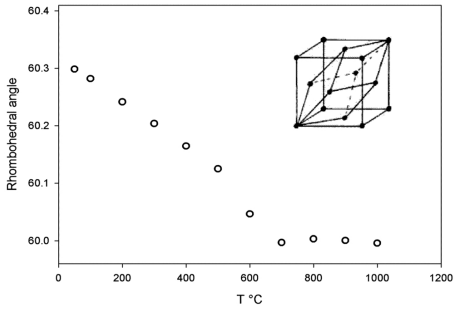

(b)

Figure 11.8: (a) Synchrotron XRD pattern of LSCF sample at 25 °C and 1000 °C. The difference between rhombohedral and cubic symmetry is marked by the disappearance of the 113 Bragg peak. (b) the rhombohedral to cubic transition is also described by the evolution of the cell angle in rhombohedral setting, which becomes 60 °C above 700 °C as expected for a metrically cubic lattice[132].

exposed to air is black and the other (in contact with the alumina specimen holder) is gray, similar to the as received material. After exposure times longer than 54 days a lamellar phase was presented (B9 specimen in Fig.11.10a). WDS mapping performed with the Jeol microprobe (Fig.11.10b and 11.10c) indicates that such a phase is rich in Co and poor in Fe compared to the matrix. This is expected for the hexagonal phase, known as (BaSr)CoO_3 having a precise crystallographic relation with the cubic perovskitic matrix [23]. Where a thicker

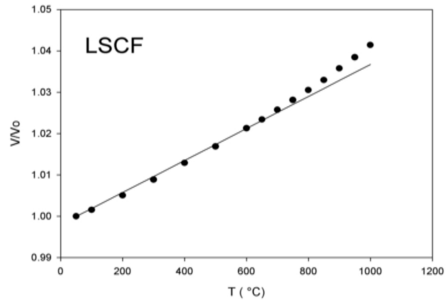

(a)

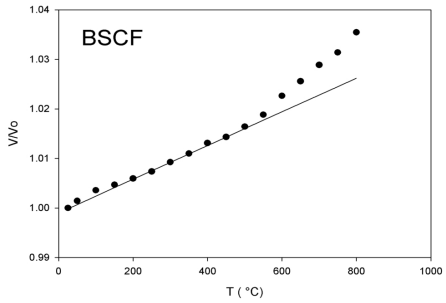

(b)

Figure 11.9: Thermal expansion measured by XRD of synchrotron radiation for (a) LSCF and (b) BSCF, respectively. Circles refer to experimental points. The line is calculated by fitting data up to 600 °C and extrapolating at higher temperature, to evidence the increase of thermal expansion above 600 °C[132].

hexagonal phase layer formed, an iron enrichment in the adjacent perovskite grain is clearly visible, as in the Fe map of Fig. 11.10c. Moreover, on the surface of the aged specimens, several particles rich in Co are present (Fig. 11.10b); Co oxides were already present in the as delivered material, but probably grew in number and size during high temperature exposure, even if no quantification effort was made here.

Moreover, LSCF and BSCF were tested in a glass permeation cell with a con-

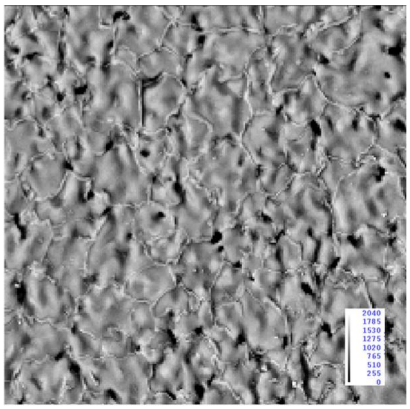

(a)

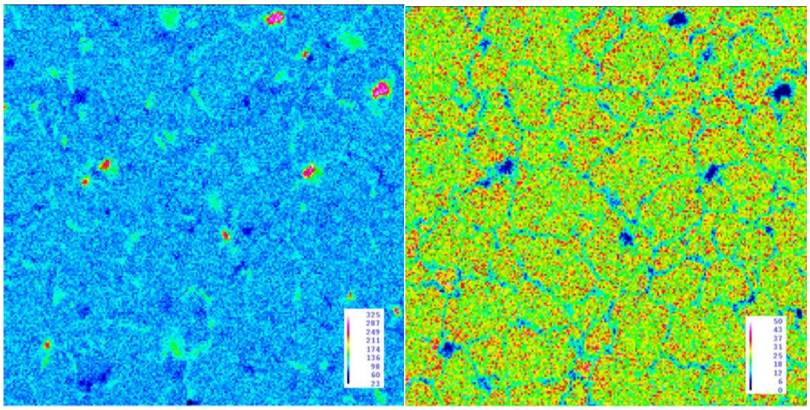

(b) (c)

Figure 11.10: (a) Surface morphology of B9 BSCF sample aged for 54 days. A secondary phase is present at the grain boundaries, as a lamellar phase. WDS mapping of sample B8 (aged 20 days at 780 °C) indicates that such phase is rich in (b) Co and poor in (c) Fe compared to the matrix.[132].

figuration similar to the scheme reported in Fig. 11.11, where the sealing was ensured thanks to the presence of two gold rings. Permeation tests were performed at atmospheric pressure and high temperature (750-1010 °C) under O_2 partial pressure gradients, by feeding a O_2 /N_2 mixture and a sweep gas (He)

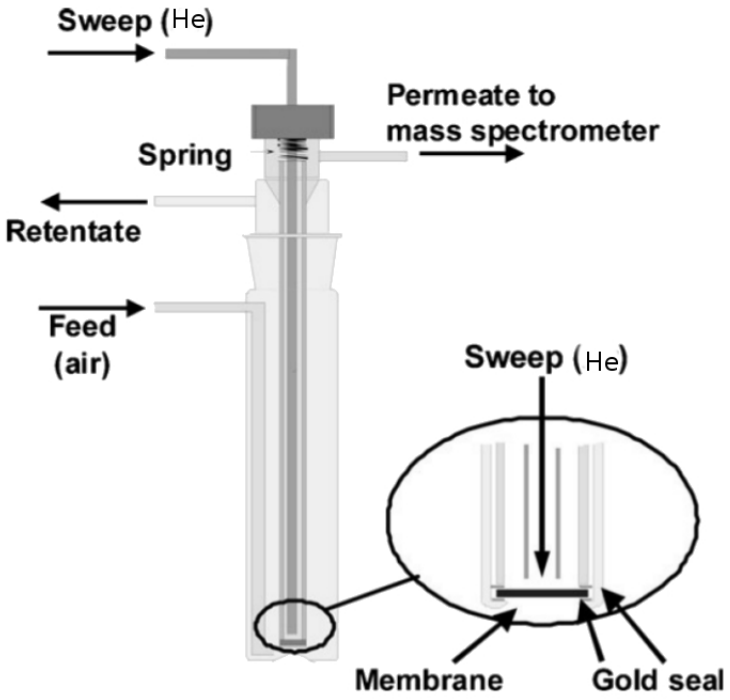

Figure 11.11: Setup of cell for permeation measurement[16].

with a flow rate of 250 N cm^3 /min and 50 N cm^3 /min, respectively. Three disc shaped membranes were tested: one LSCF (L2) and two BSCF (B1 and B2), in the testing conditions shown in Fig. 11.12. The experimental permeated O_2 fluxes (Fig. 11.13) are in line with the results reported in the literature for both materials [16, 25] and for all the membranes no difference in the oxygen flux was measured over time. After testing, the characterization of the morphology, crystal structure and chemical changes was performed by means of SEM + EDS and WDS, XRD and XPS, on both sides of the samples. The BSCF membranes B2 and B1 show some degradation at the two surfaces: the air (process) side shows swellings/cracking in regions where permeation was not occurring, probably owing to the oxygen adsorption and thermal cycles. On the surface of membrane B2 tested in air the morphology of the air side appears similar to the delivered

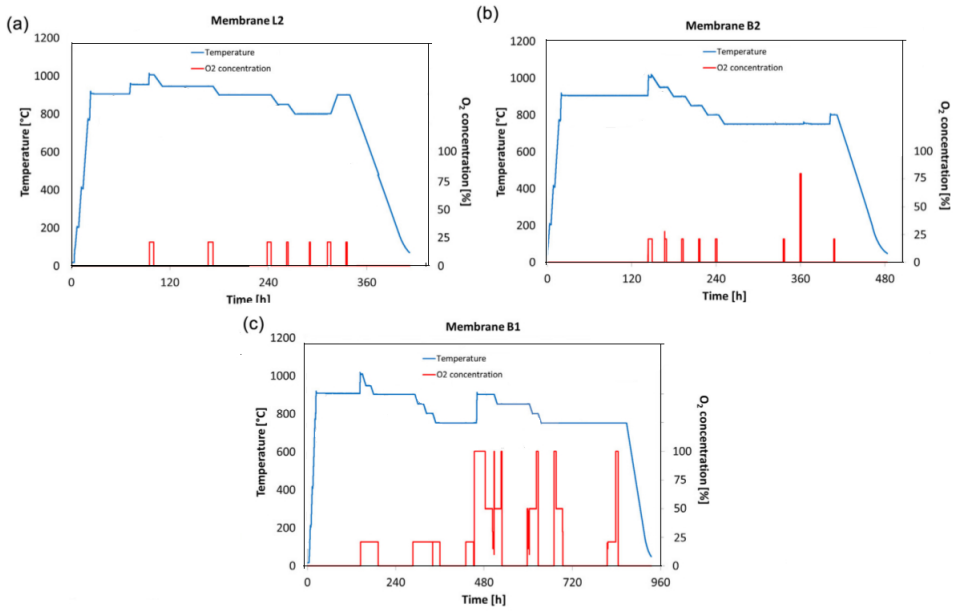

Figure 11.12: Temperature vs. time profile for permeation tests performed on membranes[132].

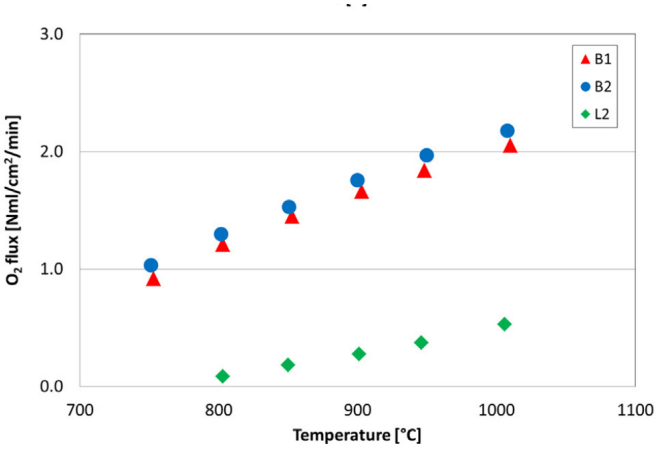

Figure 11.13: Permeation results of B1, B2 and L2 in terms of permeated oxygen flux[132].

material, but some swelling was observed in a small region (Fig.11.14a). On the sweep side, the surface morphology of B2 is rough only in some local regions, where areas with very different atomic weigh are evidenced by Backscattered Electron Images (see Fig.11.14c and 11.14d). In the WDS maps, the presence of Co oxides is quite clear and the heavy cations distribution is not uniform. Local quantitative WDS measurements show regions with quite different Fe contents. The decomposed layer is only about 1 micrometer thin on B2, as seen on a fractured surface.

Moreover, of the characterization discussed until now we have performed XPS analysis of the samples in order to be stabilized with a more precision chemical change in these membranes due to thermal treatments and permeation conditions. Now we will discuss in more detail the results. Due to the different work conditions of the sample sides we have performed different XPS measurements on two sides. The sides exposed to sweep gas are refereed with sweep in the name, while the sides exposed to feeding gas are refereed as air. We have also performed different treatments and measurements before sputtering process and after sputtering.
The line shapes are fitted with mixed singlets obtained by Voigt profiles sited on a Shirley background using the KolXPD software. The Gaussian contribu-

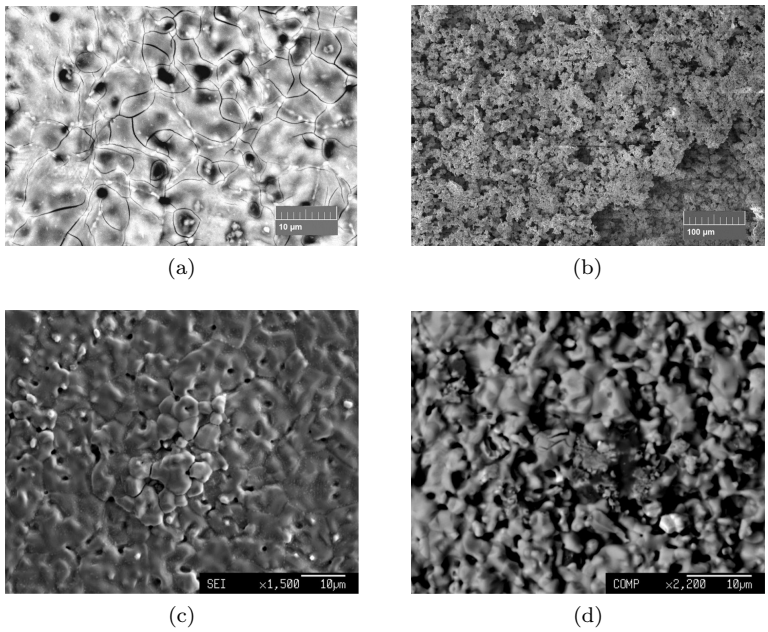

(a) (b)

(c) (d)

Figure 11.14: SEM morphology of the two sides of B1 and B2 membranes after permeation tests; (a) B1 air side swelling and cracking, (b) B1 sweep side rough areas, (c) B2 air side swelling and cracking, (d) B2 sweep side rough areas[132].

tion on full width half maximum (FWHM) profiles is taken fixed at 1.4eV while the Lorentzian contribution is different for a different orbital. This choice is made considering that the major Gaussian contribution to the shape is due to the apparatus while the Lorentzian contribution is due to the hole lifetime. We have also used the typical constrain of ratio intensity due to spin splitting. For d orbital there is a ratio of $2:3$ and for p orbital a ratio of $1:2$. The high resolution spectra presented in the following figures are the data after background subtraction, aligned of the lower energy carbon peaks at 284.8eV and each data are normalized with each area of fitting results. The relative intensity between fit and noise is different in sputtered and no sputtered sample. In particular the noise on C1s is less than in non-sputtered samples data meanwhile from the sputtering samples there is a higher noise. For the data of other elements present in the sample we have the opposite trend. This is due to the fact that

the carbon is only localized on the surface and cover the signal of the sample elements. With the sputtering process we remove this adventitious carbon so that the intensity of this element signal is closer to noise intensity.

11.1.1 LSCF

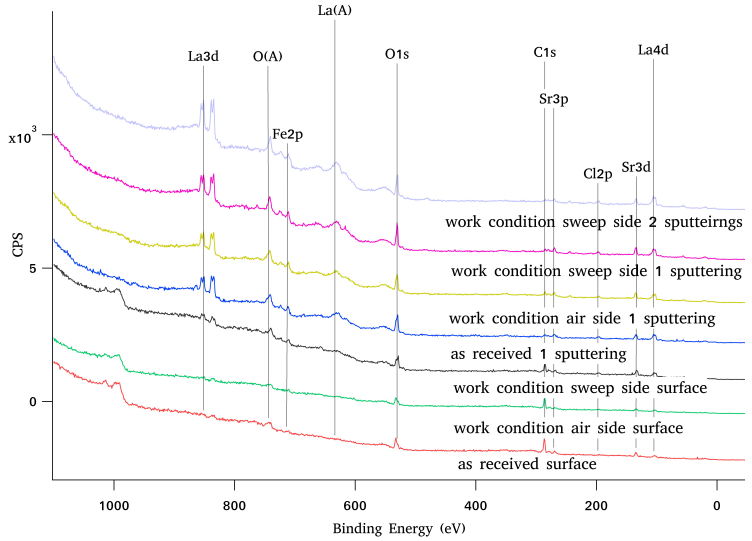

Figure 11.15: XPS wide spectra of LSCF

The wide spectra of LSCF are reported in Fig 11.15. In this figure, the elements that give an appreciable signal in the spectra and the suffix (A) after the element name indicating the Auger electrons. The first three spectra from the bottom are the as received samples and permeated sample before sputtering, feed (air) expose side, and sweep exposed respectively before sputtering. From these spectra we can see an appreciable signal from carbon and oxygen and very weak signals from the elements associate with the LSCF phase. It is only in the sweep side spectra that the intensity of the sample elements allows you to acquire a significant electron counts in high resolution spectra. In order to remove the adventitious carbon the as received sample was treated with argon sputtering at the energy of 3.5 keV for 15 min. On the permeated sample, we are interested in surface evolution and, in order to avoid remotion of a new

species we have made a sputtering for few minutes. The air and sweep side was sputtering for 2 min in Fig. 11.15. The sweep side, after this sputtering, presents more carbon that the air side, so another sputtering are made for 3 min.

11.1.1.0.1 La3d In deconvolving lanthanum La3d XPS signals, Fig. 11.16, was used a full width half maximum (FWHM) of 2.19eV using equation 4.15 in section 4.15 with a Lorentzian width of 1.3eV. The spin-orbit splitting was fixed to 16.8eV. This signal present a multiplet splitting [138].The green peak at 834.8 ± 0.8eV is due to the configuration $3d^9 4f^0$. The other two peaks, magenta and orange, are due to the configuration $3d^9 4f^1 L$ where L represent a hole in the ligand site. The magenta peak is due to electron-hole exchange[139] with total angular momentum quantum number $J = 1$ while the orange peak is for $J \neq 1$. The blue peak is a plasmon peak. The position of these three peaks are 834.4 ± 0.2eV, 835.7 ± 0.3eV and 836.4 ± 0.3eV respectively as reported in Table 11.1. These positions are compatible with lanthanum in the perovskite lattice. In the sweep spectra before sputtering the major contribution to the spectra is due to La3d shifted of 1.1eV to lower binding energy. This is due to the absence of some perovskite cations localized on the surface induced in permeation.

	peak $3d^9 f^0$	peak $3d^9 f^1 L$ $J = 1$	peak $3d^9 f^1 L$ $J \neq 1$	plasmons
as received	834.2	838.5	836.2	846.8
work condition air side 1 sputtering	834.5	838.9	836.5	847.3
work condition sweep side surface	833.1	837.4	835.2	846.3
work condition sweep side 1 sputtering	834.4	838.7	836.3	847.3
work condition sweep side 2 sputtering	834.6	839.0	836.7	847.5

Table 11.1: Peak positions for $La3d_{5/2}$ in LSCF

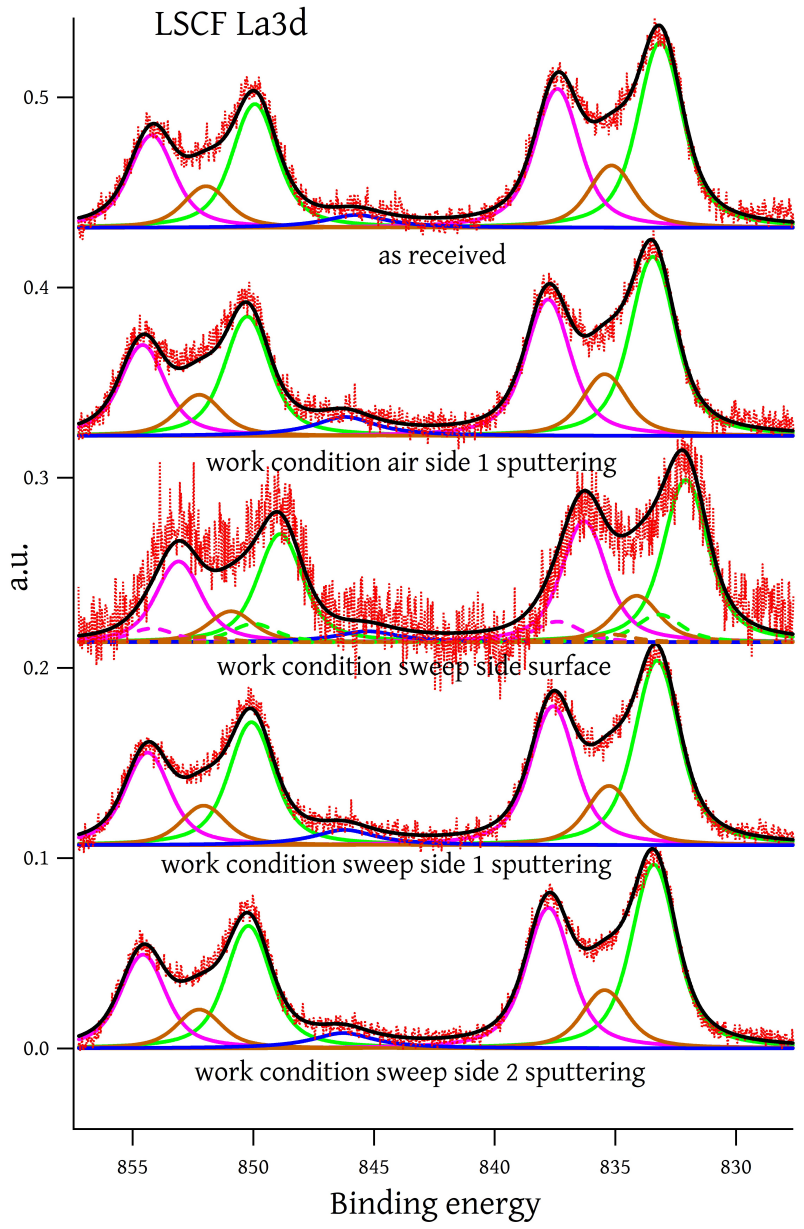

Figure 11.16: XPS high resolution spectra of La3d in LSCF

	$SrFeO_3$ (eV)	LSCF (eV)	SrO(eV)
as received		133.5	134.8
work condition air side 1 sputtering		133.8	135.0
work condition sweep side surface	131.8	133.8	
work condition sweep side 1 sputtering		133.5	134.8
work condition sweep side 2 sputtering		133.9	

Table 11.2: Position of $Sr3d_{5/2}$ peaks in LSCF

11.1.1.0.2 Sr3d In fitting strontium Sr3d was used a spin-orbit splitting of 1.7eV. In deconvolving the signals was used a FWHM 1.61eV and a Lorenztian width of 0.4eV. The as received spectra present two doublets as show in Fig. 11.17. The position peaks are summarized in table 11.2. The peak at 133.7 ± 0.2eV is compatible with strontium from bulk LSCF lattice while the one at 134.9 ± 0.1eV can be due to strontium oxide on surface. In the sweep spectra before sputtering the doublet due to strontium oxide disappears and instead there is a doublet at 131.8eV compatible with Sr^+ in $SrFeO_3$[140]. The presence of this element is confirmed by the peak of oxygen at 528.5 [141]. The $SrFeO_3$ is localized on surface in fact after sputtering this peak disappears.

In the as received sample, sputtering for fifteen minutes, the strontium oxide peak has a little less intensity in comparison with the signal from Sr in LSCF. Instead after a sputtering for two minutes, in both air side and sweep side the signal from strontium oxide is less intense in comparison with the as received and disappear leaving only the signal from LSCF after a second sputtering on sweep side. This behavior seems to indicate that the permeation bring on surface the strontium oxide that in the first atom layers was bonding in $SrFeO_3$ giving the peak a lower binding energy 131.8eV. The percentage of Sr in A perovskite site different measurement is reported in table 11.3.

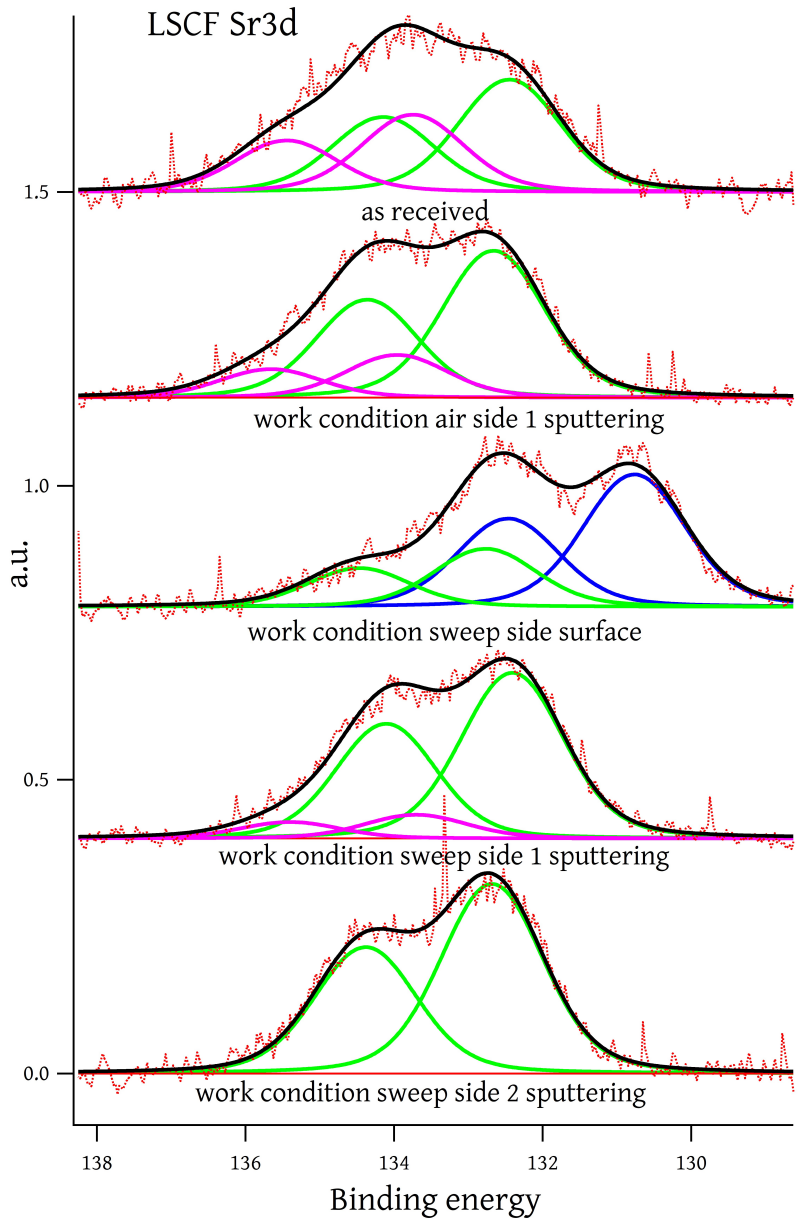

Figure 11.17: XPS high resolution spectra of Sr3d in LSCF

	$SrFeO_3$	Sr bulk	SrO	Sr percentage in A site
as received		23%	16%	39%
work condition air side 1 sputtering		39%	11%	50%
work condition sweep side surface	52%	22%		74%
work condition sweep side 1 sputtering		41%	6%	47%
work condition sweep side 2 sputtering		32%		32%

Table 11.3: Percentage of Sr3d peaks in A site in LSCF

11.1.1.0.3 O1s In deconvolving the oxygen spectra was used a FWHM 1.58eV with a Lorentzian width of 0.34eV. The oxygen O1s spectra are show in Fig.11.18. The green peak at 529.9 ± 0.1eV is compatible with oxygen in LSCF lattice [142]. This peak can have also contribution from cobalt and iron oxides. Unfortunately the signal from these elements does not allow a deconvolution in order to confirm and quantify the presence of these compounds. This peak at 529.9 ± 0.1 is the main peak for all spectra except for the one from sweep face before sputtering. In this case the main peak is located at 528.5eV, as reported in Table 11.4 that is compatible with electron enrich oxygen due to the presence $SrFeO_3$ [141]. The peak at 531.5 ± 0.1eV is compatible with strontium oxide. The other peaks are due to iron and cobalt oxide. These elements can have different valence state and form different oxides, but the XPS signal of these elements do not allow a good interpretation in order to assign the oxygen peaks to the different oxides.

11.1.2 BSCF

In the wide spectra of BSCF, reported in Fig.11.19, the adventitious carbon hides the signal from the sample elements. Only for the sweep side and for thermal treatment sample,(in Fig.11.19 780 °C 54 days surface), the intensity of sample elements allows for obtaining significant electron counts in high resolu-

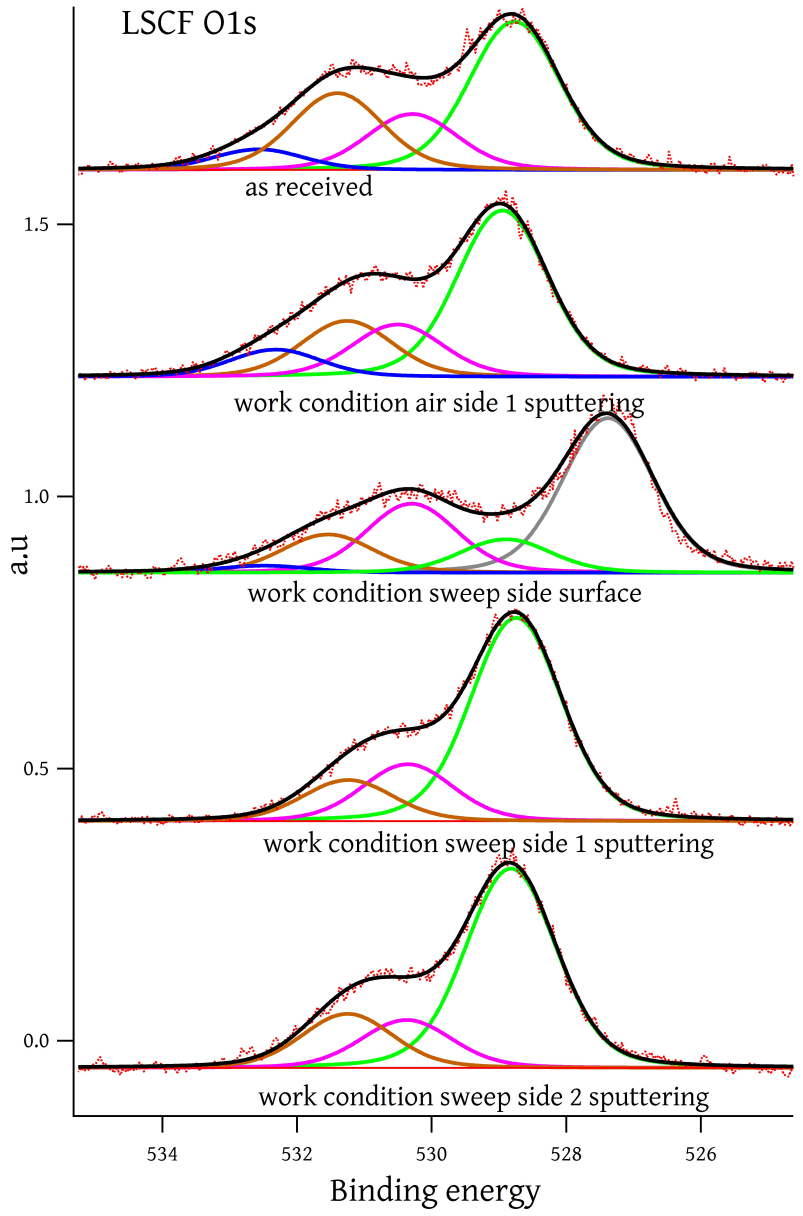

Figure 11.18: XPS high resolution spectra of O1s in LSCF

	$SrFeO_3$	LSCF	SrO	peak3	peak 4
as received		529.8	531.4	532.5	533.6
work condition air side 1 sputtering		530.0	531.6	532.3	533.4
work condition sweep side surface	528.5	530.0	531.4	532.6	533.6
work condition sweep side 1 sputtering		529.8	531.4	532.3	
work condition sweep side 2 sputtering		530	531.6	532.5	

Table 11.4: Peak positions O1s in LSCF

tion spectra. The as received sample was sputtered with Ar ions at the energy of 3.5keV for 9 min while permeated sample on sweep side was sputtered for 3 min. and the air side for 2 min while the thermal treated sample was sputtered for 30 min. From the thermal treated wide spectra, the peak at about 684.8eV is compatible with fluorine presence maybe due to a contamination on the oven.

11.1.2.0.1 Ba4d In deconvolving the Barium Ba4d signal was used a spin-orbit splitting of 2.6eV. The FWHM is 1.56eV with a Lorentzian width of 0.3eV. All measurements, as reported in Fig. 11.20, have a peak between $89.7-90.0$eV compatible with barium from BSCF, except for thermal treated sample before sputtering as show in Table 11.5. In the permeated sample, which was exposed to mixture of a oxygen and nitrogen, there is an additional doublet at $92.1-92.2$eV on both sides compatible with the presence of barium dioxide BaO_2 while the peak at $91.0-91.1$eV is compatible with barium oxide BaO that is presently also in the as received sample. The oxides are not completely localized on surface in fact even if the signal decrease after sputtering it does not disappear in the as received sample sputtered for 15 minutes. In the thermal treated samples before sputtering, there is a peak at 87.3eV compatible with BaF_2. The fluorine can be due to a contamination in oven during thermal treatment. The BaF_2 is localized on surface in fact after sputtering the signal from this compound disappears. In the same spectra there is a peak at 89.3eV compatible with the presence of

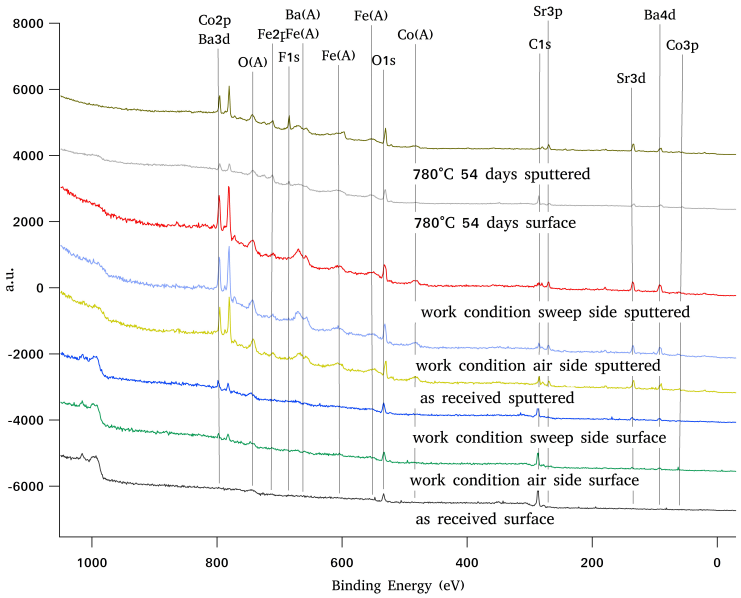

Figure 11.19: XPS wide spectra BSCF

barium carbonate; this fact is also mirrored in carbon spectra. In the thermal treatment sputtered sample, the peak at 90eV is likely due to barium in BSCF lattice.

	BaF_2	$BaCO_3$	BSCF	BaO	BaO_2
as received			89.7	91.0	
work condition air side sputtered			89.8	91.0	92.1
work condition sweep side surface			89.7	91	92.2
work condition sweep side sputtered			89.8	91.1	92.2
780 °C 52 days surface	87.3	89.3			
780 °C 52 days sputtering		89.3	90.0		

Table 11.5: peak positions of $Ba4d_{5/2}$ in BSCF

11.1.2.0.2 Ba3d and Co2p The Ba3d signal overlaps the Co2p. In deconvolving these signals was used for Ba3d a spin-orbit splitting of 15.4eV, and an FWHM of 2.52eV with a Lorentzian width of 1.75eV. The Ba3d signal, in comparison with the Ba4d signal, is due to electrons nearest to the core, so these electrons are less sensitive to chemical shift. For this reason, the contribution to the different chemical species is summed in only one doublet, the green lines in Fig.11.21. This peak is at 789.5± 0.2eV for all spectra except for thermal treated sample before sputtering in which the peak is at 779.6eV, as reported in Table 11.6. For these spectra the structure of the Ba4d total fit is shifted due to the presence of BaF_2 and $BaCO_3$ and absence of a signal from BSCF lattice barium. Using the sensitive factor the Ba4d signal intensity can be converted in a Ba3d signal and the remaining area of the peak is due to the presence of Co2p signal. In deconvolving, the Co2p signal was used a spin-orbit splitting with a fix distance of 15.4eV and an FWHM of 1.7eV with a Lorentzian width of

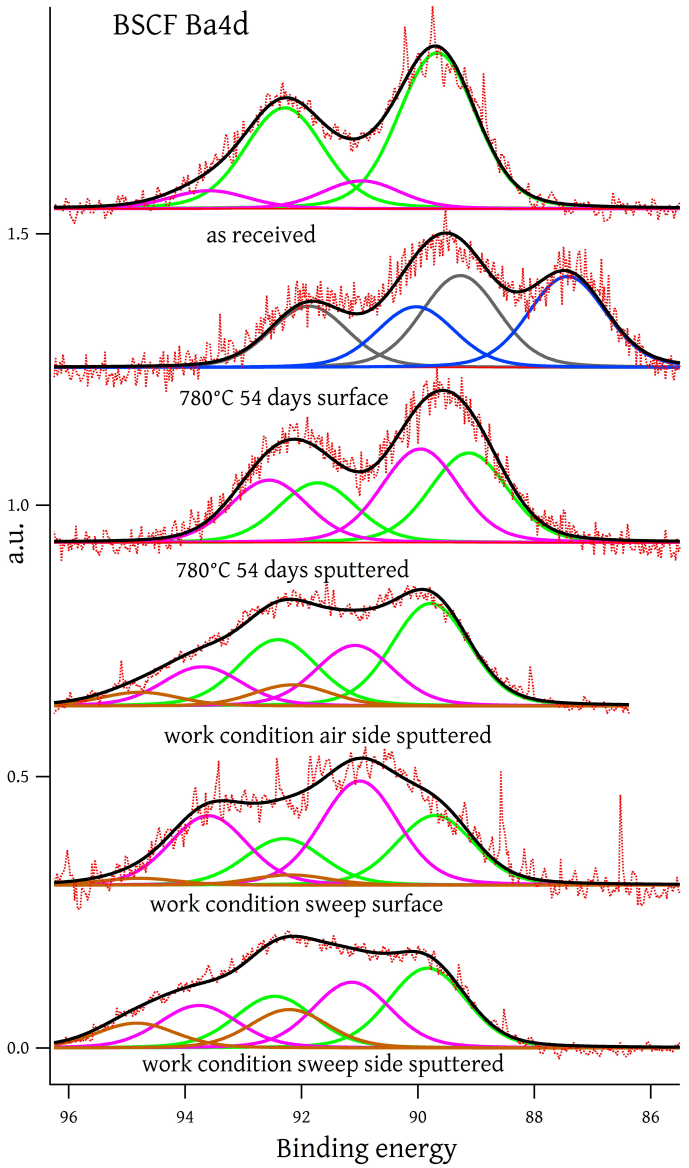

Figure 11.20: XPS high resolution spectra of Ba4d in BSCF

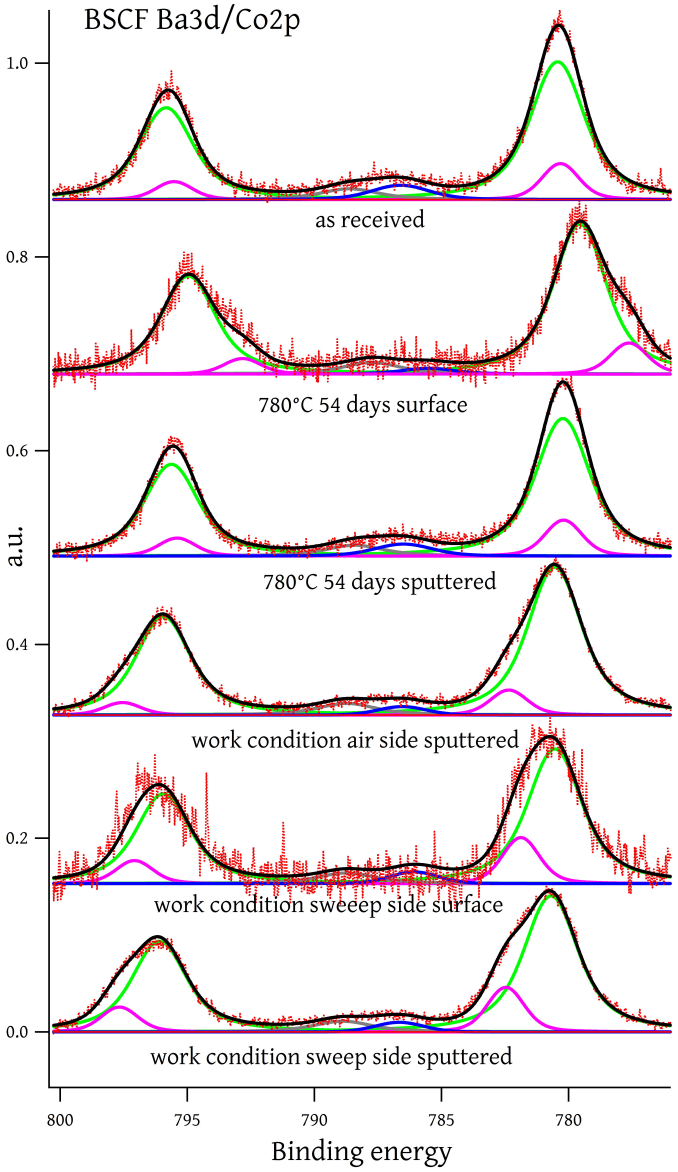

Figure 11.21: XPS high resolution spectra of Ba3d/Co2p in BSCF

0.56eV, magenta line in Fig.11.21. The position of this peak change in different spectra due to the presence of cobalt with different valence. For the as received sample the Co2p main peak at 780.2eV is compatible with Co^{3+}. After thermal treatment the position is at 779.6eV compatible with the presence of Co^{2+}. In Refs.[143] C. Norman and C.Leach report the same reduction of cobalt in thermal treatment. In their work, both Co^{2+} and Co^{3+} presences were found, while our data show only Co^{2+}. This can be due to the different thermal treatment. In their work, the Co2p spectra, with Co^{3+} presence, was acquired from the sample heated at 800 °C for 30 min, while our sample was heated to 750 °C for 1300 h. In the spectra after sputtering, the doublet is located at 780.4eV compatible with Co^{3+}. This indicated that the cobalt with lower valence is localized on the surface. In the permeated sample after sputtering the doublet is at $782.4 - 782.5$eV for both side while before sputtering on sweep side the doublet is at 781.9eV. These three positions are all compatible with Co^{4+} and the shift between sputtering and no sputtering spectra are likely due to different chemical bonding. The structures between spin-orbit doublets are due to ghost peak, gray line in Fig.11.21, and satellite from cobalt[144], blue line.

	Ba3d	Co2p	Co2p satellite
as received	780.3	780.2	786.5
work condition air side sputtered	780.5	782.4	786.6
work condition sweep side surface	780.5	781 .9	786.1
work condition sweep side sputtered	780.7	782.5	786.7
780 °C 52 days surface	779.6	777.4	785.5
780 °C 52 days sputtered	780.3	780.4	786.5

Table 11.6: Peak positions of $Ba3d_{5/2}$ and $Co2p_{3/2}$ in BSCF

Sr3d In deconvolving the strontium Sr3d spectra, as reported in Fig. 11.22, was used a spin-orbit splitting of 1.7eV with a ration between area of 2 : 3. In deconvolving, the signals are used an FWHM 1.61eV and a Lorenztian width of 0.4eV. In all spectra there is a peak at 133.4 ± 0.1eV compatible with strontium in BSCF lattice as show in Table 11.7. In the as received sample and permeated on both side there is also a peak at 134.5 ± 0.1 compatible with strontium oxide SrO. In the thermal treatment sample before sputtering, called B9_nsp, there is a peak at 131.6eV compatible with $SrFeO_{3-\delta}$[145] that was mirrored in oxygen peak at 528eV. The peaks at 135.6 ± 0.2eV in the permeated sample are compatible with $SrCO_3$.

	$SrFeO_{3-\delta}$	BSCF	SrO	$SrCO_3$
as received		133.3	134.3	
work condition air side sputtered		133.4	134.4	135.8
work condition sweep side surface		133.3	134.4	135.4
work condition sweep side sputtered		133.4	134.3	135.5
780 °C 52 days surface	131.6	133.3		
780 °C 52 days sputtered		133.4		

Table 11.7: Position of $Sr3d_{5/2}$ peaks in BSCF

11.1.2.0.3 O1s In deconvolving the oxygen spectra was used an FWHM 1.58eV with a Lorentzian width of 0.34eV. The oxygen O1s spectra are show in Fig.11.23. In Table 11.8 the peak position is reported. All the spectra have a peak at 529.8 ± 0.2 compatible with oxygen in lattice of BSCF. In sweep side before sputtering there is a peak at 528.0eV compatible with oxygen from $SrFeO_{3-\delta}$[145], this peak has a low area and the corresponding Sr signal is too low to be deconvolved in strontium spectra. This peak is mirrored in Sr spectra

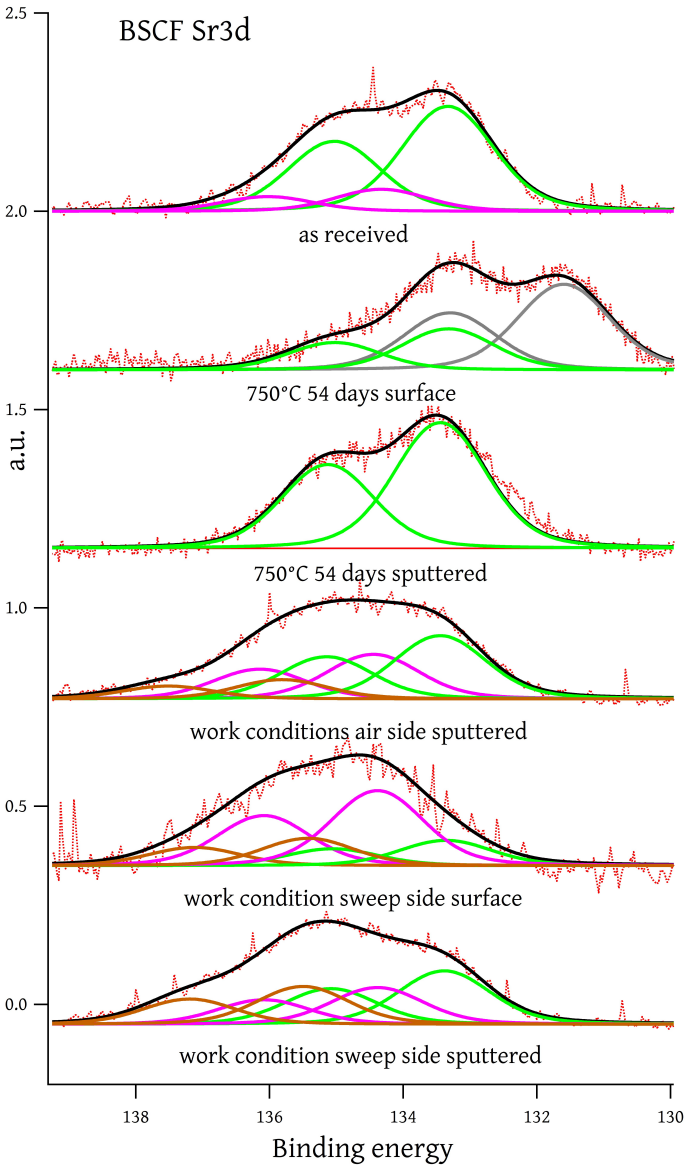

Figure 11.22: XPS high resolution spectra of Sr3d in BSCF

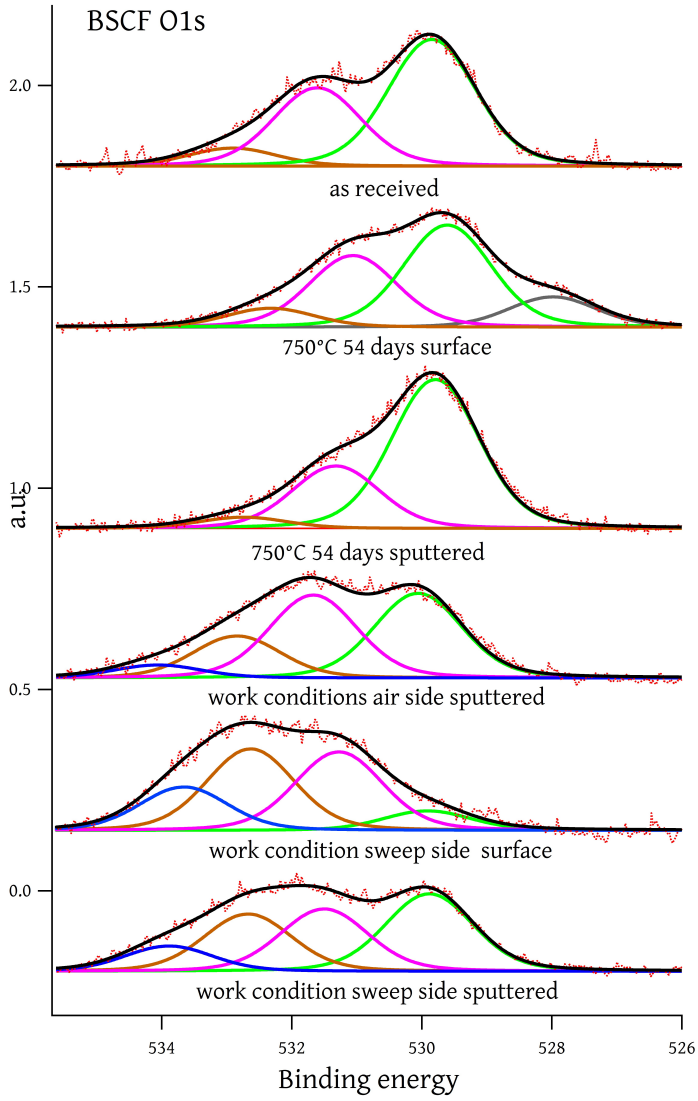

Figure 11.23: XPS high resolution spectra of O1s in BSCF

	$SrFeO_{3-\delta}$	BSCF	peak2	peak3	$SrCO_3$
as received		529.8	531.4	532.7	
work condition air side sputtered		530	531.7	532.8	534
work condition sweep side surface		529.6	531.0	532.3	533.3
work condition sweep side sputtered		529.9	531.5	532.7	533.9
780 °C 52 days surface	528.0	529.6	531.0	532.3	
780 °C 52 days sputtered		529.9	531.4	532.9	

Table 11.8: O1s peak position in BSCF

peak at 131.6eV. We can also notice that the peak at 532.6 ± 0.3eV, the orange one, is more intense in the last three spectra for which we have the presence of Co^{4+}, so they can be related to the presence of cobalt oxide.

11.1.3 Conclusion

Due to the weak signal from iron and cobalt we cannot analyze these elements. However for LSCF we can identify the signal from bulk with the oxygen peak at 529.8 ± 0.2eV, the lanthanum peak at 834.4 ± 0.2eV with related bonding and antibonding peaks and the strontium doublet at 133.7 ± 0.2eV. In the as received sample and in the permeated sample on the side exposed to feed gas after sputtering and on the side exposed to sweep gas after the first and the second sputtering there is a strontium peak at 134.9 ± 0.1eV compatible with the presence of strontium oxide where the corresponding oxygen peak is located at 531.5 ± 0.1eV. The area of this last peak has also contribution from other oxygen bonding with carbon. Considering the percentage of elements in the perovskite A side, e.g., lanthanum and strontium, as reported in Table 11.3, there is a depletion of strontium in the inner part and an excess on the surface

for the sweep side. On the side expose to sweep before sputtering there is not strontium oxide, but we have a peak to lower binding energy due to the presence of $SrFeO_3$ mirrored in the oxygen peak at 528.5eV. Also lanthanum presents a peak to lower binding energy only in the sweep side before sputtering due to the absence of some perovskite cations localized on the surface induced in permeation. In BSCF after thermal treatment before sputtering there is a presence of low energy peak in barium at 87.3eV compatible with BaF_2, due to a contamination in the oven, while the peak at 89.3eV is due to barium carbonate. This last peak is not presented in the permeated sample. We can deduce that the permeation prevents the formation of barium carbonate and promote the formation of strontium carbonate, peak at 135.6 ± 0.2eV. Moreover, in the thermally treated sample before sputtering there is a presence of $SrFeO_{3-\delta}$ deduced from the $Sr3d_{5/2}$ peak at 131.6eV and the O1s peak at 528eV. In BSCF there is an evolution of the cobalt peak. In the as received sample a thermal treated sample after sputtering the position of $Co2p_{3/2}$ peak is compatible with Co^{3+}, while before sputtering, after thermal treatment,the Co peak position is compatible with Co^{2+}. Therefor the thermal treatment induced the cobalt to assume a lower valence on surface. In the permeated sample, on both sides, the Co peak position is compatible with a higher valence Co^{4+}. Both BSCF and LSCF present and evolution after work condition, the Sr evolution is similar in both samples while the La seems to be more stable than Ba.

Chapter 12

Conclusion

In this work we have seen three ceramic materials: nanostructured zirconia thin film, LSCF and BSCF. All of these three materials can be used in reducing environmental pollution. In particular the first one seems be a good candidate in Dry Reforming Methane (DRM) and as an electrolyte in Solid Oxide Fuel Cell (SOFC), while the latter two materials can be used as Mixed Ionic-Electronic Conducting (MIEC) membranes. In all of these applications the working condition, unless nanostructured thin films, is at a high temperature (around 700 °C), and the performance depends on the stability of these materials at working temperature. This stability includes a chemical reaction and crystal phase. Moreover, the use of nanostructured zirconia thin film can lower the working temperature [11].
From the literature the nanostructured thin film properties depend on the synthesis modes. In particular, our nanostructured zirconia thin film made by SCBD has a roughness that does not significantly change with thermal treatments as reported in Ref. [30]. In this work, some preliminary characterizations of the nanostructured zirconia thin film were presented after thermal treatments by XPS and XRPD. The first characterization technique gives information on the surface with a depth of 10 nm, while the latter one gives information on all of the materials that have a thickness of 180 nm.
The main property that emerges from these characterizations is the stability of the cubic phase at room temperature, that can be due to the substoichiometry of the materials, as suggested by the simulation made in this work. From XRPD the cubic phase is stable at least up to 110 °C in air, and to 400 °C in a poor oxygen environment. This is a very important result because in the

previous mentioned application, but also in other applications of zirconia the cubic phase gives the best performance versus monoclinic. Moreover, the behavior under thermal treatment is also influenced by the substrate. Therefor, this material can be a good candidate for DRM and SOFC.
Nanostructured zirconia thin film made by SCBD is a relatively new material, and we are at the beginning as regards learning how this material reacts to different condition, and how it can be used. Instead, LSCF and BSCF materials are more know. So we have a disposition of more data from the literature. In this work we present a study of these materials, with the collaboration of the RSE SpA - Ricerca sul Sistema Energetico, using different techniques before and after the work condition. The main question we want to answer is which one is the best as MIEC. From the XPS data, which is the specific characterization that I have performed, it seems that the LSCF is chemically more stable than BSCF, so in the long-term working condition, it could can be the best choice.
LSCF can also be used as a cathode in SOFC. Therefor, we can combine nanostructure zirconia thin film with LSCF in order to make an efficient SOFC [146]. It is in this way that we need to conduct more studies on combining these two materials due to the high susceptibility of nanostructured zirconia thin film to the environment and substrate.

List of Publications

Ab initio electronic structure, optical, and magneto-optical properties of MnGaAs digital ferromagnetic heterostructures

Patrizia Rosa,[1,2] Davide Sangalli,[2,3,4] Giovanni Onida,[1,4] and Alberto Debernardi[2,*]
[1]*Dipartimento di Fisica, Univesità degli studi di Milano, via Celoria 16, I-20133 Milano, Italy*
[2]*CNR-IMM, Unità Operativa di Supporto Agrate Brianza, via Olivetti 2, I-20864 Agrate Brianza, Italy*
[3]*CNR-ISM, Unità Operativa di Supporto di Montelibretti, via Salaria Km 29.3, I-00016 Montelibretti, Italy*
[4]*European Theoretical Spectroscopy Facility, Via Celoria 16, 20133 Milano, Italy*
(Received 9 December 2014; published 24 February 2015)

We report on a theoretical study of the electronic, optical, and magneto-optical properties of digital ferromagnetic heterostructures based on Mn δ-doped GaAs. We consider different structures corresponding to Mn contents within the range 12%–50% and we study how the system changes as a function of the doping concentration. Our first-principles approach includes the spin-orbit interaction in a fully relativistic pseudopotential scheme and the local-field effect in the description of the optical absorption. We show that Mn δ-doped GaAs shares many properties with the uniformly doped $Ga_{1-x}Mn_xAs$ system, i.e., half-metallicity, similar absorption spectra, and moderate Kerr rotation angles in the visible spectral region.

DOI: 10.1103/PhysRevB.91.075207 PACS number(s): 71.45.Gm, 75.70.Cn, 75.70.Tj, 78.20.Ls

I. INTRODUCTION

Digital ferromagnetic heterostructures (DFHs) have been recently proposed as a way to overcome some of the drawbacks of random-doped $Ga_{1-x}Mn_xAs$ diluted magnetic semiconductors (DMSs), without loosing the peculiar properties of the latter connected with the possibility to exploit spin-polarization effects within a semiconducting (or half-metallic) medium compatible with the present technology of semiconductor electronic devices [1]. Mn-based DFHs in III-V semiconductors are superlattice heterostructures where (fully or partially filled) monolayers (MLs) of Mn, which is substitutional to cation group III elements, are spaced by a fixed number of layers of the III-V compound. On one hand, these δ-doped structures allow a concentration of Mn higher than in random-doped (Mn) III-V semiconductors, and thus, due to the different valence between the group III atom and the substitutional Mn, can produce in principle a larger concentration of holes, enhancing the Curie temperature (T_C) of the system. On the other hand, DMS T_C can increase considerably also because it depends on the spatial distribution of magnetic ions, which can change substantially in low-dimensional systems: Nazmul and co-workers [2] showed that in a p-type selectively doped III-V heterostructured composed of Mn δ-doped GaAs/p-AlGaAs a remarkably high T_C of about 250 K can be reached; in Ref. [3] Chen *et al.* report T_C well above room temperature in GaSb/Mn digital alloys.

Possible applications of DMSs range from spintronics (i.e., the idea to use the spin degree of freedom in order to transmit, write, or store digital data) [4,5] to the use of spin-polarized currents for the study of surface magnetism and magnetic anisotropies in materials. In this respect, half metals, which are conductive in one spin channel and semiconducting in the other, are ideal candidates to build spin injectors. Many DMSs have indeed a half-metallic behavior [1]. Moreover, several DMSs also display intriguing magneto-optical coupling effects: an example is the magneto-optical Kerr effect [6] (MOKE), i.e., the polarization rotation of the light reflected by the surface of a magnetic material, which is at the basis of the operation of magneto-optical data storage media. Moreover, the MOKE can be used in the study of electronic structure in magnetic materials.

Previous studies of GaAs-based DFHs include the experimental realization, by means of low-temperature molecular beam epitaxy (MBE), of GaAs/$Ga_{1-x}AsMn_x$, separated by GaAs spacers of variable thicknesses [7], and measurements of their optical conductivity spectra in the infrared region [8].

On the theoretical point of view the optical and magneto-optical properties of Mn-doped GaAs have been studied by means of the linearized full-potential methods [9,10] (FLAPW approach) or by the Korringa-Kohn-Rostoker method [11], but only in the case of a uniform $Ga_{1-x}Mn_xAs$ doping. *Ab initio* theoretical predictions for the magneto-optical properties of DFHs are hence lacking.

A possible advantage of DFH δ-doped structures with respect to uniformly doped $Ga_{1-x}Mn_xAs$ DMSs derives from the possible amplification of MOKE effects by exciton confinement. However, also local field effects (corresponding indeed to the electron-hole exchange in the excitonic Hamiltonian [12]) may play an important role in such a strongly anisotropic system. However, the intrinsic complexity of DFHs, with unit cells containing many atoms, makes the direct application of full-potential methods such as those of Refs. [9,10] computationally prohibitive.

On the other hand, more efficient *ab initio* methods based on pseudopotentials (PPs) and plane waves have not been systematically used for the study of MOKE spectra, because of the common wisdom that an all-electron approach was required in order to describe the wave function within the core region [where the spin-orbit (SO) interaction is stronger]. Instead, some of us have recently demonstrated that, provided that the spin-orbit interaction is fully taken into account in the construction and use of "fully relativistic" PPs, the plane-wave-based approach provides results of the same quality as those of all-electron calculations [13].

*alberto.debernardi@mdm.imm.cnr.it

Indeed the MOKE is due to a different dielectric response for right (ϵ_+) and left (ϵ_-) circularly polarized light, which stems from the difference between the wave functions with $+L_z$ character and $-L_z$ character. In a magnetic material this difference is due to the SO coupling in the Hamiltonian, $H = \xi \mathbf{L} \cdot \mathbf{S}$, which transfers the spontaneous symmetry breaking between the $+S_z$ and the $-S_z$ spin component to the spatial part of the wave function. Thus the MOKE cannot be captured by a perturbative description of the SO effect or by the use of scalar relativistic PPs, which only include the effect of the SO in the energy levels without affecting the wave function.

In this work we hence perform first-principles simulation of Mn δ-doped GaAs structures [7], including the effect of the SO in a nonperturbative way and using fully relativistic PPs. We then compute the absorption coefficients of the system and the MOKE parameters in the so-called polar geometry, where the magnetization vector is oriented perpendicular to the reflective surface and parallel to the plane of incidence. This is the most studied geometry and the one which gives the largest Kerr rotation.

This work is organized as follows. In Sec. II we present DFT-LDA ground state results and Kohn-Sham (KS) band structure for heterostructures described by 8-, 6-, 4-, and 2-layer supercells (SCs), corresponding to doping concentrations from 12.5% to 50% (see Fig. 1). We show the electronic density of states, projected onto spin components, atomic species, and $s/p/d$ angular momenta. In Sec. III we deal with optical absorption spectra, computed within the linear response scheme in the random-phase approximation (RPA), and compared with experiments. We then extend our analysis to magneto-optical effects in Sec. III A, after briefly summarizing the basic equations for the MOKE and MCD spectra, and we discuss our results analyzing the similarities and differences with the case of uniform doping. Finally, in Sec. IV we draw our conclusions.

II. ELECTRONIC PROPERTIES OF Mn-DOPED GaAs: δ DOPING

We model Mn δ-doped GaAs by means of the periodic superstructures shown in Fig. 1. The variable thickness of bare GaAs interposed between MnAs layers allows us to simulate δ-doped materials with 12%, 16%, 25%, and 50% of Mn atoms replacing Ga ones (with the latter case corresponding to a hypothetical GaAs/MnAs superlattice).

We perform our calculations with DFT-LDA [14–16] in the plane-wave PP scheme, as implemented in the Quantum ESPRESSO (QE) package [17]. To take into account the spin-orbit effects on the valence wave functions, the use of fully relativistic (norm-conserving) PPs is necessary. Moreover, the presence of noncollinear spin polarization (i.e., spinorial KS wave functions) must be allowed. Both features are available in QE. We use tetragonal unit cells, by relaxing the lattice parameter along the growth direction (perpendicular to the Mn-doped layers) and all the atomic positions within the unit cell [18]. The in-plane lattice parameter is kept fixed at its bulk GaAs value, consistently with an epitaxial growth on the GaAs (001) oriented substrate. Ground-state calculations are performed with a kinetic energy cutoff of 50 Ry (680 eV) for the wave functions, and a Monkhorst-Pack [19] grid $12\times12\times n$ for the Brillouin zone (BZ) with $n = 8,4,3,2$ for the two-, four-, six-, and eight-layer SCs, respectively, thus maintaining an (approximately) uniform mesh in the BZ. The ground state of

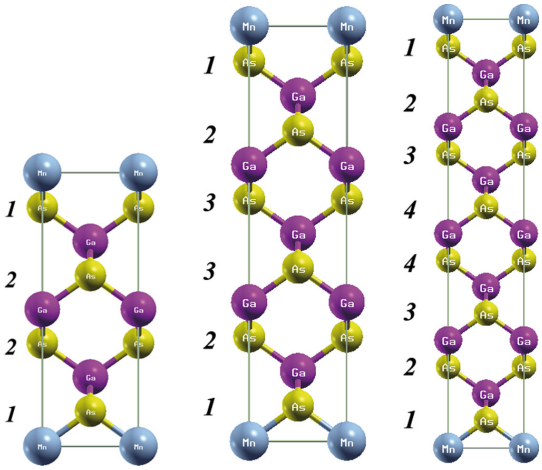

FIG. 1. (Color online) Atomic structure (unit cells) of some of the studied δ-doped materials. Yellow spheres are As atoms, the violet ones represent Ga, and the cyan color is used for Mn. The corresponding Mn-doping concentrations are 12.5% (rightmost structure, an 8-layer supercell with 7 GaAs layers separating MnAs ones); 16.7% (6-layer supercell with 5 GaAs layers); 25% (leftmost, 4-layer supercell with 3 GaAs layers); 50% (2-layer supercell, not shown).

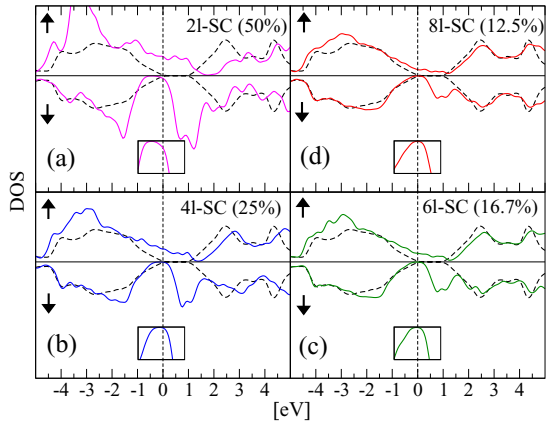

FIG. 2. (Color online) Spin-resolved density of states of the four studied Mn-doped GaAs heterostructures, compared with that of bulk GaAs (black dashed line). Panels (a) to (d) correspond to decreasing Mn concentrations, from 50% to 12.5%. Spin-up and spin-down components are computed by projecting the spinorial wave functions onto the S_z-spin eigenstates. The inset of each figure shows a zoom in the vertical scale of the density of states in the minority-spin channel close to the Fermi level.

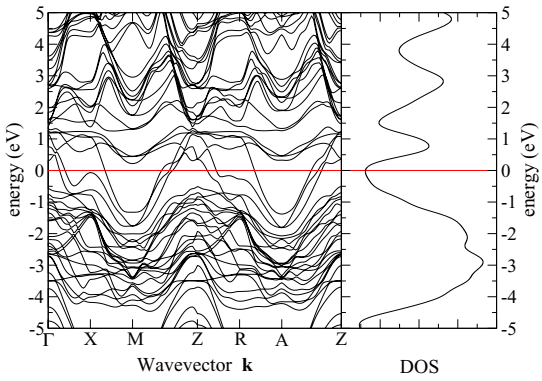

FIG. 3. (Color online) Kohn-Sham band structure and total DOS for the 25% doping case [panel (b) of Fig. 2]. The red line is drawn at the Fermi energy.

bulk GaAs, which is also considered for reference, is computed using a $12\times12\times12$ sampling.

We compare the density of states at the KS level [20], for the four systems considered, in Fig. 2. All the Mn-containing systems have a metallic character, as expected. The case of undoped bulk GaAs is also shown for comparison. Doped systems clearly display a nonzero DOS at the Fermi level, with a characteristic Mn-related structure lying in the top region of the bulk band gap. The 50% doped structure [panel (a)] clearly deviates from the behaviors shown by lower-doping systems, both at the level of the DOS and in term of Fermi surface topology. This difference can be clearly seen in the band structure, where the number of bands appearing to cross the Fermi level increases from three (see, e.g., Fig. 3), for the lower doping cases, to four (see Fig. 4) in the 50% doped system. At the same time, the DOS of the 50% doped case displays a clear reduction of the spectral weight around 2.5 eV above E_F, typical of bulk GaAs, in favor of lower energy structures.

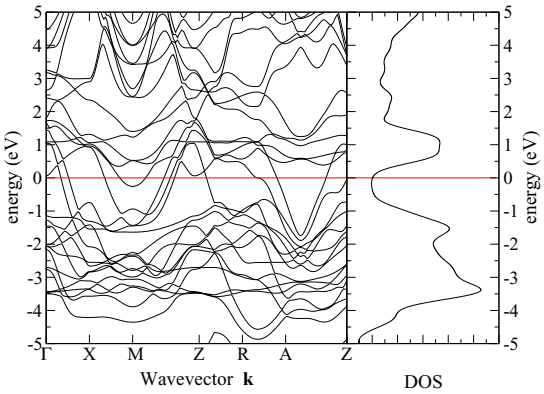

FIG. 4. (Color online) Kohn-Sham band structure and total DOS for the 50% doping case [panel (a) of Fig. 2]. The red line is drawn at the Fermi energy.

Moreover, the total magnetic moment per unit cell is an integer multiple of μ_B (namely, 4 μ_B) in all the structures except the 50% doped one, where it drops slightly below the value of 4 μ_B. A noninteger value of μ/μ_B implies that the system cannot be a half metal, as also appearing from spin-projected DOS (Fig. 2), where both the spin-up and spin-down component of the corresponding DOS are nonnegligible at the Fermi energy. In the inset of each panel we display the spin-down component of the DOS, zoomed in the vertical scale.

The 12%, 17%, and 25% DFHs present a gap in the spin-down projected DOS, which is zero at the Fermi energy. At variance, the spin-up DOS of all these DFHs is clearly nonzero at the Fermi energy. Hence, the electron population at the Fermi energy in the 12%, 17%, and 25% DFHs is fully spin-up polarized, and these systems are half metals, similarly to the case of uniformly Mn-doped GaAs compounds [1].

In view of the qualitative difference of the 50% doped system, in the following discussion and in optical property calculations only materials with integer μ/μ_B will be considered, and compared with the uniformly doped systems.

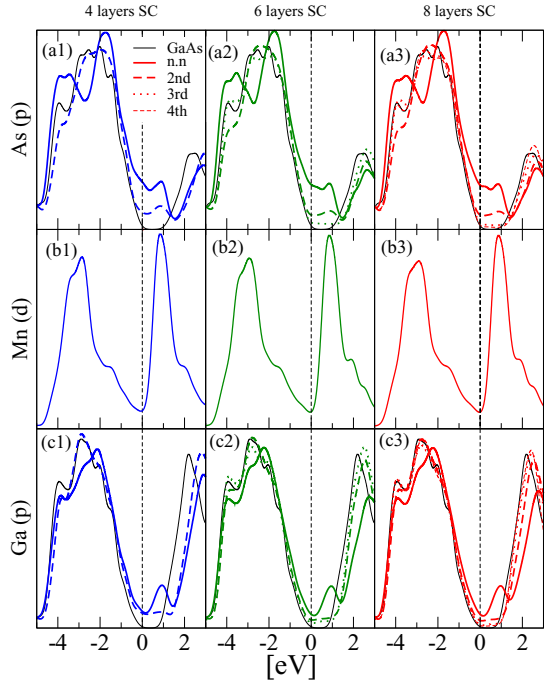

FIG. 5. (Color online) Projected density of states of the studied MnGaAs heterostructures. The projections on As p orbitals [panels (a1)–(a3)], Mn d orbitals [panels (b1)–(b3)], and Ga p orbitals [panels (c1)–(c3)] are shown for the structures with 3 (blue), 5 (green), and 7 (red) GaAs layers between the Mn layers, respectively. The projection on As and Ga species is atom resolved. Atoms are selected according to their distance from the Mn layer, as 1st nearest neighbor (thick continuous line), 2nd (thick dashed line), 3rd (dotted line), and 4th (thin dashed line). The case of bulk GaAs is also shown for comparison (thin continuous black line).

A more detailed analysis of the band character can be performed by decomposing the DOS via a projection on the different atomic species and angular momenta. The major contribution to the metallic bands comes from Mn d orbitals and As and Ga p orbitals. Figure 5 shows the As p (top panel), Mn d (middle panel), and Ga p (bottom panel) contribution for the three systems considered (i.e., three-, five-, and seven-layer supercell). The As and Ga p contribution to the undoped GaAs DOS is also shown for comparison (black line). The p As and Ga contributions are also decomposed according to the distance of the considered atom from the Mn layer, with the thick continuous line corresponding to the As (Ga) nearest to Mn. As shown in Fig. 5, the presence of Mn mainly affects the first two closest layers of As (labeled with 1 and 2 in Fig. 1, thick continuous and dashed lines in Fig. 5) and the first closest layer of Ga (same conventions). They all display a peak above the Fermi energy at the same energy of the d orbital of Mn. These peaks indicate a hybridization of d orbitals of Mn with p orbitals of the As and Ga atoms, or better with the sp^3 backbone of the GaAs lattice. Indeed the Mn atoms, replacing Ga atoms, are "forced" to create an sp^3 hybridization. However, while Ga has three electrons in the s plus p orbitals, Mn only has two. There is then a competition between filling the hole in the sp^3 backbone and keeping five valence Mn electrons in its d orbitals. This competition is represented as two resonant configurations in Fig. 6. The dashed red arrow indicates the electron shared between sp^3 and d orbitals. In both configurations the magnetic moment is $4\mu_B$/cell.

The remaining As and Ga atoms show a PDOS contribution very similar to the one in bulk GaAs, confirming that they are not substantially influenced by the presence of the Mn dopant. This result confirms that the ferromagnetic interaction between the Mn layers becomes much weaker if they are separated by more than 3 GaAs layers. However also at greater distance a small projection of the state immediately above the Fermi level remains on the As and Ga orbitals, suggesting that a smaller ferromagnetic interaction is still present also in the 12% doped system, where the Mn layers are separated by 7 GaAs layers.

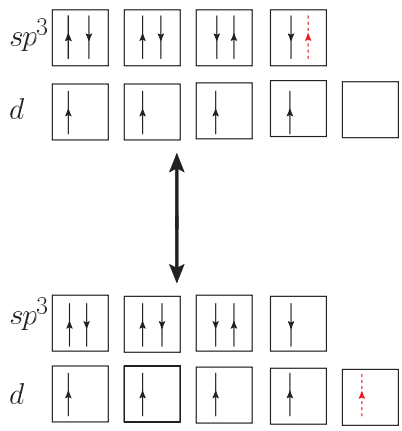

FIG. 6. (Color online) Schematic electronic diagram for the As-Mn binding represented as two resonant configurations. Each Mn orbital has four first-nearest-neighbor As atoms. In a first approximation, a hole is shared between the four Mn-As sp^3 bond orbitals and the Mn d orbitals. In practice the hole delocalizes also on the other sp^3 orbitals of the doped GaAs and is responsible of the ferromagnetic interaction between different Mn layers.

III. OPTICAL PROPERTIES OF Mn-DOPED GaAs

Optical absorption is proportional to the imaginary part of the macroscopic dielectric function, $\epsilon_M(\omega)$. The latter can be obtained from microscopic quantities such as the response function $\chi_{G,G'}(\boldsymbol{q},\omega)$ [12,21]. Response functions can in turn be computed on the basis of transition matrix elements between electronic states (both interband and intraband in the case of metals). Several levels of theory can be adopted, ranging from the simplest approach, i.e., the bare independent particle–random phase approximation (IP-RPA), to more complete approaches where, e.g., local fields and/or excitonic effects are taken into account. In the long-wavelength limit, which is appropriate for UV-VIS spectra, ϵ_M can be expressed as

$$\epsilon_M(\omega) = 1 - \lim_{\boldsymbol{q}\to 0} \frac{4\pi e^2}{|\boldsymbol{q}|^2} \chi(\boldsymbol{q},\omega), \tag{1}$$

involving only the $G = 0$, $G' = 0$ "head" of the *appropriate* response function $\chi_{G,G'}(\boldsymbol{q},\omega)$ written in reciprocal space [12].

In this work, we use $\chi^{\mathrm{RPA}}_{\boldsymbol{GG'}}(\boldsymbol{q},\omega)$, i.e., the response function constructed including the local-field (LF) effects:

$$\chi^{\mathrm{RPA}}_{\boldsymbol{GG'}}(\boldsymbol{q},\omega) = \chi^{\mathrm{QP}}_{\boldsymbol{GG'}}(\boldsymbol{q},\omega) + \sum_{\boldsymbol{G}_1\boldsymbol{G}_2} \chi^{\mathrm{QP}}_{\boldsymbol{GG}_1}(\boldsymbol{q},\omega) f^H_{\boldsymbol{G}_1\boldsymbol{G}_2}(\boldsymbol{q},\omega) \chi^{\mathrm{RPA}}_{\boldsymbol{G}_2\boldsymbol{G'}}(\boldsymbol{q},\omega). \tag{2}$$

Here $f^H_{\boldsymbol{G}_1\boldsymbol{G}_2}(\boldsymbol{q}\omega) = \delta v_H[\rho]/\delta\rho$, the functional derivative of the Hartree potential, is the bare Coulomb interaction and corresponds to an electron-hole exchange term [12]. Neglecting f^H one has $\chi_{GG'}(\boldsymbol{q},\omega) = [\chi^{\mathrm{QP}}_0]_{GG'}(\boldsymbol{q},\omega)$, i.e., the response function in the IP-RPA approximation.

The quasiparticle (QP) response function an be expressed in terms of single-particle electronic eigenstates $|\psi^{\mathrm{QP}}_{n\boldsymbol{k}}\rangle$ and eigenenergies $\epsilon^{\mathrm{QP}}_{n\boldsymbol{k}}$ as

$$\chi^{\mathrm{QP}}_{\boldsymbol{GG'}}(\boldsymbol{q},\omega) = -\frac{1}{V}\sum_{n\boldsymbol{k}}\sum_{m\boldsymbol{k'}}(f_{n\boldsymbol{k}} - f_{m\boldsymbol{k'}}) \times \left(\frac{\langle\psi^{\mathrm{QP}}_{m\boldsymbol{k'}}|e^{i(\boldsymbol{q}+\boldsymbol{G})\boldsymbol{r}}|\psi^{\mathrm{QP}}_{n\boldsymbol{k}}\rangle\langle\psi^{\mathrm{QP}}_{n\boldsymbol{k}}|e^{-i(\boldsymbol{q}+\boldsymbol{G'})\boldsymbol{r'}}|\psi^{\mathrm{QP}}_{m\boldsymbol{k'}}\rangle}{\epsilon^{\mathrm{QP}}_{m\boldsymbol{k'}} - \epsilon^{\mathrm{QP}}_{n\boldsymbol{k}} - \omega - i\eta}\right). \tag{3}$$

ϵ^{QP} are obtained from KS eigenvalues applying a gap-opening/band-stretching correction which simulates the self-energy effects in semiconductors/metals, and $|\psi^{\mathrm{QP}}_{n\boldsymbol{k}}\rangle$ are taken as unperturbed KS eigenstates $|\psi^{\mathrm{KS}}_{n\boldsymbol{k}}\rangle$, as implemented in the YAMBO [22] code.

Here we report the optical properties of our four-, six-, and eight-layer SCs of Mn-doped GaAs. The absorption spectra of the undoped system is also shown for reference as for the case of the DOS. To obtain converged spectra a k-points sampling of

the BZ with a $24 \times 24 \times n$ mesh is used, with $n = 8,6,4$ for the four, six, and eight layers, respectively, considering nv valence bands and nc conduction bands in total. The Drude term is modeled with a plasma frequency $\omega_p = 2.75$ eV and relaxation frequency of 0.7 eV and the QP corrections are included as a 10% stretching of the band structure, as in Ref. [10]. LF effects are found to converge including $\boldsymbol{G}$ vectors in Eq. (2) up to a kinetic energy cutoff of 4 Ry. The absorption of bulk GaAs is instead computed with a double-grid sampling of the BZ [23] with a regular $12 \times 12 \times 12$ mesh shifted from Γ plus a random mesh of 2000 k points. In this case the well-established value [24] of 0.8 eV opening of the band gap has been used for the QP correction.

In Figs. 7 and 8 the absorption spectra, Im[$\epsilon_M(\omega)$], for the 12%, 17%, and 25% doped materials are shown. The case of bulk (undoped) GaAs is in panel (a) of both figures. Dashed lines show the IP-RPA spectra for comparison. The RPA spectra including LF effects differ from IP-RPA ones because the intensity of the absorption is reduced. The intensity reduction is peak specific, and is due to the well-known depolarization effect, which is usually more important in nonuniform systems. However, LF do not change substantially the position of the peaks.

We first consider incident light with polarization on the layers plane (Fig. 7). The intensity of the main E2 peak around 5 eV is lower in DFHs than in bulk GaAs, and it decreases by increasing the Mn concentration. In fact this peak becomes

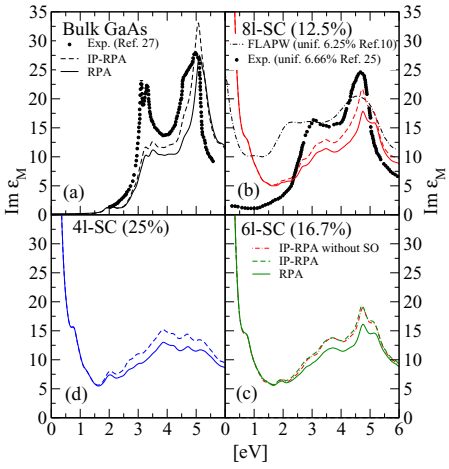

FIG. 7. (Color online) Computed UV-VIS absorption spectra for light polarization parallel to the Mn layers. Panel (a) shows the bulk GaAs case as reference, and Mn δ-doped heterostructures with 12.5%, 16.7%, and 25% Mn concentration are shown in panels (b), (c), and (d), respectively. The dashed lines and continuous lines represent the IP-RPA and RPA results, respectively. Theoretical spectra are compared with experimental data for bulk GaAs (circles in panel (a), from Ref. [27]) and for a uniformly Mn-doped GaAs sample at low doping concentrations (dots in panel (b), from Ref. [25]). We also compare with the FLAPW *ab initio* results of Ref. [10], computed for a uniformly doped system with a concentration of 6.25% (dot-dashed line).

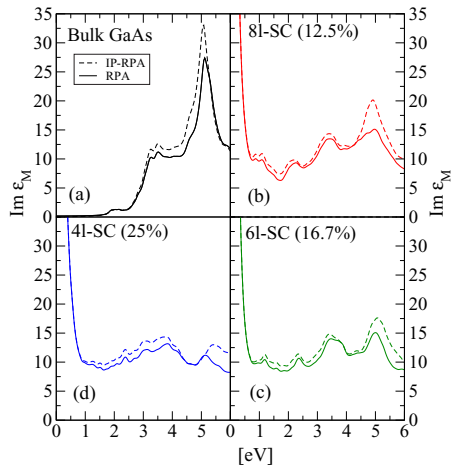

FIG. 8. (Color online) Computed UV-VIS absorption spectra of bulk GaAs [panel (a)] and Mn δ-doped heterostructures with 12.5% [panel (b)], 16.7% [panel (c)], and 25% [panel (d)] Mn doping, for light polarization perpendicular to the Mn layers (grazing incidence). As in Fig. 7, the dashed lines and continuous lines represent IP-RPA and RPA results, respectively.

a double peak by effect of the Mn δ doping [panel (b)], and more structures appear by decreasing the distance between Mn layers [panels (b), (c), and (d)]. We compare in panel (b) our IP-RPA results for the 12% δ-doped systems (seven layers of Ga between the Mn layers) with experimental data [circles in panel (b)] for a uniformly doped $Ga_{1-x}Mn_xAs$ sample with $x = 0.066$ (Ref. [25]). The theoretical underestimation of the intensity of the 5 eV (E2) peak is likely due to the different doping concentration between theory and experiment. Indeed the intensity of the E2 peak decreases increasing the dopant concentration, both experimentally (Refs. [25,26]) and theoretically (present work, and Ref. [10]). We notice that the double-peak structure at ∼5 eV of Fig. 7 is peculiar to the δ-doped GaAs absorption spectra in polar geometry, since it is absent in the computed spectra with light polarization perpendicular to the Mn layer (Fig. 8), as well as in the experimental data for randomly distributed Mn doping. The double peak also appears when the absorption spectra are computed without SO as shown in Fig. 7(c2).

The influence of local field effects in the case of grazing incidence (Fig. 8) is more pronounced for energies above 5 eV, where LFs appear to suppress the peak intensity more than at lower energies. On the other hand, in both Figs. 7 and 8 the intensity of the theoretical ∼3 eV is underestimated, due to our neglect of excitonic effects [24,27]. The latter, however, are expected to be strongly suppressed in systems with efficient free-carrier screening, such as in metals or even half metals, with respect to the case of a pure semiconductor. In fact the peak at 3 eV in the experimental data for uniform Mn doping [dots in panel (b) of Fig. 7] is clearly less prominent than in bulk GaAs.

The overestimation of ϵ_M at very low energy in our simulation can be attributed, at least in part, to an overestimation of intraband transitions, described by the Drude term. The

discrepancies between experimental data and our results can also be partially accounted for by the different types of doping (uniform vs δ-doping).

Moreover experiments are performed at diluted Mn concentration (a few percent or less). When the concentration of Mn in uniformly doped samples is sufficiently low, the overlap of impurity wave functions is negligible and the compound is semiconducting. At variance, in δ-doped samples, the conductivity in the Mn layers remains metallic also at overall low doping concentrations.

A. Kerr effect and reflection magneto-optical dichroism

MOKE experiments evaluate the difference in optical reflectivity for left and right circularly polarized light. In practice, since a linearly polarized light can be thought of as the result of the superposition of left and right circularly polarized waves having the same intensity and phase, a nonzero difference in the dielectric response of the material can be detected as a change in the polarization properties of the reflected light.

In this way, Kerr parameters are defined in terms of the Kerr rotation θ_K and the Kerr ellipticity η_K, the first describing the angle between the major axis of the ellipse with respect to the original linear polarization direction, and the second one being related to the ratio between the two ellipse axis.

In the present paper we consider the MOKE in the so-called polar geometry, where the light propagates along the direction of the magnetization of the sample, which we identify here as z, perpendicular to the sample surface. The polarization hence lies in the xy plane. We now introduce the complex refractive index $n_\pm = \sqrt{\epsilon_\pm}$, where ϵ_+ (ϵ_-) is the dielectric function for the right (left) circularly polarized light. Then following Ref. [6] the Kerr parameters are defined as

$$\theta_K(\omega) + i\eta_K(\omega) = i\frac{n_+(\omega) - n_-(\omega)}{n_+(\omega)n_-(\omega) - 1}. \tag{4}$$

$\epsilon_\pm$ can be derived, for a cubic system, from the xx and xy elements of the dielectric tensor, according to the expression $\epsilon_\pm = \epsilon_{xx} \pm i\epsilon_{xy}$. The magneto-optical response can hence be computed starting from the diagonal and off-diagonal components of the dielectric tensor. Indeed, if $\epsilon_{xy} \ll \epsilon_{xx}$, which is the common case, Eq. (4) is well approximated by

$$\theta_K(\omega) + i\eta_K(\omega) \simeq \frac{-\epsilon_{xy}(\omega)}{[\epsilon_{xx}(\omega) - 1]\sqrt{\epsilon_{xx}(\omega)}}, \tag{5}$$

which holds for small Kerr angles.

Remarkably, in such differential measurements, the contribution stemming from the off-diagonal elements of the dielectric tensor, which is usually negligible in bare absorption or reflectivity experiments, becomes important. ϵ_{xy} can be obtained from the response function $\chi(\boldsymbol{q}_\alpha \boldsymbol{q}_\beta \omega)$, by generalizing Eq. (1). In practice, we evaluate the dielectric tensor by means of the YAMBO [22] code, using the same approach described in Ref. [13], where $\epsilon_{\alpha\beta}$ is computed, at the RPA-IP level, as

$$\epsilon_{M\alpha\beta}(\omega) = \mathbf{1} - \lim_{\substack{\boldsymbol{q}_\beta \to 0 \\ \boldsymbol{q}_\alpha \to 0}} \frac{4\pi e^2}{q^2} \chi(\boldsymbol{q}_\alpha \boldsymbol{q}_\beta \omega). \tag{6}$$

ϵ_{xy} must be converged against the same parameters needed to converge the absorption. Convergence in the sampling of the BZ requires a $24 \times 24 \times n$ grid where the number of k points along the z direction are $n = 12,8,6$ for the 4-, 6-, and 8-layer supercell, respectively, i.e., a slightly finer sampling along the z direction, if compared to the one used for absorption. The reason stems from the fact that ϵ_{xy} is two orders of magnitude smaller than ϵ_{xx}. The knowledge of $\epsilon_{\alpha\beta}$ also allows one to compute the reflectance $R_\pm(\omega)$ at normal incidence, defined as the square modulus of the complex reflectivity, both for right (+) and left (−) circularly polarized light [6]:

$$R_\pm = \left\| \frac{n_\pm(\omega) - 1}{n_\pm(\omega) + 1} \right\|^2. \tag{7}$$

Following Ref. [6], the latter quantities determine the reflectance magnetic circular dichroism (R-MCD) spectrum as

$$R_{\mathrm{MCD}}(\omega) = \frac{1}{2}\frac{R_+ - R_-}{R_+ + R_-}, \tag{8}$$

which is more easily measured experimentally than the MOKE parameters. In the limit of small Kerr angles one can prove, after some tedious but straightfoward algebra, that $R_{\mathrm{MCD}}(\omega)$ and Kerr ellipticity are brought to coincide:

$$R_{\mathrm{MCD}}(\omega) \approx \eta_K(\omega). \tag{9}$$

In Fig. 9 we plot the computed Kerr parameters θ_K and η_K for the considered DFHs. We also show, by comparison, some theoretical and experimental literature data for uniformly doped MnGaAs.

We first observe that there is no clear dependence of the computed Kerr parameters on the Mn-doping concentration. This finding is in agreement with previous calculations for the uniform-doping case [9,10]. Our calculations show that, as it happens for the absorption, the computed MOKE is similar to the one obtained for the uniformly doped case. In Fig. 9 (bottom panels) the Kerr rotation is compared with all-electron calculations for the uniform system at the LDA level [10]. Despite this difference in the calculations, different structures (uniform doping and DFH), and different doping concentrations, all calculations and experimental data show at least one common dominant feature, that is, a negative Kerr rotation at low energy. In the experimental data for uniform doping [28,29] this negative peak in the Kerr rotation is blueshifted by ≈0.6 eV with respect to our results (see Fig. 9, top left panel). This shift also appears in the computed Kerr ellipticity/R-MCD data (top right panel) and in DFT calculations for the uniform-doping case. It maybe due to inadequacy of the 10% band stretching approach to mimic QP corrections, in particular for the Mn d empty states. The latter, being only 1 eV above the Fermi level, are essentially unaffected by the stretching approach.

We can thus conclude that at least the first peak in the Kerr rotation remains substantially unchanged for doping concentrations varying from 12.5% to 25%, and it is barely affected by the details of the geometrical distribution of the Mn atoms.

As it appears from Eq. (5), a peak in the Kerr rotation can either have an "optical" origin, i.e., it stems from a vanishing value of the denominator, or a "magneto-optical" one, i.e., it

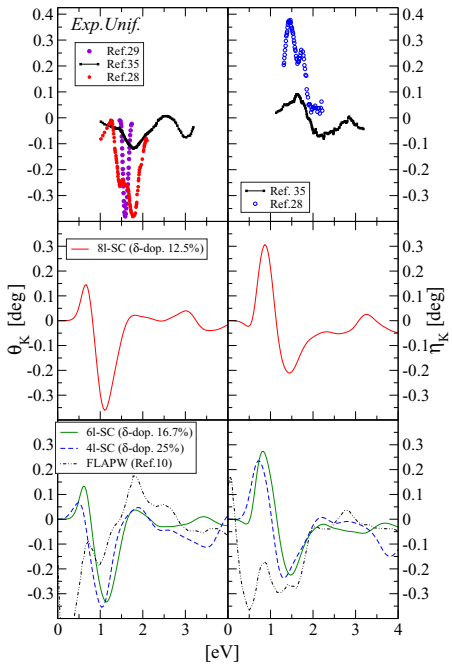

FIG. 9. (Color online) Kerr parameters computed at the IP-RPA level for three Mn δ-doped GaAs heterostructures. Central panels show the spectrum of the 12.5% Mn DFH (red line); the results for the 16.7% and 25% Mn concentrations are shown in bottom panels (green and dashed blue lines, respectively). In the top panel, we show, for comparison, several experimental data for uniformly doped samples: black dots are for a 6% Mn sample considered in Ref. [35], the red dots are for a 3% Mn case (Ref. [28]), and violet dots refer to a 2% Mn sample (Ref. [29]). Finally blue empty dots in right top panel are experimental data for the reflection MCD in a uniformly doped sample with 3% Mn from Ref. [28]. In bottom panels, we report as dashed lines the results of FLAPW (LDA + stretched bands) calculations for a uniformly doped system, from Ref. [10].

arises from maximum/minimum of $\epsilon_{xy}(\omega)$ in the numerator. For the uniformly doped system the minimum close to 1 eV has been reported to be of "optical" origin [9,10].

To analyze whether this is the case also for the DFH, we plot in Fig. 10 the diagonal and the off-diagonal dielectric function. We clearly see that Im[ϵ_{xy}] has a maximum at 1 eV and also that both Re[ϵ_{xx}] and Im[ϵ_{xx}] are small in the same region. So the corresponding peaks of the Kerr rotation, in the present case, have both optical and magneto-optical origin.

Comparing the computed Kerr parameters with the computed DOS and its projections (see Figs. 2–5), we see that a key role is likely played by the empty state induced by the Mn doping, as discussed in Sec. II (see also Fig. 6). Indeed we note that this state is located about 1 eV above the Fermi level. Thus the maximum (in absolute value) of the rotation is likely due to transitions from the valence band to this state, i.e., it is due to a transition involving both d and sp^3 states.

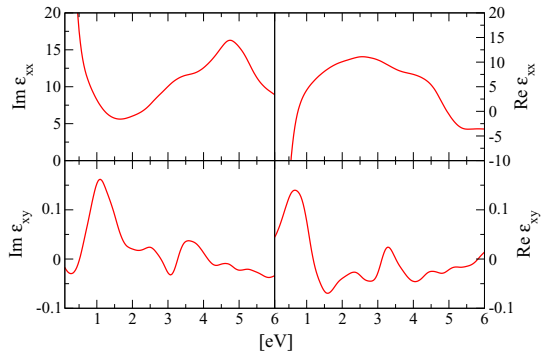

FIG. 10. (Color online) Real and imaginary part of the diagonal and off-diagonal components of ϵ for the Mn δ-doped GaAs heterostructure corresponding to a 12.5% doping (Ref. [28]).

We thus suggest that in DFHs the MOKE could be substantially affected by electron/hole doping. Indeed, varying the hole concentration, the semimetallic character of the system can be substantially affected, leading to a very different absorption spectra, in particular in the region close to or below 1 eV as already suggested for the uniformly doped system [30]. This conclusion is also supported by previous all-electron results for the uniform-doping case, where the Kerr spectrum is shown to change significantly when As antisite defects are considered together with Mn doping [9].

B. Faraday effect and transmission magneto-optical dichroism

While the Kerr effect and reflection MCD imply measuring the light reflected by a magnetic material, the corresponding effect for light transmitted through a magnetic medium is known as the Faraday effect. In polar geometry (the one considered in the present study), when a linear polarized light propagates parallel to the magnetization of a ferromagnet, a Faraday rotation is observed as a rotation of the polarization plane of the transmitted light (θ_F). In terms of circularly polarized reflective indexes, the Faraday rotation θ_F and the Faraday ellipticity η_F read [6]

$$\theta_F(\omega) + i\eta_F(\omega) = i\frac{\omega}{2c}[n_+(\omega) - n_-(\omega)]L, \qquad (10)$$

where L is the sample thickness and c the speed of light. We evaluated the Faraday parameters per unit length for the Mn δ-doped GaAs in a similar way as done for Kerr parameters; our results are displayed in Fig. 11. As the Kerr parameters are related to the R-MCD, the Faraday parameters are related to the transmission MCD [31] (T-MCD):

$$T_{\mathrm{MCD}}(\omega) = \frac{T_+ - T_-}{T_+ + T_-}, \qquad (11)$$

which, at normal incidence, is proportional to $\Delta\alpha(\omega)$, i.e., the difference of the absorption coefficient $\alpha_\pm(\omega) = 2\omega\mathrm{Im}[n_\pm(\omega)]/c$ between the right and the left circularly polarized light:

$$\Delta\alpha(\omega) = \alpha_+(\omega) - \alpha_-(\omega) = -\frac{4\eta_F(\omega)}{L}. \qquad (12)$$

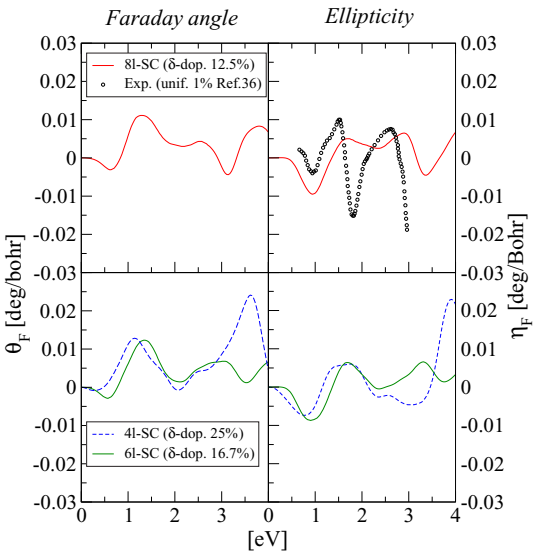

FIG. 11. (Color online) Faraday parameters/transmission MCD computed at the IP-RPA level for three Mn δ-doped GaAs heterostructures, corresponding to 12.5%, 16.7%, and 25% Mn concentrations. Black empty dots are experimental data for uniformly doped samples with 1% Mn, from Ref. [36].

Thus we can compare the results of our simulations with T-MCD experimental data for diluted concentration [32] in randomly Mn-doped GaAs.

The first thing that we observe is that, despite that the physics of the Faraday effect and T-MCD is very similar to that of the Kerr effect and R-MCD, in this case the results are slightly more sensitive to the doping concentration. At least the region above 2 eV is affected going from 12.5% to 25% doping. However, as in the case of the Kerr effect, there is a structure slightly above 1 eV which is substantially unchanged varying the doping concentration.

To investigate possible applications of DFHs as Faraday rotators, in the following we compare some of our computed optical and magneto-optical data with the corresponding quantities of bulk transition metals, which are typical textbook examples for the Faraday effect [33].

We consider the 4-layer DFH and the peak at $\approx$1 eV: according to our simulation, the Faraday rotation is $\theta_F \simeq 60^\circ\ \mu\mathrm{m}^{-1}$, significantly larger than the typical values for Fe, Co, and Ni (35°, 36°, $10^\circ\ \mu\mathrm{m}^{-1}$, respectively) [33] (taking into account the 0.6 eV redshift of our computed spectra with respect to the experimental ones, these values are taken at $\lambda = 820$ nm, i.e., at about 1.5 eV). On the other hand, DFHs have a lower optical absorption coefficient, which is desirable for efficient transmission. The optical penetration depth, defined as the length over which an electromagnetic wave of given frequency encounters a $1/e$ reduction of its intensity—proportional to the inverse of the absorption coefficient—is about 36 nm for our 4-layer DFH. For comparison, the optical penetration depth of transition metals is of the order of 15 nm.

IV. CONCLUSIONS

In conclusion, our results for Mn δ-doped GaAs show that such digital ferromagnetic heterostructures have optical absorption and magneto-optical spectra displaying both similarities and differences with respect to previously studied uniformly doped MnGaAs systems. The 50% Mn doping case (one layer of GaAs between MnAs layers) corresponds to a system with qualitatively different properties, having lost the half-metallicity. All other structures, corresponding to 12%–25% Mn doping, have optical absorption spectra which change gradually with the Mn concentration. The resulting spectra compare well with the available experimental data for the low-doping ($\leqslant$12%) system and theoretical data for the higher doping (25%), for the uniformly doped case. With increasing Mn concentration the typical bulk GaAs spectral shape becomes less and less structured. In agreement with the experimental findings the peak at $\simeq$3 eV is strongly suppressed, likely because of the hole doping induced by the Mn impurities, which screens the electron-hole interaction responsible for the creation of the excitonic peak. The peak at $\simeq$5 eV is instead less affected.

Although the absorption spectra of the δ-doped materials share the essential features of those of uniformly Mn-doped GaAs at similar concentrations, the effect of local fields is enhanced, due to the stronger nonuniformity of the δ-doped system. This effect is particularly evident when the light polarization has a large component along the growth direction, while it is less important when the polarization lays in the plane of the Mn layers. MOKE spectra do not show a clear trend with the doping concentration: essentially, the maximum value of Kerr rotation is constant, and quite similar to that of the uniformly doped material [9,10]. Although the Faraday ellipticity is more sensitive to the doping concentration, also in this case the low-energy spectrum remains substantially unchanged moving from the high-doping case (25%) to lower doping. On the other hand, the important role of the hole shared between the Mn d and GaAs sp^3 states suggests that the studied DFHs could be very sensitive to a further doping with electrons.

ACKNOWLEDGMENTS

We acknowledge the CINECA and the Regione Lombardia award under the LISA initiative, for the availability of high-performance computing resources and support, the Fondazione Cariplo (Italy) for funding (Grant No. 2009-2552) within the project OSEA (Oxides for Spin Electronic Applications), and R. Colnaghi for technical support. One of us (G.O.) acknowledges the ETSF-Italy [34] for support.

[1] K. Sato, L. Bergqvist, J. Kudrnovský, P. H. Dederichs, O. Eriksson, I. Turek, B. Sanyal, G. Bouzerar, H. Katayama-Yoshida, V. A. Dinh, T. Fukushima, H. Kizaki, and R. Zeller, Rev. Mod. Phys. **82**, 1633 (2010).

[2] A. M. Nazmul, T. Amemiya, Y. Shuto, S. Sugahara, and M. Tanaka, Phys. Rev. Lett. **95**, 017201 (2005).
[3] X. Chen, M. Na, M. Cheon, S. Wang, H. Luo, B. D. McCombe, X. Liu, Y. Sasaki, T. Wojtowicz, J. K. Furdyna, S. J. Potashnik, and P. Schiffer, Appl. Phys. Lett. **81**, 511 (2002).
[4] S. A. Wolf, D. D. Awschalom, R. A. Buhrman, J. M. Daughton, S. von Molnr, M. L. Roukes, A. Y. Chtchelkanova, and D. M. Treger, Science **294**, 1488 (2001).
[5] B. Behin-Aein, D. Datta, S. Salahuddin, and S. Datta, Nat. Nanotechnol. **5**, 266 (2010).
[6] See, e.g., K. Shinagawa, in *Magneto-Optics*, edited by S. Sugano and N. Kojima, Springer Series in Solid State Sciences, Vol. 128 (Springer-Verlag, Heidelberg, 2000).
[7] R. K. Kawakami, E. Johnston-Halperin, L. F. Chen, M. Hanson, N. Guébels, J. S. Speck, A. C. Gossard, and D. D. Awschalom, Appl. Phys. Lett. **77**, 2379 (2000).
[8] K. S. Burch, E. J. Singley, J. Stephens, R. K. Kawakami, D. D. Awschalom, and D. N. Basov, Phys. Rev. B **71**, 125340 (2005).
[9] S. Picozzi, A. Continenza, M. Kim, and A. J. Freeman, Phys. Rev. B **73**, 235207 (2006).
[10] A. Stroppa, S. Picozzi, A. Continenza, M. Y. Kim, and A. J. Freeman, Phys. Rev. B **77**, 035208 (2008).
[11] M. Ogura and H. Akai, Phys. Rev. B **82**, 184426 (2010).
[12] G. Onida, L. Reining, and A. Rubio, Rev. Mod. Phys. **74**, 601 (2002).
[13] D. Sangalli, A. Marini, and A. Debernardi, Phys. Rev. B **86**, 125139 (2012).
[14] P. Hohenberg and W. Kohn, Phys. Rev. **136**, B864 (1964).
[15] W. Kohn and L. J. Sham, Phys. Rev. **140**, A1133 (1965).
[16] J. P. Perdew and A. Zunger, Phys. Rev. B **23**, 5048 (1981).
[17] P. Giannozzi, S. Baroni, N. Bonini, M. Calandra, R. Car, C. Cavazzoni, D. Ceresoli, G. L. Chiarotti, M. Cococcioni, I. Dabo, A. Dal Corso, S. Fabris, G. Fratesi, S. de Gironcoli, R. Gebauer, U. Gerstmann, C. Gougoussis, A. Kokalj, M. Lazzeri, L. Martin-Samos, N. Marzari, F. Mauri, R. Mazzarello, S. Paolini, A. Pasquarello, L. Paulatto, C. Sbraccia, S. Scandolo, G. Sclauzero, A. P. Seitsonen, A. Smogunov, P. Umari, and R. M. Wentzcovitch, J. Phys.: Condens. Matter **21**, 395502 (2009).
[18] The total residual force is below 1.7 mRy/bohr.
[19] H. J. Monkhorst and J. D. Pack, Phys. Rev. B **13**, 5188 (1976).
[20] The density of states has been computed projecting the wave functions either on the $+S_z$ or the $-S_z$ spin channel. In this way we have been able extract the spin-resolved DOS from our calculations.
[21] G. Strinati, Riv. Nuovo Cimento Soc. Ital. Fis. **11**, 1 (1988).
[22] A. Marini, C. Hogan, M. Grüning, and D. Varsano, Comput. Phys. Commun. **180**, 1392 (2009).
[23] D. Kammerlander, S. Botti, M. A. L. Marques, A. Marini, and C. Attaccalite, Phys. Rev. B **86**, 125203 (2012).
[24] L. X. Benedict, E. L. Shirley, and R. B. Bohn, Phys. Rev. B **57**, R9385 (1998); G. Adragna, R. Del Sole, and A. Marini, *ibid.* **68**, 165108 (2003).
[25] E. J. Singley, R. Kawakami, D. D. Awschalom, and D. N. Basov, Phys. Rev. Lett. **89**, 097203 (2002); E. J. Singley, K. S. Burch, R. Kawakami, J. Stephens, D. D. Awschalom, and D. N. Basov, Phys. Rev. B **68**, 165204 (2003).
[26] K. S. Burch, J. Stephens, R. K. Kawakami, D. D. Awschalom, and D. N. Basov, Phys. Rev. B **70**, 205208 (2004).
[27] D. E. Aspnes and A. A. Studna, Phys. Rev. B **27**, 985 (1983).
[28] R. Lang, A. Winter, H. Pascher, H. Krenn, X. Liu, and J. K. Furdyna, Phys. Rev. B **72**, 024430 (2005).
[29] A. V. Kimel, G. V. Astakhov, A. Kirilyuk, G. M. Schott, G. Karczewski, W. Ossau, G. Schmidt, L. W. Molenkamp, and Th. Rasing, Phys. Rev. Lett. **94**, 227203 (2005).
[30] E. M. Hankiewicz, T. Jungwirth, T. Dietl, C. Timm, and J. Sinova, Phys. Rev. B **70**, 245211 (2004).
[31] M. Berciu, R. Chakarvorty, Y. Y. Zhou, M. T. Alam, K. Traudt, R. Jakiela, A. Barcz, T. Wojtowicz, X. Liu, J. K. Furdyna, and M. Dobrowolska, Phys. Rev. Lett. **102**, 247202 (2009).
[32] K. Ando, T. Hayashi, M. Tanaka, and A. Twardowski, J. Appl. Phys. **83**, 6548 (1998).
[33] See, e.g., J. M. D. Coey, *Magnetism and Magnetic Materials* (Cambridge University Press, Cambridge, 2010).
[34] A. Matsuura, N. Thrupp, X. Gonze, Y. Pouillon, G. Bruant, and G. Onida, Comput. Sci. Eng. **14**, 22 (2012).
[35] E. Kojima, R. Shimano, Y. Hashimoto, S. Katsumoto, Y. Iye, and M. Kuwata-Gonokami, Phys. Rev. B **68**, 193203 (2003).
[36] K. Ando, H. Saito, K. C. Agarwal, M. C. Debnath, and V. Zayets, Phys. Rev. Lett. **100**, 067204 (2008).

Journal of the European Ceramic Society 36 (2016) 1679–1690

Contents lists available at www.sciencedirect.com

Journal of the European Ceramic Society

journal homepage: www.elsevier.com/locate/jeurceramsoc

High temperature stability of $Ba_{0.5}Sr_{0.5}Co_{0.8}Fe_{0.2}O_{3-\delta}$ and $La_{0.6}Sr_{0.4}Co_{1-y}Fe_yO_{3-\delta}$ oxygen separation perovskite membranes

Mariangela Brisotto[a], Federico Cernuschi[b,*], Francesca Drago[b], Cristina Lenardi[c], Patrizia Rosa[c], Carlo Meneghini[d], Marco Merlini[e], Claudia Rinaldi[b]

[a] Università degli Studi di Brescia, Dipartimento di ingegneria meccanica e industriale, Via Branze 38, 25121 Brescia, Italy
[b] RSE, Ricerca Sistema Energetico, via Rubattino 54, 20134 Milano, Italy
[c] Università degli Studi di Milano, Dipartimento Di Fisica, via Celoria 16, 20133 Milano, Italy
[d] Università di Roma Roma Tre, Via della Vasca Navale 84, 00146 Roma, Italy
[e] Università degli Studi di Milano, Dipartimento Scienze della Terra "Ardito Desio", via Mangiagalli 23, 20133 Milano, Italy

ARTICLE INFO

Article history:
Received 29 June 2015
Received in revised form 19 January 2016
Accepted 21 January 2016
Available online 3 February 2016

Keywords:
Perovskite membrane
Oxygen permeation
Kinetic study
High temperature stability

ABSTRACT

The Barium (BSCF) and Lanthanum (LSCF) strontium cobalt–ferrite, are among the most studied mixed ionic electronic conducting materials having interesting properties as Oxygen Transport Membranes. In this paper the two materials are analysed after long term aging at high temperatures and permeation tests. Several characterisation techniques are used to understand degradation mechanisms. Surface layers were analysed by X-ray photoelectron spectroscopy: LSCF is stable, while on BSCF a thin layer of carbonates forms. Quantitative synchrotron radiation diffraction measurements of hexagonal phase content in aged BSCF allows determining Avrami coefficients at 780, 800 and 820 °C. This process is associated to the enrichment of Fe in the regions of grains near the lamellar hexagonal phase, as WDS maps show. Bulk measurements of X-ray Absorption Near Edge Structure (XANES) and the analysis of the Co2p doublet in XPS spectra confirm a reduction of Co ions oxidation number after long time at intermediate temperatures.

1. Introduction

Among the materials developed as membranes for high temperature oxygen separation (for oxycombustion or coal gasification processes) the nonstoichiometric perovskitic compounds ($ABO_{3-\delta}$) are very promising due to their high permeation [1–3]. In such compounds, oxygen transport is diffusive in the bulk through the cationic vacancies; the cubic structure is the most favourable as the vacancies are randomly distributed in the lattice, increasing the transport properties. This is the case of the strontium cobalt–ferrite, $Sr(Co, Fe)O_{3-\delta}$ (SCF) at high temperature (around 1000 °C), but brownmillerite formation causes structural instability [2,3] in the temperature range 700–900 °C. To overcome such a problem, the partial substitution of Sr (2+) with different anions, such as La (3+) and Ba (2+) is widely studied and under continuous development [3–5]. Lanthanum presence [4–10] generates a charge unbalance, locally compensated by oxygen vacancies formation; the rombohedral structure of $(La, Sr)(Co, Fe)O_{3-\delta}$ (LSCF) compounds at room temperature transforms into the desired cubic structure at a temperature in the range 700–850 °C. On the other side, the partial substitution of Sr with Ba produces cubic $(Ba, Sr)(Co, Fe)O_{3-\delta}$ (BSCF) compounds, with even better permeation properties. Results of permeation tests [11–21] show that among the two mentioned material families the best compositions are $La_{0.6}Sr_{0.4}Co_{0.2}Fe_{0.8}O_{3-\delta}$ (LSCF6428) and $Ba_{0.5}Sr_{0.5}Co_{0.8}Fe_{0.2}O_{3-\delta}$ (BSCF5582) respectively, having interesting permeation properties and acceptable structural stability during heating/cooling between ambient and operating temperatures (800 °C < T < 950 °C). Nevertheless, several studies try to understand more deeply the limits of such compounds [22–33].

The literature reports structural transition in the temperatures range 500 °C–800 °C (BSCF) or 500–600 °C (LSCF) depending on the ratio between Ba and Sr in the membrane. In the case of BSCF5582 the loss of oxygen is mainly caused by a reduction of the cobalt oxidation state compared to the iron site [23]. Just such capability of the Co to get different oxidation numbers is the main

* Corresponding author.
E-mail addresses: mariangiola.brisotto@unibs.it (M. Brisotto), federico.cernuschi@rse-web.it (F. Cernuschi), drago@rse-web.it (F. Drago), cristina.lenardi@mi.infn.it (C. Lenardi), carlo.meneghini@uniroma3.it (C. Meneghini), marco.merlini@unimi.it (M. Merlini), claudiarinaldi.ion@gmail.com (C. Rinaldi).

http://dx.doi.org/10.1016/j.jeurceramsoc.2016.01.029
0955-2219/

cause of the long term stability problems of BSCF5582 related to a reversible transformation (cubic → hexagonal) in the intermediate temperature range (i.e. 700–850 °C) and to kinetic demixing phenomena occurring during permeation at higher temperatures. Several studies tried to clarify the nature of the formation of a secondary hexagonal phase [24–34], but published kinetics data of this transformation are limited to only one temperature [24,32]. Moreover only few data about the decomposition processes of BSCF after long term permeation tests can be found in the literature [21], while some interesting results are present for LSCF [9,10,18–20].

In this paper, a further contribution to the characterisation of these two materials with a multi-methodological approach (physical, crystallographic and spectroscopic), and to the study of their stability in a wider temperature range is provided. In the last part of the paper the analyses performed on some membranes after permeation tests are shown and discussed.

2. Experimental

2.1. Materials

This study was performed on discs (1 mm thick and 14.7 mm in diameter) of LSFC 6482 and BSCF5582 perovskites produced at Forschungzentrum Jülich (FZJ) by uniaxial pressing and sintering up to 1000 °C and 1200 °C for BSCF and LSCF, respectively, as better explained in [18,31].

To study the stability at high temperature and the kinetic of phase transformations, samples were heat treated at three different temperatures (780, 800, and 820 °C) for different times ranging from 72 to 1300 h. Moreover some membranes were tested in a test rig and afterward analysed to evidence structural evolution and clarify degradation mechanisms induced by oxygen permeation between 750 and 950 °C. Membranes were tested in a glass permeation cell (configuration similar to the scheme reported in [31]), where the sealing was ensured thanks to the presence of two gold rings. Permeation tests were performed at atmospheric pressure and high temperature (750–1010 °C) under O_2 partial pressure gradients, by feeding a O_2/N_2 mixture and a sweep gas (He) with a flow rate of 250 N cm^3/min and 50 N cm^3/min, respectively [35].

2.2. Characterisation techniques

The surface morphology of the two materials was examined in a scanning electron microscope (SEM FEG MIRA 3—TESCAN) with X-ray Energy Dispersive Spectroscopy (EDS) microanalysis (Bruker Quantax 200 with XFlash detector). The chemical composition was measured by a Jeol-8000 Superprobe with six spectrometers WDS (Wavelength Dispersive Spectroscopy), using mineral standards. Raman spectroscopy analyses were carried out with a high-resolution Raman microscope (Labram HR-800, Horiba/Jobin-Yvon; exciting source He–Ne laser, $\lambda = 633$ nm, 50 × objective).

Structural and microstructural XRD characterization was performed by an advanced diffractometer (Bruker D8Advance) operating with Cu tube (40 kV and 40 mA). Two-dimensional XRD patterns were acquired using a Rigaku D-Max Rapid Diffractometer (Cu tube—40 kv and 30 mA), equipped with a collimator (300 μm area) and an Image Plate detector. The measurements were carried out in the reflection mode at 20°.

Two synchrotron X-ray diffraction experiments were performed: the first at the ID09A beamline at ESRF synchrotron radiation facility (Grenoble, France) on as received materials (BSCF, LSCF) and laboratory annealed samples; the standard beamline setup for transmission geometry with area detector was used [37], with monochromatic radiation at high energy ($E = 30$ keV; $\lambda = 0.4145$ Å) to minimize absorption. In the second experiment, performed at the MCX beamline of the ELETTRA synchrotron radiation facility (Trieste, Italy), the thermal expansion coefficient (TEC) and the structural evolution up to 1000 °C of both perovskites were monitored, by using the monochromatic radiation ($\lambda = 0.7866$ Å) and the experimental set up described in [36]. The sample is first powdered and then inserted within a quartz capillary inserted into a closed furnace (for accurate temperature control in the range 25–1000 °C) and sealed to a device able to switch from vacuum to air or inert gas (N_2) atmospheres. Diffraction signals are collected by a translating curved (cylindrical) imaging plate detector to assure a constant sample-detector distance and avoid geometrical corrections for intensity. Raw data (pixel vs. intensity) extracted with Fit2D software [37] are converted into an angle/intensity histogram by a preliminary calibration performed with the NIST standard Si powder. Rietveld analysis of converted spectra was performed with GSAS software [38].

TEC was also measured in Ar and in O_2 in the temperature range 30 °C–900 °C (heating rate of 5 °C/min), using a differential dilatometer (Netzsch–Gerätebau GmbH, Mod. 402 ED), measuring differential expansion of the tested sample, compared to an alumina reference sample. Samples were machined as small 12 × 6 × 1 mm rectangles and weighed before and after TEC measurements to verify the stability of the materials in different atmospheres at high temperature.

Photoemission spectra were acquired with ultra-high vacuum (UHV) chamber having a conventional X-ray source (Leybold LHS 10/12 Mg Kα = 1253.6 eV). The system is equipped with a hemispherical electron analyser, (EA11 MCD). The spectra were acquired in constant pass-energy mode: wide spectra with pass energy $Ep = 100$ eV, high resolution spectra at the element edges with pass energy $Ep = 30$ eV. The overall resolution was 0.9 eV. All the spectra are referenced to the Fermi level and the binding energy scale is calibrated via the Au 4f7/2 core level line (84.0 eV) of a clean polycrystalline Au sample. To remove surface contamination, samples were sputtered with Argon ions at the energy of 3.5 keV. No charging effects were observed during measurements, performed on LSCF and BSCF in the as received condition and after permeation tests, nor on BSCF after long term thermal ageing at 780 °C. The line shapes are fitted with mixed singlets obtained by a linear combination of a Gaussian and a Lorentzian profiles sited on a Shirley background using the KolXPD software (reference: KolXPD, software for photoelectron spectroscopy data measurement and processing, Current version: 1.8.0.37, http://www.kolibrik.net/kolxpd/).

X-ray absorption spectra (XAS) measurements in the near edge region (XANES) were carried out at the ELETTRA (Trieste-Italy) XAFS beamline. The Fe-K ($E_{Fe} = 7112$ eV) and Co-K edge ($E_{Co} = 7709$ eV) absorption spectra were collected in transmission geometry at room temperature on BSCF in the as received condition and after 40 days annealing at 800 °C. The energy scale was calibrated using the absorption spectrum of reference foils (Fe or Co) placed after the sample. The experimental data were treated following the standard procedures for background subtraction and edge jump normalization [39].

3. Results

3.1. Crystallography and microstructure of as received materials

The surface morphology of the LSCF discs is characterized by small grains (diameter 1.2 ± 0.07 μm) and closed porosity few micrometers in size, as shown in Fig. 1a and Fig. 1b, respectively. WDS analyses confirm the nominal composition, as summarized in Table 1. Synchrotron XRD measurements show that at room temperature LSCF is Rhombohedral, R-3c, ($a = 5.4789$ Å $c = 13.3215$ Å)

Table 1
LSCF and BSCF chemical composition as estimated by using WDS microprobe.

Element	wt%	Atomic %	Exp. index of chemical formula	Theor. index of the chemical formula
LSCF				
O	21.5 ± 1	59.8	2.99	3−δ
La	36.2 ± 1	11.6	0.58	0.60
Sr	16.9 ± 0.7	8.6	0.43	0.40
Fe	20.0 ± 0.7	15.9	0.80	0.80
Co	5.5 ± 0.2	4.1	0.21	0.20
BSCF				
O	19.5 ± 1	56.4	2.82	3−δ
Ba	32.4 ± 1	11.0	0.55	0.5
Sr	20.9 ± 1	11.1	0.55	0.5
Fe	5.2 ± 0.2	4.3	0.22	0.2
Co	21.9 ± 0.7	17.3	0.86	0.8

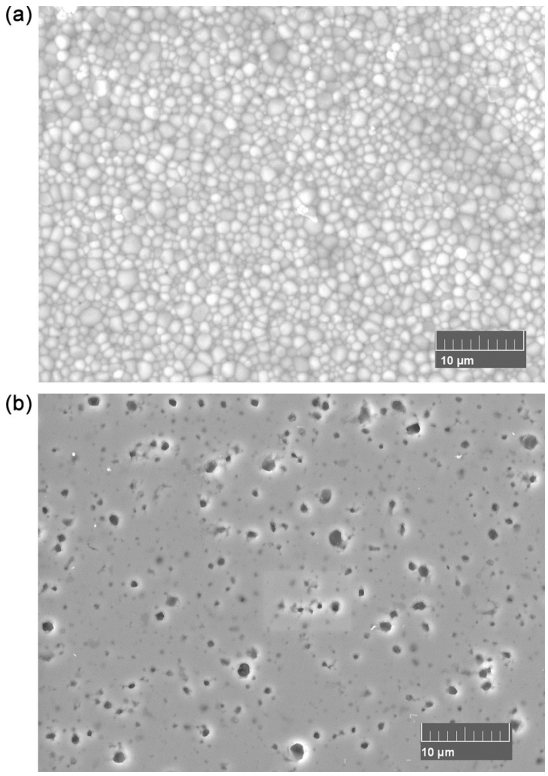

Fig. 1. LSCF secondary electron image of (a) surface and (b) section. The grains morphology and the closed porosity can be clearly observed.

with (La, Sr), (Co, Fe) and O in the (0,0,0.25), (0,0,0) and (0,y,0) position with y = 0.4802, from structural refinement. Increasing the temperature, a modification of the crystal structure was clearly detected. In particular at about 700 °C the LSCF becomes cubic (see details in the following section).

The surface morphology of the BSCF membranes is shown in Fig. 2a; grain and porosity size (Fig. 2b) are about 5 μm and 1 μm, respectively. WDS measurements confirm the nominal composition, as shown in Table 1. The synchrotron XRD results show the cubic structure (a = 3.9740 Å), Pm–3 m with (Ba, Sr), (Co, Fe) and O atoms in the (0,0,0), (0.5,0.5,0.5) and (0.5,0.5,0) position respectively. Surface diffraction measurements indicate also the presence of a small amount of Co oxides. This finding is confirmed by SEM and EDS, which evidence the presence of some Co rich particles

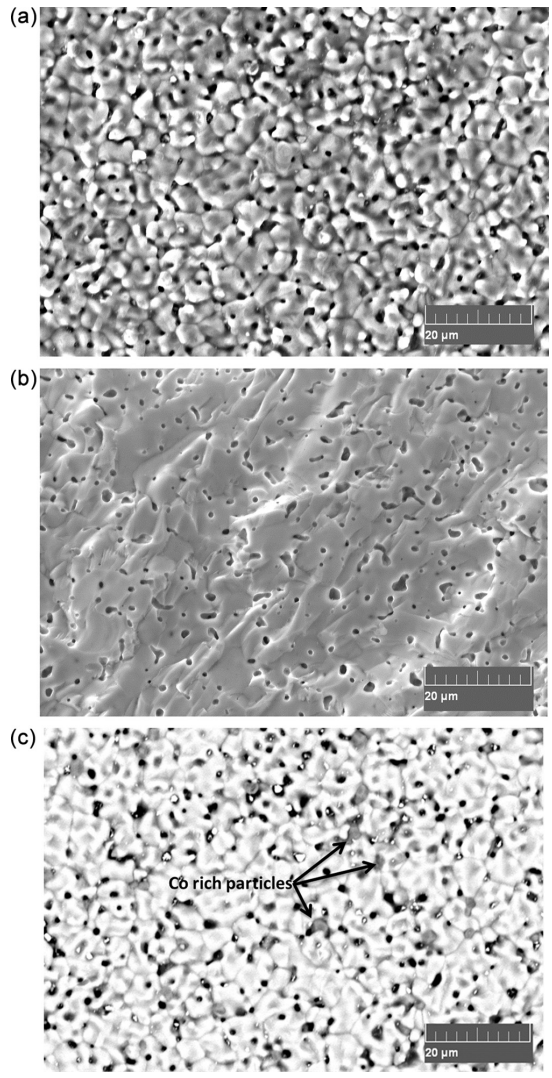

Fig. 2. BSCF secondary electron image of (a) surface and (b) fracture surface. The grains morphology and the closed porosity can be clearly observed. In (c) the Co rich particles dispersed on sample surface close to the grain boundaries can be seen as dark gray spots indicated by the arrows.

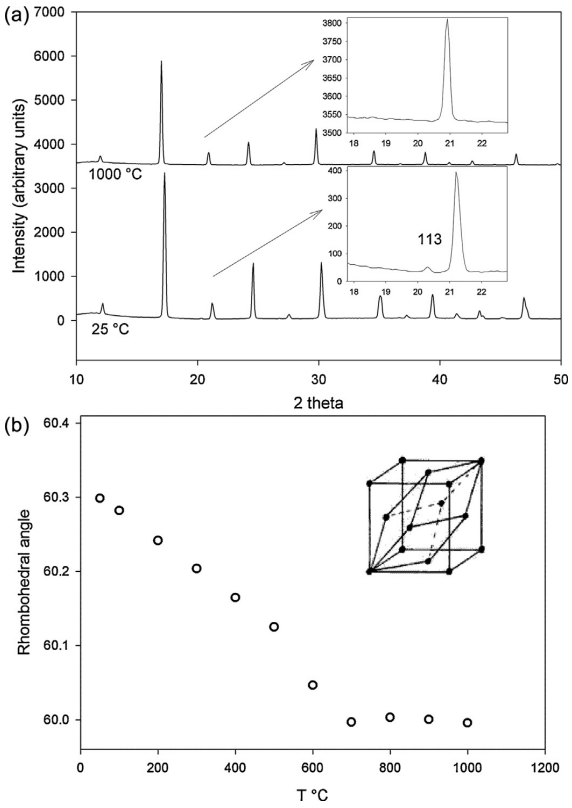

Fig. 3. (a) Synchrotron XRD pattern of LSCF sample at 25 °C and 1000 °C. The difference between rhombohedral and cubic symmetry is marked by the disappearance of the 113 Bragg peak. (b) the rhombohedral to cubic transition is also described by the evolution of the cell angle in rhombohedral setting, which becomes 60 °C above 700 °C, as expected for a metrically cubic lattice.

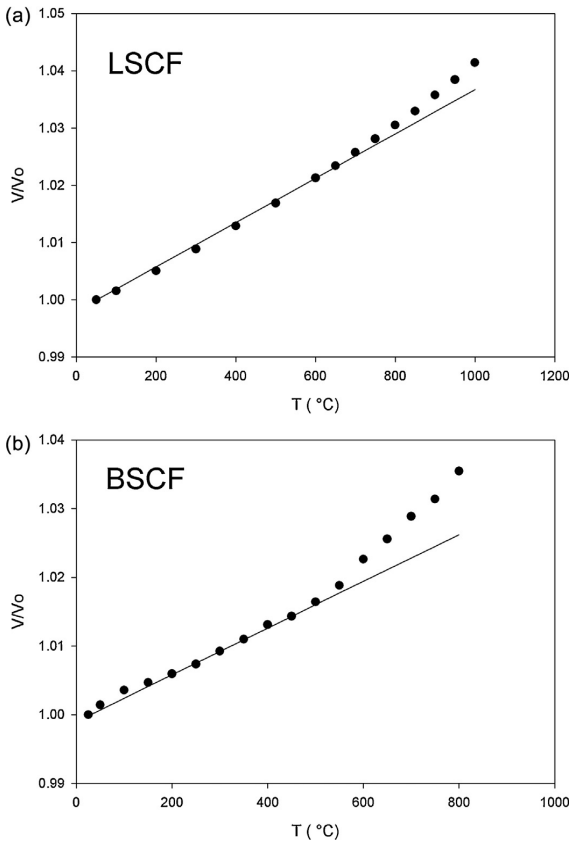

Fig. 4. Thermal expansion measured by XRD of synchrotron radiation for (a) LSCF and (b) BSCF, respectively. Circles refer to experimental points. The line is calculated by fitting data up to 600 °C and extrapolating at higher temperature, to evidence the increase of thermal expansion above 600 °C.

Table 2
Average TEC values within each temperature linearity range for LSCF.

	30–630 °C	630–900 °C
LSCF in Ar	14.7×10^{-6} °C^{-1}	25.3×10^{-6} °C^{-1}
LSCF in O_2	14.7×10^{-6} °C^{-1} (30–700 °C)	20.2×10^{-6} °C^{-1} (700–900 °C)
LSCF HT XRD in Air	13.1×10^{-6} °C^{-1}	17.3×10^{-6} °C^{-1}

mainly at grain boundaries, see Fig. 2c. XRD analyses relieved both CoO and Co_3O_4.

3.1.1. High temperature XRD

The LSCF sample, heated in air, shows a structural transition from the R-3c to the Pm-3 m structure above 750 °C, detectable by the disappearance of Rhombohedral superstructure diffraction peaks in XRD spectra. The geometric transformation of the unit cell at about 700 °C is confirmed by the Rhombohedral angle evolution versus temperature (see Fig. 3), since this angle is 60° in a cubic lattice but deviates from this value as soon as the lattice geometry changes. X-ray diffraction recorded during cooling confirms that the transition is reversible as the quenched sample structure is again rhombohedral. By measuring the unit cell increase the thermal expansion was estimated as a function of the temperature (Fig. 4a and Table 2). Furthermore a slight thermal expansion increase, possibly related also to the rhombohedral/cubic phase transition can be observed at temperatures higher than 800 °C.

On the opposite, the BSCF material does not present any structural transition or decomposition during heating in air to 1000 °C as the results of synchrotron XRD measurements indicate, within the experimental accuracy of this technique. However, above 600 °C a significant increase of both the lattice parameter and the thermal expansion coefficient is measured, as reported in Table 3 and in Fig. 4b.

3.1.2. Differential dilatometry in different atmospheres

The plots of differential expansion ($\Delta L/L_0$) as a function of the temperature measured in Ar and O_2 atmospheres for BSCF and LSCF are shown in Fig. 5. The corresponding estimated values of TEC are summarised in Tables 2 and 3. Both dilatometry and X-ray diffraction indicate an increase of thermal expansion coefficient above 600 °C. The variations of $\Delta L/L_0$ as a function of the temperature are more pronounced for BSCF than LSCF membranes. The inert atmosphere (Ar) contributes to anticipate at lower temperatures the TEC transition and to increase significantly the high temperature TEC value. In particular in the case of BSCF tested in inert atmosphere three distinct linearity zones (instead of two) can be distinguished (see Table 3). A comparison of the TEC experimental results for BSCF with values reported in the literature is provided in Table 3.

Table 3
Average TEC values within each temperature linearity range for BSCF.

	30–500 °C	500–700 °C	700–900 °C	30–800 °C
BSCF in Ar	13.3×10^{-6} °C^{-1}	$33.9 \cdot 10^{-6}$ °C^{-1}	24.7×10^{-6} °C^{-1}	
BSCF in O_2	13.1×10^{-6} °C^{-1} (30–550 °C)	–	26.6×10^{-6} °C^{-1} (550–900 °C)	
Ref. [7]	8.7×10^{-6} °C^{-1} (30–300 °C)	–	25.1×10^{-6} °C^{-1} (500–800 °C)	18.7×10^{-6} °C^{-1}
Ref. [8]	8.7×10^{-6} °C^{-1} (30–300 °C)	–	25.1×10^{-6} °C^{-1} (500–800 °C)	20.44×10^{-6} °C^{-1}
Ref. [6]	$9–11 \times 10^{-6}$ °C^{-1} (up to 500 °C)	–	$16–19 \times 10^{-6}$ °C^{-1} (up to 1050 °C)	
Ref. [24]	–	–	–	$16–18 \times 10^{-6}$ °C^{-1}
Ref. [26]	–	–	–	19.6×10^{-6} °C^{-1}
BSCF HT XRD in air	11.2×10^{-6} °C^{-1}		20.6×10^{-6} °C^{-1} (550–800 °C)	

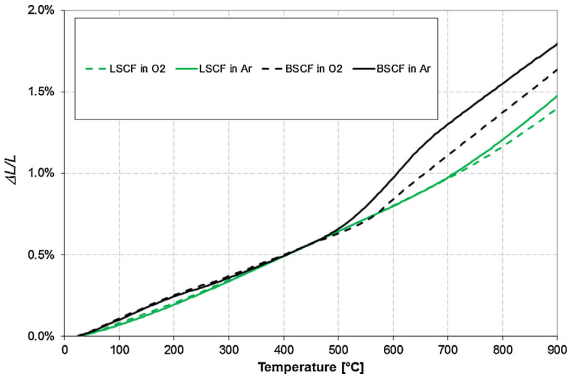

Fig. 5. Dilatometry results as a function of the temperature and environment, for BSCF and LSCF: $\Delta L/L_0$ slope variations occur at 550 °C and 700 °C, respectively. They are more pronounced for BSCF and Ar atmosphere, compared to LSCF (700 °C) and O_2 atmosphere.

In the whole 30–800 °C temperature range, the average measured TEC (18×10^{-6} °C^{-1}) results in very good agreement with all the data reported in the literature [28,30], comparing measurements carried out in O_2 to tests performed in air, although the trend does not appear linear. Also the results of weight variations are in good agreement with thermo-gravimetric values reported in the literature; in particular for compositions similar to BSCF, Ovenstone et al. [17] and Li et al. [4] report weight losses at high temperature: 0.8% (in air) and 1.5% (6×10^{-4} atm pO_2). Cooling down at RT, a partial weight recovery takes place: 1% in air and 0.5% in 6×10^{-4} atm pO_2. Thus, the net weight variations for BSCF are 0.2% in air and −1% in a very poor of oxygen atmosphere. The values obtained in this work are similar: 0.18% (±0.08) in O_2 and −1.3% (±0.2) in Ar. Comparing BSCF and LSCF results, it can be noticed that in O_2 atmosphere LSCF shows a smaller weight gain (0.03% ± 0.2) than BSCF; moreover in Ar LSCF has a positive weight variation (0.615% ± 0.05), while BSCF has a bigger and negative weight variation.

For LSCF the increased thermal expansion can be mainly related to the structural transition from the rhombohedral phase at RT to the high temperature cubic phase.

For BSCF the change in thermal expansion can be explained by varied electronic properties such as partial reduction of atomic species and charge transfer between cations. In particular, the loss of oxygen in the crystal lattice at elevated temperatures promotes a reduction of the valence state of Co and Fe from +4 to +3. When the temperature increases further, a new reduction of the valence state of Co and Fe (from +3 and +2) can occur. The TEC increases at each valence state reduction [33,34]. as a lower valence state corresponds to a bigger cations size.

3.2. Characterization after aging at high temperature

3.2.1. LSCF

The LSCF specimens exposed at 780 °C until 480 h (20 days) were analyzed at RT with synchrotron radiation; no significant difference compared to the spectra of the as received material is noticed. Similar results were obtained on the specimens exposed at 820 °C for similar duration. These results confirm the stability of the LSCF compound in the examined temperature range, in agreement with the literature [5–8].

3.2.2. BSCF

Aging treatments were done at the three temperatures 780, 800 and 820 °C, with durations increasing from few days up to several weeks. After aging in an air furnace, specimens have differently colored surfaces: the side exposed to air is black and the other (in contact with the alumina specimen holder) is grey, similar to the as-received material. The surface of the black side is covered by very tiny crystals, sulphur rich as pointed out by WDS analysis (Fig. 6). Two-dimensional XRD measurements in reflection mode and MicroRaman spectroscopy indicate on the black side of aged samples the presence of pure $BaSO_4$ (Figs. 6c, 7b) and mixed $Ba_{0.5}Sr_{0.5}SO_4$ (Fig. 7a). The formation of sulphates on the sample surface exposed to air is related to the presence of sulphur in the binding used for the ceramic sintering, as already mentioned in literature [40,41].

In the 2D XRD spectra taken on the grey side of the same samples, the peak at 27 reveals the presence of the hexagonal phase $(BaSr)CoO_3$ (Fig. 7a). Its intensity increases with the exposure time in the furnace, as more accurately confirmed by the synchrotron results. This secondary phase is present at the grain boundaries, as very small particles after the shorter exposure times and as a lamellar phase after exposure times longer than 59 days (B9 specimen in Fig. 8a). WDS mapping performed with the Jeol microprobe (Fig. 8b and c) indicates that such phase is rich in Co and poor in Fe compared to the matrix. This is expected for the hexagonal phase, known as $(BaSr)CoO_3$ having a precise crystallographic relation with the cubic perovskitic matrix [17]. Where a thicker hexagonal phase layer formed, an iron enrichment in the adjacent perovskite grain is clearly visible, as in the Fe map of Fig. 8c. Moreover on the surface of the aged specimens, several particles rich in Co are present (Fig. 8b); Co oxides were already present in the as delivered material, but probably grew in number and size during high temperature exposure, even if no quantification effort was made here.

3.2.3. Kinetics of hexagonal phase formation

To collect more information about the kinetics of the hexagonal phase formation both traditional and synchrotron radiation XRD were performed on the aged specimens. An homogeneous synchrotron data set on powdered material was used to

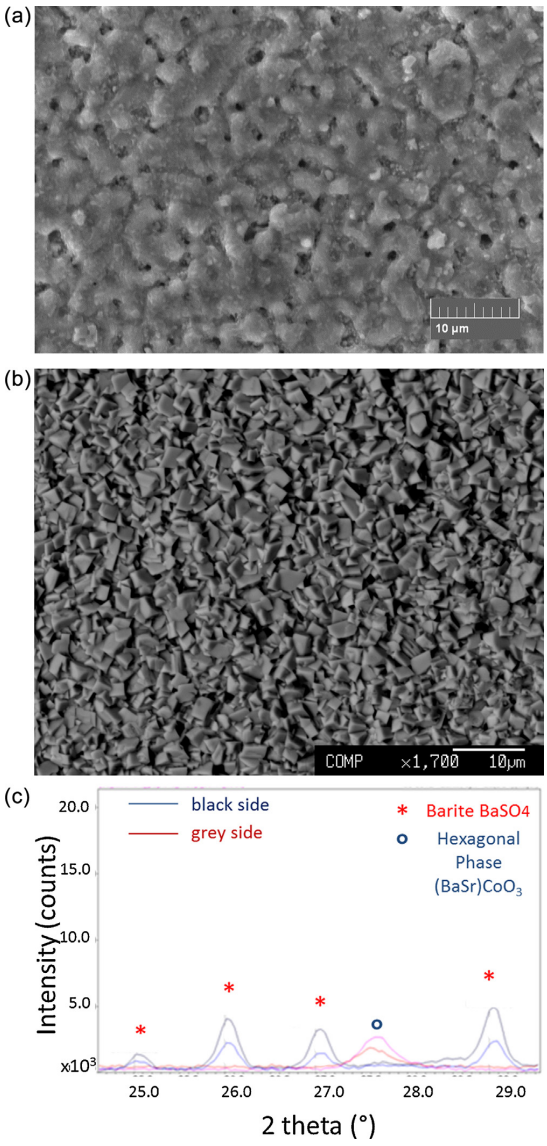

Fig. 6. aged BSCF membranes: surface morphology after aging: (a) a very fine microstructure superimposed to the original one (see Fig. 2a) promoted by the high temperature exposure can be observed on the surface of sample B8 aged 20 days at 780 °C and (b) small sulphates crystals grown on the sample surface exposed to air for B11 sample aged 40 days at 780 °C (c) XRD spectra of B11 sample: the peaks of Ba sulphates and hexagonal phase can be seen on black and grey surfaces, respectively.

extract the phase fraction of cubic and hexagonal phases, by the Rietveld method, using structural models reported in literature [24,32]. The experimental hexagonal phase content is plotted as a function of the aging time in Fig. 9 for each temperature, together with the relative fitting curves, according to the modified Johnson–Mehl–Avrami model [32]:

$$\alpha_{hex}(t) = \alpha_{hex}(\infty) \times \left(1 - e^{-kt^n}\right) \quad (1)$$

where $\alpha_{hex}(t)$, $\alpha_{hex}(\infty)$, are the volumetric fractions of the hexagonal phase after an aging time t and after an infinite time; k and n are

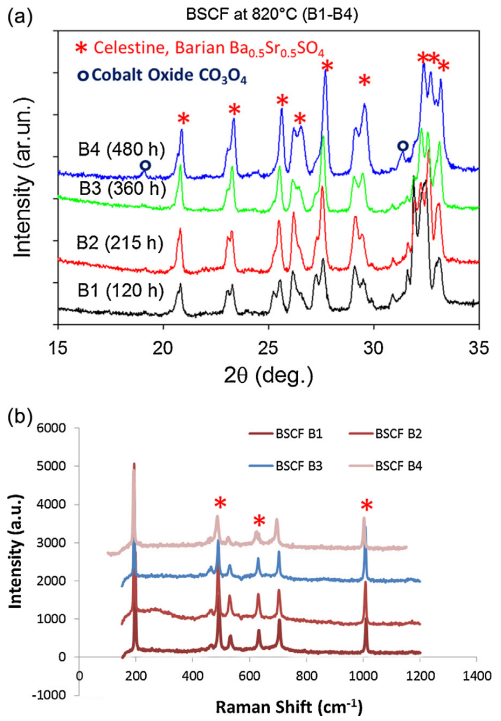

Fig. 7. (a) XRD and (b) Raman spectra of BSCF exposed to 820 °C as a function of time. The peaks in figures correspond to barium-strontium (Barian Celestine) and pure barium (Baryte) sulphates, respectively.

Table 4
Parameters of the fitting curves with the modified Johnson–Mehl–Avrami model.

Ageing temperature	$\alpha_{hex}(\infty)$	Characteristic time $\tau = 1/k$ [days]
BSCF 780 °C	32.2%	26.3
BSCF 800 °C	21.2%	14.7
BSCF 820 °C	11.7%	11.5
BSCF 800° literature	52.3%	17.8

the rate constant of formation of hexagonal phase and the Avrami coefficient, respectively.

As the hexagonal phase nucleation occurs mainly at grain boundaries (as shown in Fig. 8), the experimental data are fitted after setting the Avrami coefficient $n = 1$, as also suggested by Mueller et al. [32]. For this value of n, the reciprocal of the kinetic constant k can be interpreted as the characteristic time τ of the process (time required to reach about 63% of the value $\alpha_{hex}(\infty)$). The fitting parameters found at the studied temperatures are summarized in Table 4 and compared with published data at 800 °C [32]. Both the characteristic time τ and the $\alpha_{hex}(\infty)$ values decrease from about 30% to 12% by increasing the aging temperature from 780 °C up to 820 °C. This happens as 820 °C approaches the upper boundary of the transformation domain (hexagonal phase formation limit is found at 840 °C in [24] and at 825 °C in [25]). The volume phase fraction of the hexagonal phase at infinite time at 800 °C of this work (21%) is significantly smaller than that (52%) reported by Mueller et al. [32]. Several elements can contribute to explain such difference: different experimental XRD techniques, different grain size (as smaller the grain size as more grain boundaries are present as possible hexagonal formation sites [24]); moreover not all the grain boundary sites could be active for the process, possibly due

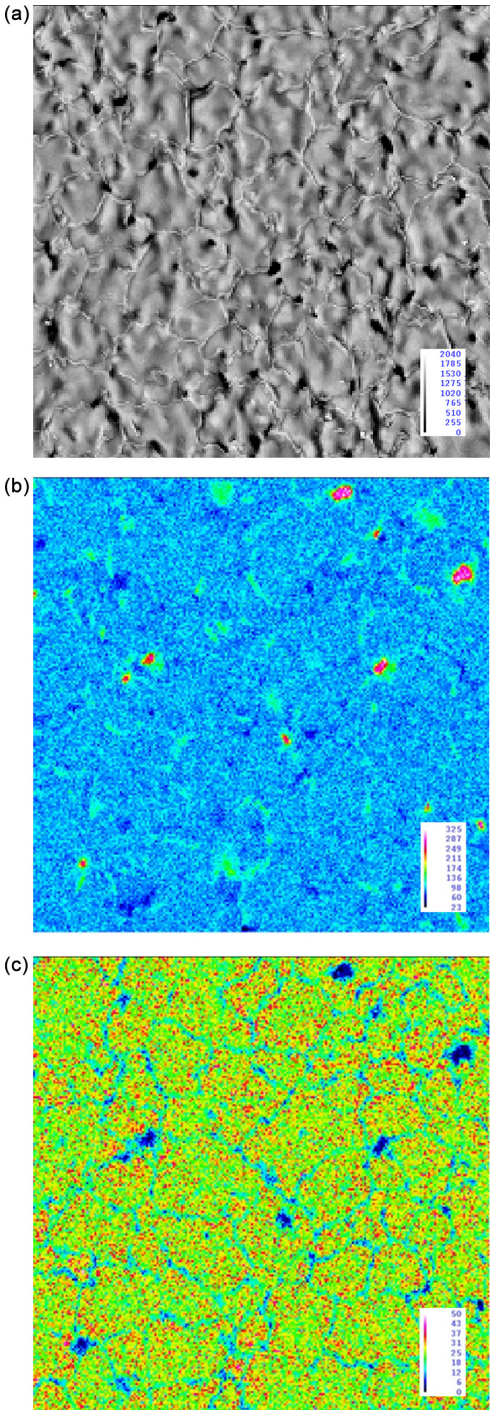

Fig. 8. (a) Surface morphology of B9 BSCF sample aged for 54 days. A secondary phase is present at the grain boundaries, as a lamellar phase. WDS mapping of sample B8 (aged 20 days at 780 °C) indicates that such phase is rich in (b) Co and poor in (c) Fe compared to the matrix.

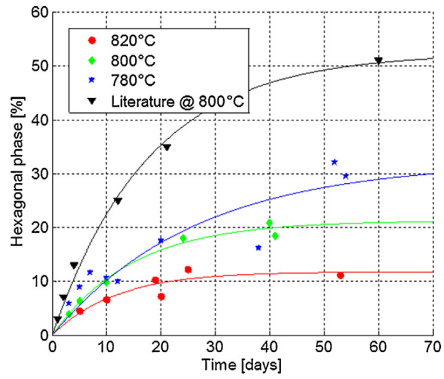

Fig. 9. Avrami plot for BSCF samples aged at three temperatures. For comparison purposes literature data [25] are reported as well.

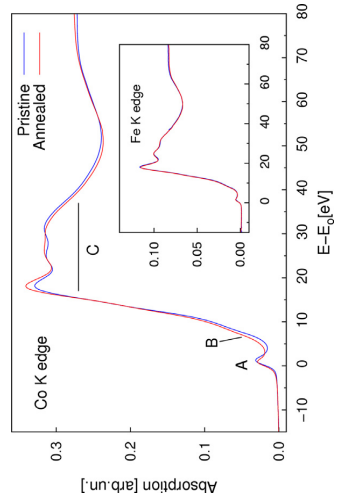

Fig. 10. XANES spectra collected at the Co K edge and Fe K edge (inset) on BSCF pristine sample (blue) and exposed at 800 °C for 40 days (red curves). The effect of annealing is evident for the Co K edge spectra at pre-edge peak (A), in the edge raising (B) and in the post edge region (C), the Fe K edge spectra remains unchanged upon annealing. (For interpretation of the references to color in this figure legend, the reader is referred to the web version of this article.)

to the presence of some impurities (e.g. S from the binder). On the contrary, the characteristic time found here at 800 °C is sufficiently similar to the literature value (difference = 17% Table 4).

3.2.4. XANES results

The fine features in the near edge region of X-ray absorption spectra (XANES) provide information about the electronic state of the absorber and its local coordination chemistry. The normalized Fe K edge spectra of BSCF in the as received and annealed (BSCF-26 aged 40 days = 960 h at 800 °C) conditions are shown in Fig. 10; they are very similar and consistent with Fe^{3+} valence state [38] octahedral coordinated (FeO_6 units). This demonstrates that the effect of annealing on the average valence state and local atomic structure of Fe ions is negligibly weak. The Co K edge XANES spectra depict definitively different behavior (Fig. 10): upon annealing the pre-edge peak area decreases, (label A in Fig. 10), the onset of the edge shifts toward lower energy label B in Fig. 10 and the post edge features largely change (C region in Fig. 10). The pre-edge peak (A)

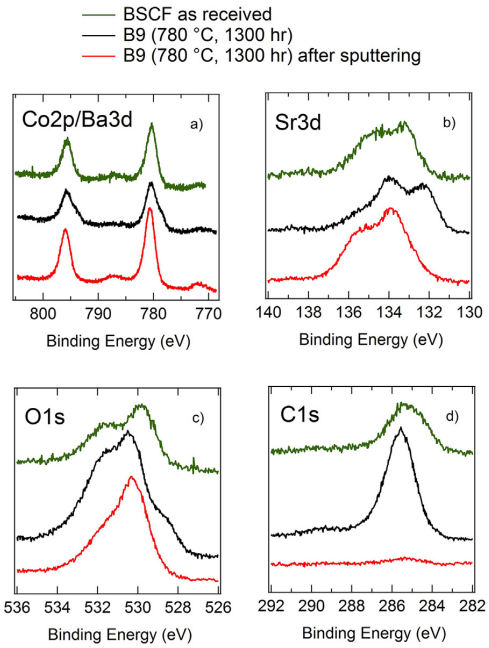

Fig. 11. XPS spectra of C, Sr, O and Sr relative to a BSCF sample characterised in as delivered and aged at 780 °C (B9–54 days) conditions. (For interpretation of the references to color in the text, the reader is referred to the web version of this article.)

reflects the density of empty electronic state (hybridized p-d states) at the Co site; the observed reduced intensity upon annealing is proving some charge transfer to Co reducing its oxidation state, this is confirmed by the low energy shift of the edge B onset in the same Fig. 10. The modifications of the post edge signal of Co are associated to a variation in valence state and in the average local atomic structure of this element.

3.2.5. X-ray photoemission spectroscopy results

First surface atomic layers of as delivered and aged BSCF (only on the clean grey side) were analyzed by XPS Some sputtering was necessary to eliminate the high surface contamination almost hiding the native structure of the sample (very low intensity of Co, Ba, Fe and Sr peaks). Fig. 11 shows the high resolution spectra of BSCF specimens: as received (green line) and aged 1300 h at 780 °C (B9) before (black line) and after sputtering (red line) at the Co2p/Ba3d, Sr3d, O1s and C1s edges. The comparison between spectra of the aged sample before and after sputtering let to appreciate the removal and/or the variation of the species present at the surface.

The overlapping between the Co2p and Ba3d edges (shift ~0.3 eV) with the same doublet splitting (15.3 eV) needs an accurate peak deconvolution in order to bring out the various components (Fig. 11a). The main features centered at 780.2 eV (Co 2p 3/2 and Ba 3d 5/2) and 795.5 (Co 2p 1/2 and Ba 3d 3/2) eV are compatible with both elements in the perovskite phase. The deconvolution allows also to identify a small contribution of a $BaCO_3$. The propensity of the material to form carbonates observed here was also highlighted in [42–44]. The shoulders emerging after annealing at lower energies, namely 778.4 and 793.6 eV, could be associated with a reduced state of the cobalt for example in the spinel Co_3O_4 even if there is no clear evidence of additional broad shake-up peaks at about 787.2 eV and 803.1 eV. Another attribution could be a bond of cobalt with a more electronegative trace element present as contaminant. However this contribution disappears after sputtering confirming a superficial nature of the peak.

The Sr 3d edge (Fig. 11b) is mainly ascribable to strontium bonded to oxygen in a perovskite structure and for the aged sample feature of carbonate in the form $SrCO_3$ is superimposed.

The barium and strontium carbonate are mirrored by a low intensity peak at the higher binding energy (289.6 eV) in C1s edge (Fig. 11d). Otherwise the carbon peak as the usual structure related to adventious carbon species (~285.5 eV). The moderate sputtering almost completely removes the carbon as well as the related carbonate contribution in Ba and Sr profiles. This trend is also reflected in the O1s peak (Fig. 11c) as indicated by the strong lowering of the shoulder in the O1s peak at about 531.8 eV after sputtering, thus ascribable to carbonate species (CO_3^{2-}) and adsorbed oxygen containing species. The main structure in the region between 529.6 and 530.5 eV is characteristic of the perovskite phase.

The intensity of the Fe2p peaks is so low in all the acquired spectra (not shown) that no reliable data analysis can be carried out on them.

3.3. Observations on membranes after permeation tests

Three disc shaped membranes were tested: one LSCF (L2) and two BSCF (B1 and B2), in the testing conditions shown in Fig. 12. The experimental permeated O_2 fluxes (Fig. 12d) are in line with the results reported in literature for both materials [18,31] and for all the membranes no difference in the oxygen flux was measured over time. After testing, the characterization of the morphology, crystal structure and chemical changes was performed by means of SEM + EDS and WDS, XRD and XPS, on both sides of the samples.

The LSCF membrane does not show any significant change in the crystallographic structure nor in the surface morphology, compared to the as delivered material. The main achievement obtained by XPS measurements is the accumulation of oxygen ions on both sides, as assessed by the peak at about 528.9 eV (Fig. 13). This feature is more evident on the side exposed to the gas flow and is completely removed by the sputtering. A similar superficial accumulation of oxygen is not evident in the BSCF membrane.

On the opposite the BSCF membranes B2 and B1 show some degradation at the two surfaces: the air (process) side shows sulphates formation in the central area (as on the black side of aged samples) and swellings/cracking in regions where permeation was not occurring, probably owing to the oxygen adsorption and thermal cycles. On the surface of membrane B2 tested in air the morphology of the air side appears similar to the as delivered material, but some swelling was observed in a small region (Fig. 14a); also a decoration of tiny particles is present and can be attributed to the initial sulphate formation [42] (Fig. 14b).

On the sweep side, the surface morphology of B2 is rough only in some local regions, where areas with very different atomic weigh are evidenced by Backscattered Electron Images (see Fig. 14c and d). In the WDS maps the presence of Co oxides is quite clear and the heavy cations distribution is not uniform. Local quantitative WDS measurements show regions with quite different Fe contents. The decomposed layer is only about 1 micrometer thin on B2, as seen on a fractured surface.

More evident is the kinetic decomposition on the sweep side surface of the membrane B1, tested also in pure oxygen (see Fig. 12c). As shown in Fig. 15, circular areas of different colors are visible on both sides, with the shape related to the configuration of the permeation cell used The 2D- XRD integrated spectra of Fig. 15 were obtained using a 300 μm collimator in the laboratory at 20° reflection angle, to distinguish central area from regions around it. The width of the perovskitic phase peaks relative to the center of the air side is similar to the as delivered specimen, as here the compound and the average size of crystal-

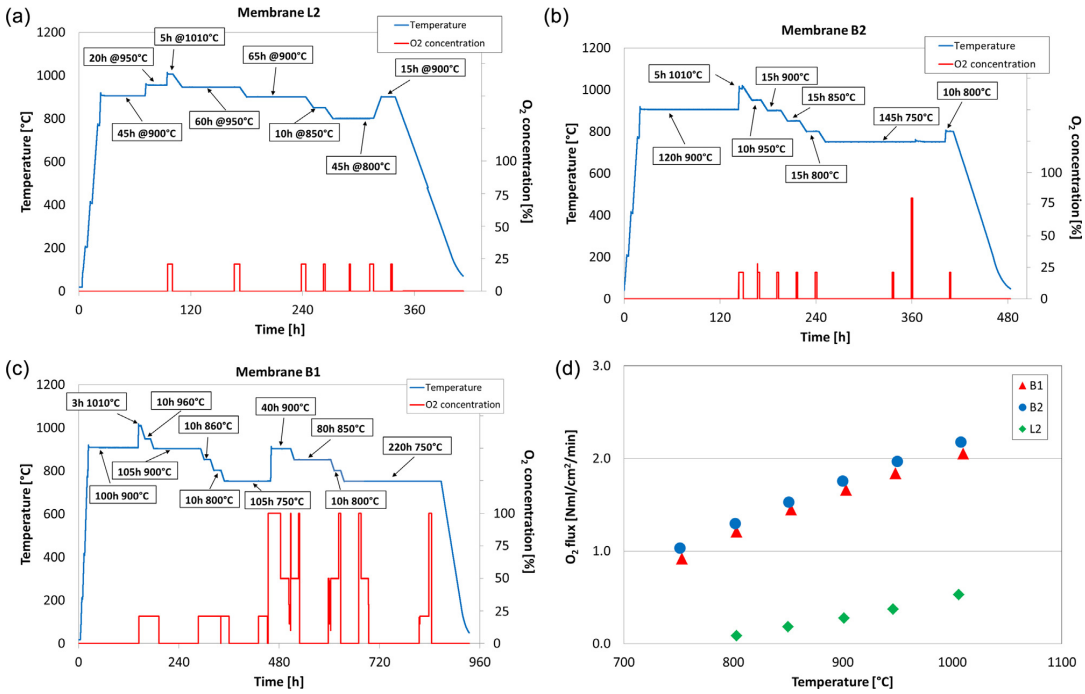

Fig. 12. Temperature vs. time profile for permeation tests performed on membranes (a) L2, (b) B2, (c) B1, respectively. (d) Permeation results of B1, B2 and L2 in terms of permeated oxygen flux.

lites remain unchanged, but other peaks of a new phase appear at $2\theta = 29^\circ$, $2\theta = 26^\circ$, attributable to Barium Sulphate. This compound was detected also in the synchrotron spectrum on the air side and was confirmed also by the microRaman spectroscopy, similarly to findings on the side exposed to air of furnace aged BSCF samples (see previous section) and in agreement with [41,42].

At the center of the sweep (permeate) side of B1 the presence of binary oxides is detected by XRD of synchrotron radiation; they are identified as *Co* oxides both by lab XRD (Fig. 15) and SEM + EDS [32,33]. Here the broadening of the cubic perovskitic phase peaks at high angle in the lab XRD spectra suggests a significant reduction of crystallites size and possibly an initial kinetic demixing of the perovskite phase. Actually SEM observations show a significant surface roughening in the circular central region (Fig. 15), near the sweep gas inlet; backscattered electron images indicate regions with different atomic weight. In surrounding regions where the sweep gas flow is low, or almost absent, the grain boundaries of the perovskite grains are "corroded" and many *Co* oxides are present, as confirmed also by SEM-EDS-WDS analyses [24,25]. No sulphate formation was detected at the sweep side, due to the reducing environment. In the XRD spectra collected on both sides no presence of hexagonal phase was detected, but XRD data provide indications that irreversible decomposition processes (kinetic demixing) take place, even if mainly at the sweep side surface.

4. Discussion

In the frame of this work, the LSCF membranes show a rather stable behaviour in terms of oxygen permeation along with the testing duration in the whole temperature range. The LSCF membrane does not show any significant change in the crystallographic structure nor in the surface morphology.

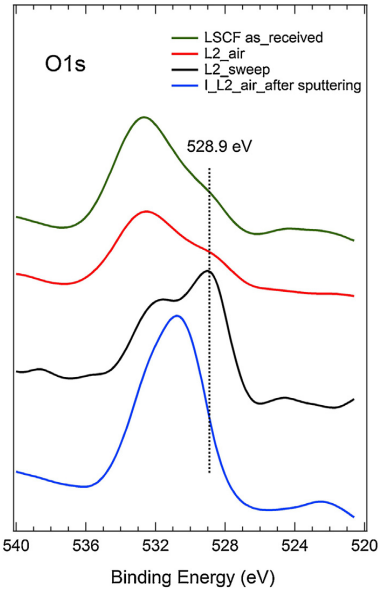

Fig. 13. XPS results obtained on L2 membrane after permeation test. The dashed line shows the peak position (528.9 eV) related to the presence of oxygen ions.

On the opposite BSCF, which presents the best transport properties, has higher structural instability. The first degradation process is a reversible formation hexagonal phase at the grain boundaries of

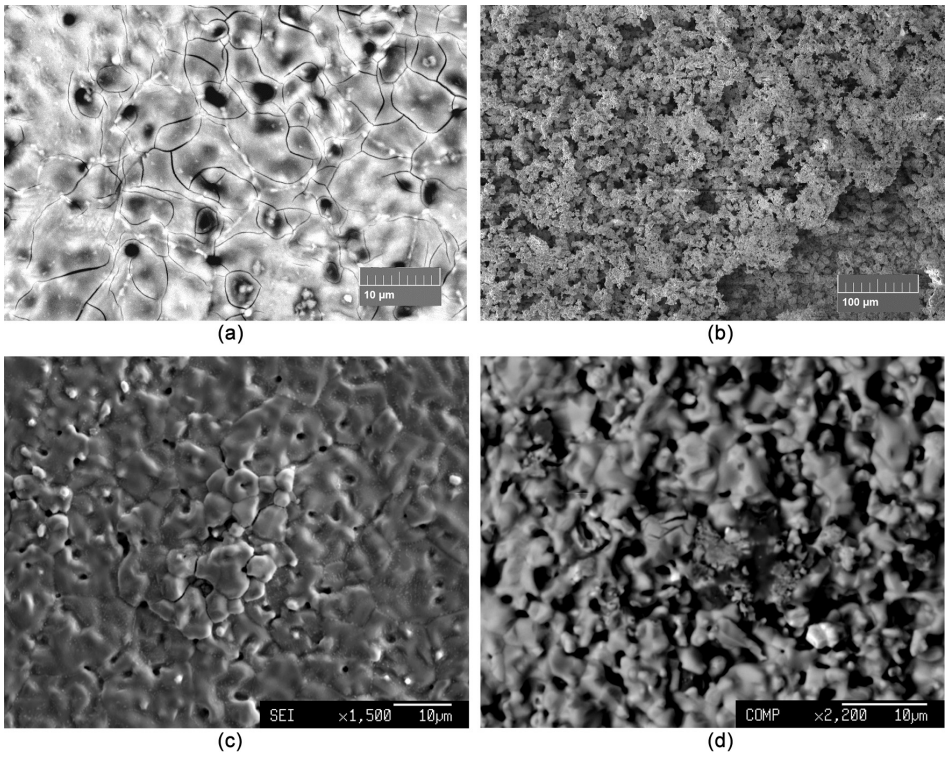

Fig. 14. SEM morphology of the two sides of B1 and B2 membranes after permeation tests; (a) B1 air side swelling and cracking, (b) B1 sweep side rough areas, (c) B2 air side swelling and cracking, (d) B2 sweep side rough areas.

the cubic perovskite between 700 and 840 °C. The quantitative XRD results here shown help to better define its kinetics on respect previous published work, using weight percent values of the hexagonal phase determined by synchrotron radiation excited XRD spectra. The Avrami model coefficients are now determined at three temperatures 780, 800 and 820 °C. The mechanism proposed by several authors for this process reversible at higher temperatures [24,32] is confirmed by the results obtained here, even if such process in our opinion can be considered more as the formation of a secondary phase, with a definite coherence with the mother perovskite, more than a true decomposition, as suggested by other authors. On the opposite a true decomposition in binary and ternary oxides happens during permeation, as more as higher is the oxygen pressure difference between the two sides of the membrane, as indicated by the results of observations performed here on the B1 and B2 membranes. BSCF actually suffers of kinetic demixing[1], detected by XRD, caused by the difference between the diffusion coefficient for A-cations (Ba, Sr) compared to B-cations (Co, Fe). The crystallographic structure of the cubic perovskite is based on edge shared CoO_6 octahedral chains, connected by Ba, Sr cations forming ionic bonds with oxygen anions of the chains; the octahedral are centered by Co. The structure of the hexagonal phase determines a

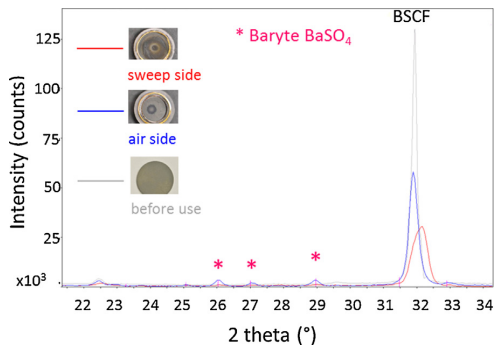

Fig. 15. Sample B1. XRD spectra of air and sweep sides compared to the as delivered sample. The presence of pure barium sulphate on the air side can be observed. The broadening of perovskite peak on the sweep side can be clearly seen.

octahedral cation-cation distance shorter than in the cubic perovskite structure, where octahedral are connected through corner sharing (Fig. 16).

For this reason, Co is preferred in the structure compared to Fe and a slightly reduced valence is also preferred, as confirmed by XANES results. No Fe-oxide phase is detected within experimental resolution as result of BSCF hexagonal transformation in aged specimens. It is likely taking place a rediffusion of Fe in the perovskite structure, through a schematic reaction which

[1] Since the kinetic demixing is very slow and involves only the surface of the samples (1 mm thick), no difference in terms of oxygen flux was observed during the permeation tests. Only for very thin membranes, where the surface exchange reaction is the limiting step of the permeation process, the kinetic demixing could be an important phenomenon affecting the permeation performances.

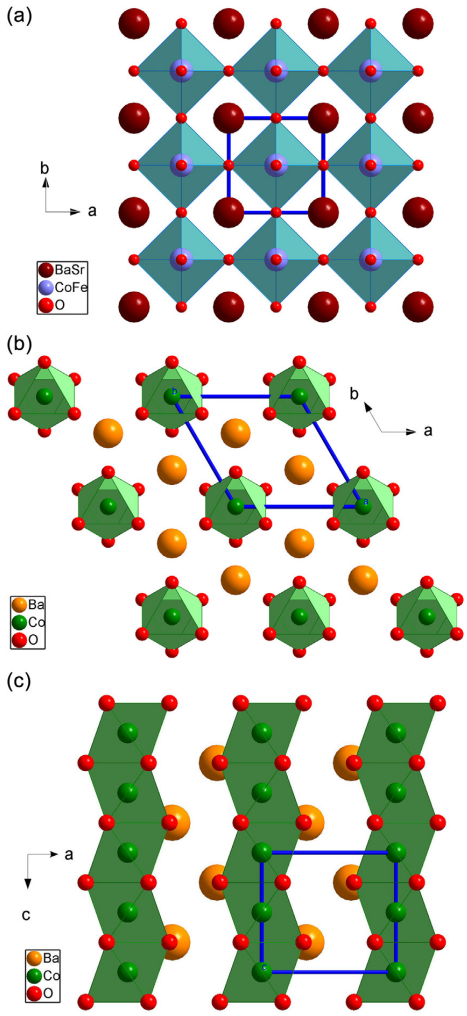

Fig. 16. (a) Crystal structure of cubic BSCF perovskite. It is based on corner-sharing (Co, Fe) octahedral, with (Ba, Sr) in the large [12]-fold coordinated interstitial sites. (b) Crystal structure of hexagonal $BaCoO_3$ viewed along crystallographic *c* axis. The CoO_6 octahedra are arranged in columns parallel to the *c* axis; (c) view of the hexagonal $BaCoO_3$ structure along *b* axis. The CoO_6 columns are edge-sharing. This topology reduces the Co–Co distances as compared to the cubic perovskite structure.

consider only the Co and Fe species, as confirmed qualitatively by the WDS maps of Co and Fe (see Fig. 8b and c). Iron concentration is higher in regions of the perovskitic grains near the grain boundaries where hexagonal phase rich in Co and Ba is present.

Also XPS findings for samples aged long times indicate that near the Co2p doublet associated to Co^{3+} also a small secondary doublet appears at higher binding energy (indication of a reduction of Co oxidation state).

This complex ceramic material is also very sensitive to the presence of impurities such as *S* coming from the sintering binder or to carbon presence, as demonstrated by XPS analyses of the first surface layers.

5. Conclusions

Several state of the art probes have been exploited to carefully investigate degradation mechanisms of BSCF and LSCF membranes occurring during high temperature aging and permeation tests.

SEM, WDS, XRD and differential dilatometry techniques confirmed that both BSCF and LSCF samples considered for this study have the nominal composition and microstructure and behave, as expected when exposed to high temperature. Only in the case of BSCF samples, CoO and Co_3O_4 oxides at grain boundaries have been detected, as a secondary phase.

Aging tests confirmed that LSCF samples are stable within the temperature (780–820 °C) and time (48–1272 h) ranges investigated within the present study.

On the contrary, after high temperature exposure in air, the formation of $BaSO_4$ and $Ba_{0.5}Sr_{0.5}SO_4$ in form of tiny crystals on the surfaces of BSCF samples, caused by the sulphur present in the binding used for sintering membranes and the secondary hexagonal phase $(BaSr)CoO_3$ whose morphology evolves with exposure time from small spherical to lamellar shaped particles were detected by SEM, WDS, XRD and microRaman. Furthermore, XPS analysis allowed to highlight the formation of a thin layer of Ba and Sr carbonates ($BaCO_3$ and $SrCO_3$) on the sample surface, as well.

Quantitative synchrotron radiation diffraction measurements of hexagonal phase content allowed the determination of Avrami coefficients at 780, 800 and 820 °C for BSCF. The temperature driven hexagonal phase content variation is associated to the enrichment of Fe in the regions of grains near the lamellar hexagonal phase, as WDS maps showed. In the investigated temperature range, by increasing the temperature, the estimated characteristic time τ and the asymptotic volumetric fraction of the hexagonal phase vary from about 26 to 11 days and from 32% to 12%, respectively. While τ resulted in good agreement with literature data available at 800 °C, the estimated asymptotic volumetric fraction of the hexagonal phase resulted significantly smaller than the value available in the literature. Possible reasons for this occurrence could be the differences in the microstructure and impurities that could prevent sites to be active for this decomposition process in the two phases $(Ba, Sr)CoO_3$ + Fe and Sr rich BSCF).

Bulk measurements of XANES and the analysis of the Co2p doublet in XPS spectra confirmed a reduction of Co ions oxidation number after long time at intermediate temperatures.

After medium term permeation tests any significant variation in the oxygen flux was observed and the crystallographic structure, the surface morphology and chemical changes were characterized by SEM + EDS, WDS, XRD and XPS, on both sides of the tested membranes.

Only on BSCF samples a kinetic decomposition consisting in Co oxides formation and surface swelling and cracking on air side was detected by SEM and EDS. On the other hand, on the sweep side, XRD analysis suggested an initial kinetic demixing of the perovskite phase. This phenomenon, consists in an enrichment of Fe and Co on the air side and of Ba and Sr on the sweep side. For the tests carried out in this work, the kinetic demixing had no influence on the permeation performances owing to the thick thickness of tested membranes, but for thinner membranes kinetic demixing could be an important degradation process for long term tests.

Acknowledgements

Prof. W.A. Meulemberg from Forshung Zentrum Julich (D) is acknowledged for providing all the membranes studied in the frame of this work. Dr. A. Risplendente (University of Milan—Earth Science Department) is acknowledged for assistance during microprobe analysis. Dr. A. Lausi, Dr. J. Plaiser and Dr. G. Aquilanti

are acknowledged for assistance during synchrotron experiments. Mr. S. Capelli—RSE is gratefully acknowledged for SEM and EDS analyses. This activity was financially supported by the Research Fund for the Italian Electrical System under the Contract Agreement between RSE S.p.A. and the Ministry of Economic Development—General Directorate for Nuclear Energy, Renewable Energy and Energy Efficiency stipulated on July 29, 2009 in compliance with the Decree of March 19, 2009.

References

[1] J. Sunarso, S. Baumann, J.M. Serra, W.A. Meulenberg, S. Liu, Y.S. Lin, J.C. Diniz da Costa, MIEC ceramic based membranes for O_2 separation, J. Membr. Sci. 320 (2008) 13–41.
[2] H. Kruidhof, H.J.M. Bouwmeester, R.H.E. Doorn, A.J. Burggraf, Influence of order-disorder transitions on oxygen permeability through selected nonstoichiometric perovskite-type oxides, Solid State Ionics 63–65 (1993) 816–822.
[3] K. Zhang, J. Sunarso, Z. Shao, W. Zhou, C. Sun, S. Wang, S. Liu, Research progress and materials selection guidelines on mixed conducting perovskite-type ceramic membranes for oxygen production, RSC Adv. 1 (2011) 1661–1676.
[4] S. Li, Z. Lu, X. Huang, B. Wei, W. Su, Thermal, electrical, and electrochemical properties of Lanthanum-doped $Ba_{0.5}Sr_{0.5}Co_{0.8}Fe_{0.2}O_{3-\delta}$, J. Phys. Chem. Solids 68 (2007) 1707–1712.
[5] H.L. Lein, K. Wijk, T. Grande, Thermal and chemical expansion of mixed conducting $La_{0.5}Sr_{0.5}Fe_{1-x}CO_x$ materials, Solid State Ionics 177 (2006) 1795–1798.
[6] H.L. Lein, K. Wiik, M. Einarsrud, T. Grande, E. Lara-curzio, High-temperature creep behaviour of mixed conducting LSCF materials, J. Am. Ceram. Soc. 89 (2006) 2895–2898.
[7] B.X. Huang, J. Malzbender, R.W. Steinbrech, L. Singheiser, Mechanical properties of $La_{0.58}Sr_{0.4}Co_{0.2}Fe_{0.8}O_{3-\delta}$ membranes, Solid State Ionics 180 (2009) 241–245.
[8] S. Hashimoto, Y. Fukuda, M. Kuhn, K. Sato, K. Yashiro, J. Misuzaki, Oxygen nonstoichiometry and thermo-chemical stability of $La_{0.6}Sr_{0.4}Co_{1-y}Fe_yO_{3-\delta}$ (y = 0. 2, 0. 4, 0. 6, 0. 8), Solid State Ionics 181 (2010) 1713–1719.
[9] B. Wang, B. Zydorczak, Z.-T. Wu, K. Li, Stabilities of LSCF6428 oxygen separation membranes—effects of kinetic demixing/decomposition and impurity segregation, J. Membr. Sci. 344 (2009) 101–106.
[10] B. Wang, B. Zydorczak, D. Poulidi, I.S. Metcalfe, K. Li, A further investigation of the kinetic demixing/decomposition of LSCF6428, J. Membr. Sci. 369 (2011) 526–535.
[11] S.M. Fang, C.Y. Yoo, H. Bouwmeester, Performance and stability of niobium-substituted BSCF5582 membranes, Solid State Ionics 195 (2011) 1–6.
[12] M. Arnold, H. Wang, A. Feldhoff, Influence of CO_2 on the oxygen permeation performance and the microstructure of perovskite-type BSCF5582 membranes, J. Membr. Sci. 293 (2007) 44–52.
[13] M. Betz, F. Schulze-Küppers, S. Baumann, W.A. Meulenberg, D. Stöver, Supported oxygen transport membranes for oxyfuel power plants, Sci. Technol. 72 (2010) 93–98.
[14] H. Wang, C. Tablet, A. Feldhoff, J. Caro, Investigation of phase structure sintering, and permeability of perovskite-type BSCF5582 membranes, J. Membr. Sci. 262 (2005) 20–26.
[15] S. Engels, et al., Oxygen permeation and stability investigations on MIEC membranes materials under operating conditions for power plant processes, J. Membr. Sci. 370 (2011) 58–69.
[16] N. Lakshminarayanan, H. Choi, J.N. Kuhn, U.S. Ozkan, Effect of additional B-site transition metal doping on oxygen transport and activation characteristics in $La_{0.6}Sr_{0.4}(Co_{0.18}Fe_{0.72}X_{0.1})O_{3-\delta}$ (where X = Zn, Ni or Cu) perovskite oxides, Appl. Catal. B: Environ. 103 (3–4) (2011) 318.
[17] J. Ovenstone, J. Jung, J.S. White, D.D. Edwards, S.T. Misture, Phase stability of BSCF in low oxygen partial pressures, J. Solid State Chem. 181 (2008) 576–586.
[18] X. Tan, Z. Wang, B. Meng, X. Meng, K. Li, Pilot-scale production of oxygen from air using perovskite hollow fibre membranes, J. Membr. Sci. 352 (2010) 189–196.
[19] X. Tan, N. Liu, B. Meng, J. Sunarso, K. Zhang, S. Liu, Oxygen permeation behavior of $La_{0.6}Sr_{0.4}Co_{0.8}Fe_{0.2}O_3$ hollow fibre membranes with highly concentrated CO_2 exposure, J. Membr. Sci. 389 (2012) 216–222.
[20] Z. Shao, W. Yang., Y. Cong, H. Dong, J. Tong, G. Xiong, Investigation of the permeation behavior and stability of a $Ba_{0.5}Sr_{0.5}Co_{0.8}Fe_{0.2}O_{3-\delta}$-oxygen membrane, J. Membr. Sci. 172 (2000) 177–188.
[21] D. Schlehuber, E. Wessel, L. Singheiser, T. Markus, Long-term operation of a $La_{0.58}Sr_{0.4}Co_{0.2}Fe_{0.8}O_{3-\delta}$-membrane for oxygen separation, J. Membr. Sci. 351 (2010) 16–20.
[22] S. McIntosh, J. Vente, W. Haije, D. Blank, H.J.M. Bouwmeester, Oxygen stoichiometry and chemical expansion of $Ba_{0.5}Sr_{0.5}Co_{0.8}Fe_{0.2}O_{3-\delta}$ measured by in situ neutron diffraction, Chem. Mater. 18 (2006) 2187–2193.
[23] M. Arnold, Q. Xu, F. Tichelaar, A. Feldhoff, Local charge disproportion in a high-performance perovskite, Chem. Mater. 21 (2009) 635–640.
[24] C. Niedrig, S. Taufall, M. Burriel, W. Menesklou, S. Wagner, S. Baumann, E. Tiffée, Thermal stability of the cubic phase in $Ba_{0.5}Sr_{0.5}Co_{0.8}Fe_{0.2}O_{3-\delta}$ (BSCF) 1, Solid State Ionics 197 (2011) 25–31.
[25] B. Rutkowski, J. Malzbender, R.W. Steinbrech, T. Beck, H.J. Bouwmeester, Influence of thermal history on the cubic-to-hexagonal phase transformation and creep behaviour of $Ba_{0.5}Sr_{0.5}Co_{0.8}Fe_{0.2}O_{3-\delta}$ ceramics, J. Membr. Sci. 381 (2011) 221–225.
[26] M. Arnold, T. Gesing, J. Martynczuk, A. Feldhoff, Correlation of the formation and the decomposition process of the BSCF perovskite at intermediate temperatures, Chem. Mater. 20 (2008) 5851–5858.
[27] K. Efimov, T. Halfer, A. Kuhn, P. Heitijans, J. Caro, A. Feldhoff, Novel cobalt-free oxygen-permeable perovskite-type membrane, Chem. Mater. 22 (2010) 1540–1544.
[28] H. Wang, C. Tablet, A. Feldhoff, J. Caro, A cobalt-free oxygen-permeable membrane based on the perovskite-type oxide $Ba_{0.5}Sr_{0.5}Zn_{0.2}Fe_{0.8}O_{3-\delta}$, Adv. Mater. 17 (2005) 1785.
[29] J. Martynczuk, F. Liang, M. Arnold, V. Sepelak, A. Feldhoff, Aluminum-doped perovskites as high-performance oxygen permeation materials, Chem. Mater. 21 (2009) 1586.
[30] K. Efimov, Q. Xu, A. Feldhoff, Transmission electron microscopy study of $Ba_{0.5}Sr_{0.5}Co_{0.8}Fe_{0.2}O_{3-\delta}$ perovskite decomposition at intermediate temperatures, Chem. Mater. 22 (2010) 5866–5875.
[31] S. Baumann, F. Schulze-Küppers, S. Roitsch, M. Betz, M. Zwick, E.M. Pfaff, W.A. Meulenberg, J. Mayer, D. Stöver, Influence of sintering conditions on microstructure and oxygen permeation of $Ba_{0.5}Sr_{0.5}Co_{0.8}Fe_{0.2}O_{3-\delta}$ (BSCF) oxygen transport membranes, J. Membr. Sci. 359 (2010) 102–109.
[32] D.N. Mueller, R.A. De Souza, T.E. Weirich, D. Roehrens, J. Mayer, M. Martin, A kinetic study of the decomposition of the cubic perovskite-type oxide $Ba_xSr_{1-x}Co_{0.8}Fe_{0.2}O_{3-\delta}$ (BSCF) (x = 0.1 and 0.5), Phys. Chem. Chem. Phys. 12 (2010) 10320–10328.
[33] J.F. Vente, W.G. Haije, Z.S. Rak, Performance of functional perovskite membranes for oxygen production, J. Membr. Sci. 276 (2006) 178–184.
[34] S.R. Bishop, K.L. Duncan, E.D. Wachsman, Thermo-chemical expansion in strontium-doped Lanthanum cobalt iron oxide, J. Am. Ceram. Soc. 93 (2010) 4115–4121.
[35] C. Chemelli, F. Drago, L. Ferravante, C. Rinaldi, E. Storni, Membrane per la separazione dell'ossigeno, RSE Rep. (2012), 12005748.
[36] P. Riello, A. Lausi, J. MacL.O.O.D, J.R. Plaiser, G. Zerauschek, P. Fornasiero, In situ reaction furnace for real-time XRD studies, J. Synchrotron Radiat. 20 (2013) 194–196.
[37] M. Merlini, M. Hanfland, Single-crystal diffraction at megabar conditions by synchrotron radiation, High Press. Res. 33 (2013) 511–522.
[38] T. Chakraborty, C. Meneghini, G. Aquilanti, S. Ray, Structural, electrical and magnetic properties of $Ba_{0.9}Co_{0.1}Ti_{0.97}Fe_{0.03}O_{3-\delta}$ and the effect of oxygen vacancies, J. Appl. Phys. 114 (2013) 223911.
[39] C. Meneghini, F. Bardelli, S. Mobilio, ESTRA-FitEXA: a software package for EXAFS data analysis, Nucl. Inst. Methods B 285 (2012) 153–157.
[40] A. Leo, S. Smarta, S. Liub, J.C. Diniz da Costa, High performance perovskite hollow fibres for oxygen separation, J. Membr. Sci. 368 (2011) 64–68.
[41] A.A. Yaremchenko, C. Buysse, V. Middelkoop, F. Snijkers, A. Buekenhoudt, J.R. Frade, A.V. Kovalevsky, Impact of sulphur contamination on the oxygen transport mechanism through BSCF5582: relevant issues in the development of capillary and hollow fibre membrane geometry, J. Membr. Sci. 428 (2013) 123–130.
[42] Jae-Il Jung, Doreen D. Edwards, X-ray photoelectron (XPS) and Diffuse Reflectance Infra Fourier Transformation (DRIFT) study of $Ba_{0.5}Sr_{0.5}Co_xFe_{1-x}O_{3-\delta}$ (BSCF: x = 0–0.8) ceramics, J. Solid State Chem. 184 (2011) 2238–2243.
[43] M. Arnold, H. Wang, A. Feldhoff, Influence of CO_2 on the oxygen permeation performance and the microstructure of perovskite-type BSCF5582 membranes, J. Membr. Sci. 293 (2007) 44–52.
[44] Z. Shao, G. Xiong, H. Dong, W. Yang, L. Lin, Synthesis, oxygen permeation study and membrane performance of a $Ba_{0.5}Sr_{0.5}Co_{0.8}Fe_{0.2}O_{3-\delta}$ oxygen-permeable dense ceramic reactor for partial oxidation of methane to syngas, Sep. Purif. Technol. 25 (2001) 97–116.

Bibliography

[1] Takehisa Fukui, Kenji Murata, Satoshi Ohara, Hiroya Abe, Makio Naito, and Kiyoshi Nogi. Morphology control of {Ni-YSZ} cermet anode for lower temperature operation of {SOFCs}. *Journal of Power Sources*, 125(1):17 – 21, 2004.

[2] Annelise Kopp Alves, Felipe Amorim Berutti, and Felipe Antonio Lucca Sánchez. *Nanomaterials and Catalysis*, pages 93–117. Springer Berlin Heidelberg, Berlin, Heidelberg, 2011.

[3] Reihaneh Malakooti, Hesamaldin Mahmoudi, Rahele Hosseinabadi, Srebri Petrov, and Andrea Migliori. Facile synthesis of pure non-monoclinic zirconia nanoparticles and their catalytic activity investigations for knoevenagel condensation. *RSC Adv.*, 3:22353–22359, 2013.

[4] Jean-Michel Lavoie. Review on dry reforming of methane, a potentially more environmentally-friendly approach to the increasing natural gas exploitation. *Frontiers in Chemistry*, 2:81, 2014.

[5] Weizuo Li and Zhongkui Zhao. Hierarchically structured tetragonal zirconia as a promising support for robust ni based catalysts for dry reforming of methane. *RSC Adv.*, 6:72942–72951, 2016.

[6] Weizuo Li, Zhongkui Zhao, Yanhua Jiao, and Guiru Wang. Morphology effect of zirconia support on the catalytic performance of supported ni catalysts for dry reforming of methane. *Chinese Journal of Catalysis*, 37(12):2122 – 2133, 2016.

[7] Ahmed Sadeq Al-Fatesh, Muhammad Awais Naeem, Wasim Ullah Khan, Ahmed Elhag Abasaeed, and Anis Hamza Fakeeha. Effect of nano-support

and type of active metal on reforming of ch4 with co2. *Journal of the Chinese Chemical Society*, 61(4):461–470, 2014.

[8] Gang Chen, Yu Gao, Yifei Luo, and Ruifeng Guo. Effect of a site deficiency of {LSM} cathode on the electrochemical performance of {SOFCs} with stabilized zirconia electrolyte. *Ceramics International*, 43(1, Part B):1304 – 1309, 2017.

[9] D.A. Agarkov, I.N. Burmistrov, F.M. Tsybrov, I.I. Tartakovskii, V.V. Kharton, and S.I. Bredikhin. In-situ raman spectroscopy analysis of the interfaces between ni-based {SOFC} anodes and stabilized zirconia electrolyte. *Solid State Ionics*, 302:133 – 137, 2017. ISSFIT12.

[10] SPS Badwal, S Giddey, C Munnings, and A Kulkarni. Review of progress in high temperature solid oxide fuel cells. *ChemInform*, 46(31), 2015.

[11] Pei-Chen Su, Cheng-Chieh Chao, Joon Hyung Shim, Rainer Fasching, and Fritz B. Prinz. Solid oxide fuel cell with corrugated thin film electrolyte. *Nano Letters*, 8(8):2289–2292, 2008. PMID: 18605702.

[12] Carlos R. Vera, Carlos L. Pieck, Kiyoyuki Shimizu, and JoséM. Parera. Tetragonal structure, anionic vacancies and catalytic activity of so_4^{2-}–zro_2 catalysts for n-butane isomerization. *Applied Catalysis A: General*, 230(1,Äì2):137 – 151, 2002.

[13] Neelima Mahato, Amitava Banerjee, Alka Gupta, Shobit Omar, and Kantesh Balani. Progress in material selection for solid oxide fuel cell technology: A review. *Progress in Materials Science*, 72:141 – 337, 2015.

[14] Adrian Leo, Shaomin Liu, and Jo ao C. Diniz da Costa. Development of mixed conducting membranes for clean coal energy delivery. *International Journal of Greenhouse Gas Control*, 3(4):357 – 367, 2009.

[15] Zhihao Chen, Ran Ran, Zongping Shao, Hai Yu, J.C. Diniz da Costa, and Shaomin Liu. Further performance improvement of $Ba_{0.5}Sr0.5Co_{0.8}Fe_{0.2}O_{3-\delta}$ perovskite membranes for air separation. *Ceramics International*, 35(6):2455 – 2461, 2009.

[16] S. Baumann and F. Schulze-K˙ Influence of sintering conditions on microstructure and oxygen permeation of $Ba_{0.5}Sr0.5Co_{0.8}Fe_{0.2}O_{3-\delta}$(BSCF) oxygen transport membranes. *Journal of Membrane Science*, 359(1-2):102 – 109, 2010. Membranes and CO2 Separation.

[17] P. Haworth, S. Smart, J. Glasscock, and J.C. Diniz da Costa. Yttrium doped BSCF membranes for oxygen separation. *Separation and Purification Technology*, 81(1):88 – 93, 2011.

[18] Hannes Stadler, Franz Beggel, Martin Habermehl, Bernhard Persigehl, Reinhold Kneer, Michael Modigell, and Peter Jeschke. Oxyfuel coal combustion by efficient integration of oxygen transport membranes. *International Journal of Greenhouse Gas Control*, 5(1):7 – 15, 2011.

[19] Salwa Meredith Hashim, Abdul Rahman Mohamed, and Subhash Bhatia. Current status of ceramic-based membranes for oxygen separation from air. *Advances in Colloid and Interface Science*, 160(1-2):88 – 100, 2010.

[20] Haihui Wang, Cristina Tablet, Armin Feldhoff, and J˙ Investigation of phase structure, sintering, and permeability of perovskite-type $Ba_{0.5}Sr0.5Co_{0.8}Fe_{0.2}O_{3-\delta}$ membranes. *Journal of Membrane Science*, 262(1-2):20 – 26, 2005.

[21] Stefan Engels, Torsten Markus, Michael Modigell, and Lorenz Singheiser. Oxygen permeation and stability investigations on miec membrane materials under operating conditions for power plant processes. *Journal of Membrane Science*, 370(1-2):58 – 69, 2011.

[22] Nandita Lakshminarayanan, Hyunkyu Choi, John N. Kuhn, and Umit S. Ozkan. Effect of additional b-site transition metal doping on oxygen transport and activation characteristics in $La_0.6Sr_{0.4}(Co_{0.18}Fe_{0.72}X_{0.1})O_{3-\delta}$ (where X = Zn, Ni or Cu) perovskite oxides. *Applied Catalysis B: Environmental*, 103(3-4):318 – 325, 2011.

[23] James Ovenstone, Jae-Il Jung, Jeffery S. White, Doreen D. Edwards, and Scott T. Misture. Phase stability of BSCF in low oxygen partial pressures. *Journal of Solid State Chemistry*, 181(3):576 – 586, 2008.

[24] Mirko Arnold, Haihui Wang, and Armin Feldhoff. Influence of co2 on the oxygen permeation performance and the microstructure of perovskite type $Ba_{0.5}Sr_{0.5})(Co_{0.8}Fe_{0.2})O_{3-\delta}$ membranes. *Journal of Membrane Science*, 293(1-2):44 – 52, 2007.

[25] Xiaoyao Tan, Zhigang Wang, Bo Meng, Xiuxia Meng, and K. Li. Pilot-scale production of oxygen from air using perovskite hollow fibre membranes. *Journal of Membrane Science*, 352(1-2):189 – 196, 2010.

[26] Xiaoyao Tan, Nan Liu, Bo Meng, Jaka Sunarso, Kun Zhang, and Shaomin Liu. Oxygen permeation behavior of $La_0.6Sr_{0.4}Co_{0.8}Fe_{0.2}O_3$ hollow fibre membranes with highly concentrated CO_2 exposure. *Journal of Membrane Science*, 389:216 – 222, 2012.

[27] Zongping Shao, Weishen Yang, You Cong, Hui Dong, Jianhua Tong, and Guoxing Xiong. Investigation of the permeation behavior and stability of a $Ba_{0.5}Sr_{0.5}Co_{0.8}Fe_{0.2}O_{3-\delta}$ oxygen membrane. *Journal of Membrane Science*, 172(1-2):177 – 188, 2000.

[28] D. Schlehuber, E. Wessel, L. Singheiser, and T. Markus. Long-term operation of a $La_{0.58}Sr_0.4Co_{0.2}Fe_{0.8}O_{3-\delta}$ membrane for oxygen separation. *Journal of Membrane Science*, 351(1-2):16 – 20, 2010.

[29] S.M. Fang, C.Y. Yoo, and H.J.M. Bouwmeester. Performance and stability of niobium-substituted $Ba_{0.5}Sr0.5Co_{0.8}Fe_{0.2}O_{3-\delta}$ membranes. *Solid State Ionics*, 195(1):1 – 6, 2011.

[30] F. Borghi, E. Sogne, C. Lenardi, A. Podestà, M. Merlini, C. Ducati, and P. Milani. Cluster-assembled cubic zirconia films with tunable and stable nanoscale morphology against thermal annealing. *Journal of Applied Physics*, 120(5):055302, 2016.

[31] L. Bettini. *Synthesis and electrochemical investigation of cluster assembled carbon thin films*. PhD thesis, Università degli studi di Milano, 2013.

[32] K. Wegner, P. Piseri, H. Vahedi Tafreshi, and P. Milani. Cluster beam deposition: a tool for nanoscale science and technology. *Journal of Physics D: Applied Physics*, 39:439, 2006.

[33] E Barborini, P Piseri, and P Milani. A pulsed microplasma source of high intensity supersonic carbon cluster beams. *Journal of Physics D: Applied Physics*, 32(21):L105, 1999.

[34] E. Barborini, P. Piseri, A. Podestà, and P. Milani. Cluster beam microfabrication of patterns of three-dimensional nanostructured objects. *Applied Physics Letters*, 77(7):1059–1061, 2000.

[35] P. Milani, E. Barborini, C.E. Bottani, A.C. Ferrari, and A. Li Bassi. Nanostructured carbon films from supersonic cluster beam deposition: structure and morphology. *The European Physical Journal D - Atomic, Molecular, Optical and Plasma Physics*, 9:63–68, 1999.

[36] P. Milani, A. Podestà, P. Piseri, E. Barborini, C. Lenardi, and Castelnovo. C. Cluster assembling of nanostructured carbon films. *Diamond and Related Materials*, 10(2):240–247, 2001.

[37] P. Piseri, A. Podestà, E. Barborini, and P. Milani. Production and characterization of highly intense and collimated cluster beams by inertial focusing in supersonic expansions. *Review of Scientific Instruments*, 72(5):2261–2267, 2001.

[38] P. Piseri, H. Vahedi Tafreshi, and P. Milani. Manipulation of nanoparticles in supersonic beams for the production of nanostructured materials. *Current Opinion in Solid State and Materials Science*, 8:195–202, 2004.

[39] C. Piconi and G. Maccauro. Zirconia as a ceramic biomaterial. *Biomaterials*, 20(1):1 – 25, 1999.

[40] Jèrôme Duval, Johannes Lyklema, J. Mieke Kleijn, and Herman P. van Leeuwen. Amphifunctionally electrified interfaces: Coupling of electronic and ionic surface-charging processes. *Langmuir*, 17(24):7573–7581, 2001.

[41] Paolo Francesco Manicone, Pierfrancesco Rossi Iommetti, and Luca Raffaelli. An overview of zirconia ceramics: Basic properties and clinical applications. *Journal of Dentistry*, 35(11):819 – 826, 2007.

[42] X.Q. Cao, R. Vassen, and D. Stoever. Ceramic materials for thermal barrier coatings. *Journal of the European Ceramic Society*, 24(1):1 – 10, 2004.

[43] X Zhou, I Balachov, and D.D Macdonald. The effect of dielectric coatings on igscc in sensitized type 304 ss in high temperature dilute sodium sulfate solution. *Corrosion Science*, 40(8):1349 – 1362, 1998.

[44] Qinyuan Zhang, Jun Shen, Jue Wang, Guangming Wu, and Lingyan Chen. Sol-gel derived ZrO_2-SiO_2 highly reflective coatings. *International Journal of Inorganic Materials*, 2(4):319 – 323, 2000.

[45] T Nguyen and E Djurado. Deposition and characterization of nanocrystalline tetragonal zirconia films using electrostatic spray deposition. *Solid State Ionics*, 138(3-4):191 – 197, 2001.

[46] John P Breen and Julian R.H Ross. Methanol reforming for fuel-cell applications: development of zirconia-containing cu-zn-al catalysts. *Catalysis Today*, 51(3-4):521 – 533, 1999.

[47] Fereydoon Namavar, Gonghua Wang, Chin Li Cheung, Renat F Sabirianov, Xiao Cheng Zeng, Wai Ning Mei, Jaeil Bai, Joseph R Brewer, Hani Haider, and Kevin L Garvin. Thermal stability of nanostructurally stabilized zirconium oxide. *Nanotechnology*, 18(41):415702, 2007.

[48] Carsten Schulte, Simona Rodighiero, Martino Alfredo Cappelluti, Luca Puricelli, Elisa Maffioli, Francesca Borghi, Armando Negri, Elisa Sogne, Massimiliano Galluzzi, Claudio Piazzoni, Margherita Tamplenizza, Alessandro Podestà, Gabriella Tedeschi, Cristina Lenardi, and Paolo Milani. Conversion of nanoscale topographical information of cluster-assembled zirconia surfaces into mechanotransductive events promotes neuronal differentiation. *Journal of Nanobiotechnology*, 14(1):18, 2016.

[49] Suveen Kumar, Saurabh Kumar, Sachchidanand Tiwari, Saurabh Srivastava, Manish Srivastava, Birendra Kumar Yadav, Saroj Kumar, Thien Toan Tran, Ajay Kumar Dewan, Ashok Mulchandani, Jai Gopal Sharma, Sagar Maji, and Bansi Dhar Malhotra. Biofunctionalized nanostructured zirconia for biomedical application: A smart approach for oral cancer detection. *Advanced Science*, 2(8):1500048–n/a, 2015. 1500048.

[50] J. Chevalier, L. Gremillard, A.V. Virkar, and D.R. Clarke. The tetragonal-monoclinic transformation in zirconia: Lessons learned and future trends. *Journal of the American Ceramic Society*, 92(9):1901–1920, 2009.

[51] Patrick M. Kelly and L.R. Francis Rose. The martensitic transformation in ceramics its role in transformation toughening. *Progress in Materials Science*, 47(5):463 – 557, 2002.

[52] Koutaro Kawata, Hideki Maekawa, Takahiro Nemoto, and Tsutomu Yamamura. Local structure analysis of {YSZ} by y-89 mas-nmr. *Solid State Ionics*, 177(19-25):1687 – 1690, 2006. Solid State Ionics 15: Proceedings of the 15th International Conference on Solid State Ionics, Part I.

[53] Stefano Fabris, Anthony T. Paxton, and Michael W. Finnis. A stabilization mechanism of zirconia based on oxygen vacancies only. *Acta Materialia*, 50(20):5171 – 5178, 2002.

[54] Davide Sangalli and Alberto Debernardi. Exchange-correlation effects in the monoclinic to tetragonal phase stabilization of yttrium-doped zro_2: A first-principles approach. *Phys. Rev. B*, 84:214113, Dec 2011.

[55] Reza Ghasemi, Reza Shoja-Razavi, Reza Mozafarinia, and Hossein Jamali. Comparison of microstructure and mechanical properties of plasma-sprayed nanostructured and conventional yttria stabilized zirconia thermal barrier coatings. *Ceramics International*, 39(8):8805 – 8813, 2013.

[56] S Shukla and S Seal. Mechanisms of room temperature metastable tetragonal phase stabilisation in zirconia. *International materials reviews*, 50(1):45–64, 2005.

[57] G. Sumana, Maumita Das, Saurabh Srivastava, and B.D. Malhotra. A novel urea biosensor based on zirconia. *Thin Solid Films*, 519(3):1187 – 1191, 2010. Biomolecular Electronics and Organic Nanotechnology for Environmental Preservation.

[58] Pratima R. Solanki, Ajeet Kaushik, P.M. Chavhan, S.N. Maheshwari, and B.D. Malhotra. Nanostructured zirconium oxide based genosensor for escherichia coli detection. *Electrochemistry Communications*, 11(12):2272 – 2277, 2009.

[59] Suveen Kumar, Jai Gopal Sharma, Sagar Maji, and Bansi Dhar Malhotra. Nanostructured zirconia decorated reduced graphene oxide based efficient biosensing platform for non-invasive oral cancer detection. *Biosensors and Bioelectronics*, 78:497 – 504, 2016.

[60] Pasquale Emanuele Scopelliti, Antonio Borgonovo, Marco Indrieri, Luca Giorgetti, Gero Bongiorno, Roberta Carbone, Alessandro Podestá, and Paolo Milani. The effect of surface nanometre-scale morphology on protein adsorption. *PLOS ONE*, 5(7):1–9, 07 2010.

[61] Satyajit Shukla, Sudipta Seal, Rashmi Vij, Sri Bandyopadhyay, and Zia Rahman. Effect of nanocrystallite morphology on the metastable tetragonal phase stabilization in zirconia. *Nano Letters*, 2(9):989–993, 2002.

[62] Fereydoon Namavar, Chin Li Cheung, Renat F. Sabirianov, Wai-Ning Mei, Xiao Cheng Zeng, Gonghua Wang, Hani Haider, and Kevin L. Garvin. Lotus effect in engineered zirconia. *Nano Letters*, 8(4):988–996, 2008. PMID: 18338872.

[63] A. Ortiz, J. C. Alonso, and E. Haro-Poniatowski. Spray deposition and characterization of zirconium-oxide thin films. *Journal of Electronic Materials*, 34(2):150–155, 2005.

[64] H. Hahn and R. S. Averback. The production of nanocrystalline powders by magnetron sputtering. *Journal of Applied Physics*, 67(2):1113–1115, 1990.

[65] E. Djurado, P. Bouvier, and G. Lucazeau. Crystallite size effect on the tetragonal-monoclinic transition of undoped nanocrystalline zirconia studied by xrd and raman spectrometry. *Journal of Solid State Chemistry*, 149(2):399 – 407, 2000.

[66] Tomas Chraska, Alexander H King, and Christopher C Berndt. On the size-dependent phase transformation in nanoparticulate zirconia. *Materials Science and Engineering: A*, 286(1):169 – 178, 2000.

[67] A. Debernardi, D. Sangalli, A. Lamperti, E. Cianci, P. Lupo, F. Casoli, F. Albertini, L. Nasi, R. Ciprian, and P. Torelli. Electronic and magnetic properties of iron doped zirconia: Theory and experiment. *Journal of Applied Physics*, 115(17):17D718, 2014.

[68] Ronald C. Garvie. The occurrence of metastable tetragonal zirconia as a crystallite size effect. *The Journal of Physical Chemistry*, 69(4):1238–1243, 1965.

[69] Yoshio Murase and Etsuro Kato. Role of water vapor in crystallite growth and tetragonal-monoclinic phase transformation of zro2. *Journal of the American Ceramic Society*, 66(3):196–200, 1983.

[70] Paul S. Bagus, Eugene S. Ilton, and Connie J. Nelin. The interpretation of {XPS} spectra: Insights into materials properties. *Surface Science Reports*, 68(2):273 – 304, 2013.

[71] Thomas C Taucher, Iris Hehn, Oliver T Hofmann, Michael Zharnikov, and Egbert Zojer. Understanding chemical versus electrostatic shifts in x-ray photoelectron spectra of organic self-assembled monolayers. *The Journal of Physical Chemistry C*, 120(6):3428–3437, 2016.

[72] Ashish Chauhan and Priyanka Chauhan. Powder xrd technique and its applications in science and technology. *Journal of Analytical & Bioanalytical Techniques*, 5(5):1–5, 2014.

[73] Li Tan Zhen Guo. *Fundamentals and applications of nanomaterials*. Boston : Artech house, 2009.

[74] B. E. Warren. *X-Ray Diffraction*. Mineola, NY: Courier Dover Publications, 1990.

[75] G.P. Parravicini G. Grosso. *Solid State Physics*. Academic Press, 2000.

[76] D. Sangalli. Metodi innovativi per il calcolo della risposta lineare nell'ambito della teoria del funzionale densità in sistemi spin polarizzati. Master's thesis, Università degli studi di Milano, year.

[77] F. Sottile. *Response functions of semiconductors and insulators: from the Bethe-Salpeter equation to time-dependent density functional theory*. PhD thesis, Ecole Polytechnique, 2003.

[78] M. Veronica Ganduglia-Pirovano, Alexander Hofmann, and Joachim Sauer. Oxygen vacancies in transition metal and rare earth oxides: Current state of understanding and remaining challenges. *Surface Science Reports*, 62(6):219 – 270, 2007.

[79] A. S. Foster, V. B. Sulimov, F. Lopez Gejo, A. L. Shluger, and R. M. Nieminen. Structure and electrical levels of point defects in monoclinic zirconia. *Phys. Rev. B*, 64:224108, Nov 2001.

[80] J.L. Lyons, A. Janotti, and C.G. Van de Walle. The role of oxygen-related defects and hydrogen impurities in hfo2 and zro2. *Microelectronic Engineering*, 88(7):1452 – 1456, 2011. Proceedings of the 17th Biennial International Insulating Films on Semiconductor Conference17th Biennial International Insulating Films on Semiconductor Conference.

[81] J. X. Zheng, G. Ceder, T. Maxisch, W. K. Chim, and W. K. Choi. First-principles study of native point defects in hafnia and zirconia. *Phys. Rev. B*, 75:104112, Mar 2007.

[82] http://www.kolibrik.net/science/kolxpd/.

[83] Sulaiman N. Basahel, Tarek T. Ali, Mohamed Mokhtar, and Katabathini Narasimharao. Influence of crystal structure of nanosized zro2 on photocatalytic degradation of methyl orange. *Nanoscale Research Letters*, 10(1):73, 2015.

[84] Marco Merlini and Michael Hanfland. Single-crystal diffraction at megabar conditions by synchrotron radiation. *High Pressure Research*, 33(3):511–522, 2013.

[85] Tanushree Chakraborty, Carlo Meneghini, Giuliana Aquilanti, and Sugata Ray. Structural, electrical, and magnetic properties of $Ba_{0.9}Ca_{0.1}Ti_{0.97}Fe_{0.03}O_3$ and the effect of oxygen vacancies. *Journal of Applied Physics*, 114(22), 2013.

[86] Manoranjan Ghosh, Debjani Karmakar, S Basu, SN Jha, D Bhattacharyya, SC Gadkari, and SK Gupta. Effect of size and aspect ratio on structural parameters and evidence of shape transition in zinc oxide nanostructures. *Journal of Physics and Chemistry of Solids*, 75(4):543–549, 2014.

[87] Vasili Perebeinos, SiuWai Chan, and Feng Zhang. Madelung model prediction for dependence of lattice parameter on nanocrystal size. *Solid state communications*, 123(6):295–297, 2002.

[88] J. P. Perdew and Alex Zunger. Self-interaction correction to density-functional approximations for many-electron systems. *Phys. Rev. B*, 23:5048–5079, May 1981.

[89] W. Kohn and L. J. Sham. Self-consistent equations including exchange and correlation effects. *Phys. Rev.*, 140:A1133–A1138, Nov 1965.

[90] P. Hohenberg and W. Kohn. Inhomogeneous electron gas. *Phys. Rev.*, 136:B864–B871, Nov 1964.

[91] Paolo Giannozzi, Stefano Baroni, Nicola Bonini, Matteo Calandra, Roberto Car, Carlo Cavazzoni, Davide Ceresoli, Guido L Chiarotti, Matteo Cococcioni, Ismaila Dabo, Andrea Dal Corso, Stefano de Gironcoli, Stefano Fabris, Guido Fratesi, Ralph Gebauer, Uwe Gerstmann, Christos Gougoussis, Anton Kokalj, Michele Lazzeri, Layla Martin-Samos, Nicola Marzari, Francesco Mauri, Riccardo Mazzarello, Stefano Paolini, Alfredo Pasquarello, Lorenzo Paulatto, Carlo Sbraccia, Sandro Scandolo, Gabriele Sclauzero, Ari P Seitsonen, Alexander Smogunov, Paolo Umari, and Renata M Wentzcovitch. Quantum espresso: a modular and open-source software project for quantum simulations of materials. *Journal of Physics: Condensed Matter*, 21(39):395502, 2009.

[92] A Baldereschi and M Peressi. Atomic scale structure of ionic and semiconducting solid solutions. *Journal of Physics: Condensed Matter*, 5(34B):B37, 1993.

[93] Hendrik J. Monkhorst and James D. Pack. Special points for brillouin-zone integrations. *Phys. Rev. B*, 13:5188–5192, Jun 1976.

[94] Priscila Lemes-Rachadel, Giulliani Sachinelli Garcia, Ricardo Antonio Francisco Machado, Dachamir Hotza, and João Carlos Diniz da Costa. Current developments of mixed conducting membranes on porous substrates. *Materials Research*, 17:242 – 249, 02 2014.

[95] H.J.M. Bouwmeester and A.J. Burggraaf. Chapter 10 dense ceramic membranes for oxygen separation. In A.J. Burggraaf and L. Cot, editors, *Fundamentals of Inorganic Membrane Science and Technology*, volume 4 of *Membrane Science and Technology*, pages 435 – 528. Elsevier, 1996.

[96] F.T Akin and Y.S Lin. Selective oxidation of ethane to ethylene in a dense tubular membrane reactor. *Journal of Membrane Science*, 209(2):457 – 467, 2002.

[97] Takao Nozaki and Kaoru Fujimoto. Oxide ion transport for selective oxidative coupling of methane with new membrane reactor. *AIChE Journal*, 40(5):870–877, 1994.

[98] J.E. ten Elshof, B.A. van Hassel, and H.J.M. Bouwmeester. Catalysis in membrane reactors activation of methane using solid oxide membranes. *Catalysis Today*, 25(3):397 – 402, 1995.

[99] W. Wang and Y.S. Lin. Analysis of oxidative coupling of methane in dense oxide membrane reactors. *Journal of Membrane Science*, 103(3):219 – 233, 1995.

[100] Sherman J. Xu and William J. Thomson. Perovskite-type oxide membranes for the oxidative coupling of methane. *AIChE Journal*, 43(S11):2731–2740, 1997.

[101] W.T. Yang. 2-18 F-2-Fluoro-2-Deoxy-D-Glucose positron emission tomography in staging of locally advanced breast cancer. *Breast Diseases: A Year Book Quarterly*, 16(2):155 – 157, 2005.

[102] J. Sunarso, S. Baumann, J.M. Serra, W.A. Meulenberg, S. Liu, Y.S. Lin, and J.C. Diniz da Costa. Mixed ionic-electronic conducting MIEC ceramic-based membranes for oxygen separation. *J. Membr. Sci.*, 320(1-2):13–41, 2008.

[103] Javier Pérez-Ramírez and Bent Vigeland. Perovskite membranes in ammonia oxidation: Towards process intensification in nitric acid manufacture. *Angewandte Chemie International Edition*, 44(7):1112–1115, 2005.

[104] M. Czyperek, P. Zapp, H.J.M. Bouwmeester, M. Modigell, K. Ebert, I. Voigt, W.A. Meulenberg, L. Singheiser, and D. St˙Gas separation membranes for zero-emission fossil power plants: Mem-brain. *Journal of Membrane Science*, 359(1-2):149 – 159, 2010. Membranes and CO_2 Separation.

[105] S.J Skinner and J.A Kilner. Oxygen diffusion and surface exchange in $La_{2-x}Sr_x$ $NiO_{4+\delta}$. *Solid State Ionics*, 135(1-4):709 – 712, 2000. Proceedings of the 12th International Conference on Solid State.

[106] Y. Ji, J.A. Kilner, and M.F. Carolan. Electrical properties and oxygen diffusion in yttria-stabilised zirconia (YSZ)-$La_{0.8}Sr_{0.2}MnO_{3\pm\delta}$ (LSM) composites. *Solid State Ionics*, 176(9-10):937 – 943, 2005.

[107] V.V. Kharton, A.V. Kovalevsky, A.P. Viskup, A.L. Shaula, F.M. Figueiredo, E.N. Naumovich, and F.M.B. Marques. Oxygen transport in $Ce_{0.8}Gd_{0.2}O_{2-\delta}$ based composite membranes. *Solid State Ionics*, 160(3-4):247 – 258, 2003.

[108] K. Li, Xiaoyao Tan, and Yutie Liu. Single-step fabrication of ceramic hollow fibers for oxygen permeation. *Journal of Membrane Science*, 272(1-2):1 – 5, 2006.

[109] Shaomin Liu and George R. Gavalas. Oxygen selective ceramic hollow fiber membranes. *Journal of Membrane Science*, 246(1):103 – 108, 2005.

[110] Adrian Leo, Simon Smart, Shaomin Liu, and Jo ao C. Diniz da Costa. High performance perovskite hollow fibres for oxygen separation. *Journal of Membrane Science*, 368(1-2):64 – 68, 2011.

[111] J. M. Serra, V. B. Vert, O. Büchler, W. A. Meulenberg, and H. P. Buchkremer. It-sofc supported on mixed oxygen ionic-electronic conducting composites. *Chemistry of Materials*, 20(12):3867–3875, 2008.

[112] C. Buysse, A. Kovalevsky, F. Snijkers, A. Buekenhoudt, S. Mullens, J. Luyten, J. Kretzschmar, and S. Lenaerts. Fabrication and oxygen permeability of gastight, macrovoid-free $Ba_{0.5}Sr0.5Co_{0.8}Fe_{0.2}O_{3-\delta}$ capillaries for high temperature gas separation. *Journal of Membrane Science*, 359(1-2):86 – 92, 2010. Membranes and CO_2 Separation.

[113] T. Schiestel, M. Kilgus, S. Peter, K.J. Caspary, H. Wang, and J. Caro. Hollow fibre perovskite membranes for oxygen separation. *Journal of Membrane Science*, 258(1-2):1 – 4, 2005.

[114] V.M. Goldschmidt. Geochemische verterlungsgesetze der elemente, 1927. Oslo.

[115] S. A. Bhalla, R. Guo, and R. Roy. The perovskite structure – a review of its role in ceramic science and technology. *Material Research Innovations*, 4(1):3–26, 2000.

[116] H. W. Jang, A. Kumar, S. Denev, M. D. Biegalski, P. Maksymovych, C. W. Bark, C. T. Nelson, C. M. Folkman, S. H. Baek, N. Balke, C. M. Brooks, D. A. Tenne, D. G. Schlom, L. Q. Chen, X. Q. Pan, S. V. Kalinin, V. Gopalan, and C. B. Eom. Ferroelectricity in strain-free $SrTiO_3$ thin films. *Phys. Rev. Lett.*, 104:197601, May 2010.

[117] SB Adler. Factors governing oxygen reduction in solid oxide fuel cell cathodes. *chem. Rev.*, 104:4791, Oct 2004.

[118] R. J. H. Voorhoeve, D. W. Johnson, J. P. Remeika, and P. K. Gallagher. Perovskite oxides: Materials science in catalysis. *Science*, 195(4281):827–833, 1977.

[119] Allan J. Jacobson. Materials for solid oxide fuel cells. *Chemistry of Materials*, 22(3):660–674, 2010.

[120] Magdalena Helmer. Chemistry: Cleaning up catalysts. *Nature*, 418:138, July 2002.

[121] Chang Hwan Kim, Gongshin Qi, Kevin Dahlberg, and Wei Li. Strontium-doped perovskites rival platinum catalysts for treating NO_x in simulated diesel exhaust. *Science*, 327(5973):1624–1627, 2010.

[122] HJM Bouwmeester, AJ Burgraaf, AJ Burgraaf, and L Cot. Fundamentals of inorganic membrane science and technology, 1996, 435.

[123] S.B. Adler, X.Y. Chen, and J.R. Wilson. Mechanisms and rate laws for oxygen exchange on mixed-conducting oxide surfaces. *Journal of Catalysis*, 245(1):91 – 109, 2007.

[124] Haihui Wang, You Cong, and Weishen Yang. Oxygen permeation study in a tubular $Ba_{0.5}Sr0.5Co_{0.8}Fe_{0.2}O_{3-\delta}$ oxygen permeable membrane. *Journal of Membrane Science*, 210(2):259 – 271, 2002.

[125] Zhaohui Yang and Y.S Lin. A semi-empirical equation for oxygen nonstoichiometry of perovskite-type ceramics. *Solid State Ionics*, 150(3-4):245 – 254, 2002.

[126] Bart A. van Hassel, Tatsuya Kawada, Natsuko Sakai, Harumi Yokokawa, Masayuki Dokiya, and Henny J.M. Bouwmeester. Oxygen permeation modelling of perovskites. *Solid State Ionics*, 66(3):295 – 305, 1993.

[127] G. Z. Cao. Electrical conductivity and oxygen semipermeability of terbia and yttria stabilized zirconia. *Journal of Applied Electrochemistry*, 24(12):1222–1227, 1994.

[128] Yue-Sheng Lin, Weijian Wang, and Jonghee Han. Oxygen permeation through thin mixed-conducting solid oxide membranes. *AIChE Journal*, 40(5):786–798, 1994.

[129] H.J.M. Bouwmeester, H. Kruidhof, A.J. Burggraaf, and P.J. Gellings. Oxygen semipermeability of erbia-stabilized bismuth oxide. *Solid State Ionics*, 53:460 – 468, 1992.

[130] S. Dou, C. R. Masson, and P. D. Pacey. Mechanism of oxygen permeation through lime-stabilized zirconia. *Journal of The Electrochemical Society*, 132(8):1843–1849, 1985.

[131] R.M. Thorogood, R. Srinivasan, T.F. Yee, and M.P. Drake. Composite mixed conductor membranes for producing oxygen, August 31 1993. US Patent 5,240,480.

[132] Mariangela Brisotto, Federico Cernuschi, Francesca Drago, Cristina Lenardi, Patrizia Rosa, Carlo Meneghini, Marco Merlini, and Claudia Rinaldi. High temperature stability of $Ba_{0.5}Sr0.5Co_{0.8}Fe_{0.2}O_{3-\delta}$ and $La_{0.6}Sr_{0.4}Co_{1-y}Fe_yO_{3-\delta}$ oxygen separation perovskite membranes. *Journal of the European Ceramic Society*, 36(7):1679 – 1690, 2016.

[133] Pietro Riello, Andrea Lausi, Jennifer Macleod, Jasper Rikkert Plaisier, Giulio Zerauschek, and Paolo Fornasiero. *In situ* reaction furnace for real-time XRD studies. *Journal of Synchrotron Radiation*, 20(1):194–196, Jan 2013.

[134] Hilde Lea Lein, Kjell Wiik, and Tor Grande. Thermal and chemical expansion of mixed conducting $La_{0.5}Sr_{0.5}Fe_{1-x}Co_xO_{3-\delta}$ materials. *Solid State Ionics*, 177(19-25):1795 – 1798, 2006. Solid State Ionics 15: Proceedings of the 15th International Conference on Solid State Ionics, Part I.

[135] Hilde Lea Lein, Kjell Wiik, Mari-ann Einarsrud, Tor Grande, and Edgar Lara-curzio. High-temperature creep behavior of mixed conducting $La_{0.5}Sr_{0.5}Fe_{1-x}Co_xO_{3-\delta}$ $(0.5 \leq x \leq 1)$ materials. *Journal of the American Ceramic Society*, 89(9):2895–2898, 2006.

[136] B.X. Huang, J. Malzbender, R.W. Steinbrech, and L. Singheiser. Mechanical properties of $La_{0.5}Sr_{0.4}Co_{0.2}Fe_{0.8}O_{3-\delta}$ membranes. *Solid State Ionics*, 180(2-3):241 – 245, 2009.

[137] Shin ichi Hashimoto, Yasuhiro Fukuda, Melanie Kuhn, Kazuhisa Sato, Keiji Yashiro, and Junichiro Mizusaki. Oxygen nonstoichiometry and thermo-chemical stability of $La_{0.6}Sr_{0.4}Co_{1-y}Fe_yO_{3-\delta}$ $(y = 0.2, 0.4, 0.6, 0.8)$. *Solid State Ionics*, 181(37-38):1713 – 1719, 2010.

[138] E. Talik, A. Pajaczkowska, A. Guzik, P. Zajdel, J. Kusz, A. Klos, and A. Szysiak. X-ray diffraction, electronic structure and magnetic characterization of nano and single crystals $SrLaAlO_4$: Mn optical materials. *Materials Science and Engineering:B*, 182:74–80, 2014.

[139] D. F. Mullica, C. K. C. Lok, H. O. Perkins, and V. Young. X-ray photoelectron final-state screening in $La(OH)_3$: A multiplet structural analysis. *Phys. Rev. B*, 31:4039–4042, Mar 1985.

[140] Xin ZHAO, Qiuhua YANG, and Jinjin CUI. XPS study of surface absorbed oxygen of ABO_3 mixed oxides. *Journal of Rare Earths*, 26(4):511 – 514, 2008.

[141] A. E. Bocquet, A. Fujimori, T. Mizokawa, T. Saitoh, H. Namatame, S. Suga, N. Kimizuka, Y. Takeda, and M. Takano. Electronic structure of $SrFe^{4+}O_3$ and related fe perovskite oxides. *Phys. Rev. B*, 45:1561–1570, Jan 1992.

[142] Miroslaw Zawadzki, Hanna Grabowska, and Janusz Trawczyński. Effect of synthesis method of LSCF perovskite on its catalytic properties for phenol methylation. *Solid State Ionics*, 181(23-24):1131 – 1139, 2010.

[143] C. Norman and C. Leach. In situ high temperature x-ray photoelectron spectroscopy study of barium strontium iron cobalt oxide. *Journal of Membrane Science*, 382(1-2):158 – 165, 2011.

[144] J.C Dupin, D Gonbeau, H Benqlilou-Moudden, Ph Vinatier, and A Levasseur. XPS analysis of new lithium cobalt oxide thin-films before and after lithium deintercalation. *Thin Solid Films*, 384(1):23 – 32, 2001.

[145] V.N. Stathopoulos, V.C. Belessi, T.V. Bakas, S.G. Neophytides, C.N. Costa, P.J. Pomonis, and A.M. Efstathiou. Comparative study of La-Sr-Fe-O perovskite-type oxides prepared by ceramic and surfactant methods over the CH_4 and H_2 lean-deNO_x. *Applied Catalysis B: Environmental*, 93(1-2):1 – 11, 2009.

[146] Yunhui Gong, Diego Palacio, Xueyan Song, Rajankumar L. Patel, Xinhua Liang, Xuan Zhao, John B. Goodenough, and Kevin Huang. Stabilizing nanostructured solid oxide fuel cell cathode with atomic layer deposition. *Nano Letters*, 13(9):4340–4345, 2013. PMID: 23924170.